TECHNISCHE UNIVERSITÄT DRESDEN

Fakultät für Maschinenwesen Institut für Energietechnik, Professur für Wasserstoff- und Kernenergietechnik

INVESTIGATION OF THE STABILITY OF A MOLTEN SALT FAST REACTOR

Diplomarbeit

Maximilian Kraus

Dresden, 31.03.2020

WKET

TU Dresden
Fakultät Maschinenwesen
Institut für Energietechnik
Professur für Wasserstoff- und Kernenergietechnik

Kontakt:
Web: tu-dresden.de/ing/mw/iet/wket
e-Mail: Sofie.paufler@tu-dresden.de
Telefon: 0351 463 34472

TECHNISCHE UNIVERSITÄT DRESDEN

Fakultät für Maschinenwesen Institut für Energietechnik, Professur für Wasserstoff- und Kernenergietechnik

Diplomarbeit

Thema:	Investigation of the Stability of a Molten Salt Fast Reactor
Bearbeiter:	Maximilian Kraus
Matrikelnummer:	3857047
Bearbeitungszeitraum:	01.11.2019 bis 31.03.2020
Ort, Datum der Abgabe:	Dresden, 31.03.2020
Nummer:	WKET-2019-05
Betreuer:	Dr.-Ing. Carsten Lange Dipl.-Phys. Marco Viebach
Verantw. Hochschullehrer:	Prof. Dr.-Ing. habil. Wolfgang Lippmann

Textseiten: 80

Anhänge: 26

KURZFASSUNG

Im Fokus dieser Arbeit steht die Stabilitätsanalyse des MSFR – eines Flüssigsalzreaktors mit schnellem Neutronenspektrum. Als Grundlage wurde ein Modell verwendet, das am Politecnico di Milano erstellt und dort mittels linearer Methoden untersucht wurde. Da lineare Betrachtungen nur eingeschränkte Stabilitätsaussagen treffen können, erweitert diese Arbeit die Untersuchungen um die nichtlineare Stabilitätsanalyse. Zur Untersuchung des vorgegebenen Reaktormodells wurden die Systemgleichungen in MATLAB übertragen und verifiziert. Mithilfe der Rechensoftware MatCont wurde eine sogenannten Fixpunkt-Lösung des Modells unter der Variation ausgewählter Parameter verfolgt und deren Stabilität überprüft. Es hat sich gezeigt, dass der betrachtete Fixpunkt seinen Stabilitätszustand dabei nicht verändert und stabil bleibt. Koexistierende Fixpunkte oder periodische Lösungen konnten nicht nachgewiesen werden. Daher gilt das betrachtete MSFR Modell als ein stabiles System, dessen Lösungen immer auf einen stationären Zustand zulaufen.

ABSTRACT

This work focusses on analysing the stability of the MSFR – a molten salt reactor with a fast neutron spectrum. The investigations are based on a model, which was published and studied by the Politecnico di Milano using a linear approach. Since linear methods can only provide stability information to a limited extent, this work continues the conducted investigations by applying nonlinear methods. In order to examine the specified reactor model, the system equations were implemented, adjusted and verified using MATLAB code. With the help of the computational tool MatCont, a so-called fixed-point solution was tracked and its stability monitored during the variation of selected control parameters. It was found that the considered fixed point does not change its stability state and remains stable. Coexisting fixed points or periodic solutions could not be detected. Therefore, the analysed MSFR model is considered to be a stable system, in which the solutions always tend towards a steady state.

CONTENTS

1 INTRODUCTION

With a growing population and advancing electrification and digitalisation of technology, global electricity consumption has risen continuously in the past decades [1]. In the future, it is essential to provide energy in a way that is resource-efficient, environmentally friendly and ecologically sustainable in order to protect life and biodiversity on our planet. The deployment of innovative nuclear reactors can make a valuable contribution to this goal:

- Nuclear power is a low-carbon technology and plays therefore a key role in mitigating climate change [2].
- The power density of nuclear power (240 W_e /m^2) is several orders of magnitude higher than the one of the renewable energy sources, solar (7 W_e /m^2), wind (2 W_e /m^2) and biomass (0.1 W_e /m^2) [3], meaning less land-use and environmental impact of nuclear power stations compared to wind farms and solar parks.
- New concepts involve the use of spent nuclear fuel for power generation in nuclear power plants, thereby reducing the amount of long-lived radioactive waste and leading to a closed nuclear fuel cycle [4].
- Proposed reactor designs of the Generation IV International Forum employ inherent and passive safety features, which are triggered automatically under accident conditions [4].

One of the six innovative reactor concepts introduced by the Generation IV International Forum is the Molten Salt Reactor (MSR). MSRs were first investigated in the 1950s as a possible power source for nuclear-driven military aircraft at the Oak Ridge National Laboratory in the United States [5]. Focus then shifted towards the use in civilian power generation, and multiple MSR designs were explored. However, research funding ceased in 1976, and the MSR idea remained dormant until interest rose again after the Generation IV International Forum recommended further research in 2002 [6].

In the past ten years, research groups at the Politecnico di Milano, the Paul Scherrer Institut and the Centre National de Recherche Scientifique have been investigating the concept of a molten salt reactor using a fast neutron spectrum – the Molten Salt Fast Reactor

(MSFR). One article published by the Politecnico di Milano [7] presents an MSFR model and analyses its dynamics and stability behaviour. This paper uses the linearised equation system of the proposed model for the investigation. However, certain phenomena in the behaviour of dynamical systems cannot be determined and explained with a linear approach [8]. One of those sensations is the bifurcation of periodic system solutions at so-called Hopf bifurcation points when varying a control parameter of the system. The coexistence of equilibrium (fixed point) and periodic (limit cycle) solutions can lead to catastrophic behaviour, a famous example of which is the collapse of the Tacoma Bridge in 1940 [8]. It is therefore necessary to consider the complete nonlinear system of the MSFR model in order to draw conclusions about the system stability.

The aim of this work is to examine the stability behaviour of the MSFR model specified in the reference article [7] by means of nonlinear and, for comparison, linear investigation methods. The consistency of both approaches shall be reviewed, and possible bifurcations identified. The analyses are conducted for operational conditions, thereby not taking accident scenarios into account.

For the stability investigations, the system of differential equations, which describes the dynamics of the MSFR model, is translated into MATLAB code. The implementation is verified by producing and comparing selected plots to those provided in the reference. In the next step, the model is prepared for analysis in the numerical bifurcation tool MatCont. This software monitors so-called fixed-point solutions while parameters of the equation system get varied and determines whether their stability state changes or new system solutions bifurcate. The results of the MatCont analysis are verified, discussed and compared with those of the linear analysis.

This thesis is organised as follows. Chapter 2 presents an overview of the history, the underlying technological principles and the advantages and drawbacks of MSRs. A detailed description of the MSFR design is given. The subsequent chapter provides definitions for the ‘stability’ concept and discusses fixed-point and periodic solutions of dynamical systems. Corresponding stability analysis methods are explained, and different bifurcation types presented. The analysed MSFR model is described, adjusted and verified in Chapter 4. Chapter 5 describes the framework and discusses the results of the conducted stability

analyses for the nonlinear and linear approach. Conclusions from this study and further research proposals are summarised in Chapter 6.

2 MOLTEN SALT REACTOR TECHNOLOGY

2.1 Introduction

This chapter presents the basic concepts of Molten Salt Reactors (MSRs). At first, an overview of the historical development of MSR research is given. The Aircraft Reactor Experiment (1954) and the Molten Salt Reactor Experiment (1965-1969) at the Oak Ridge National Laboratory stand out as particular achievements.

The following sections explain the working principle of MSR plants and point out the benefits and drawbacks of these reactors. Section 2.4 presents the advantages of fluoride salts – the preferred carrier salt option for MSRs. Their physical properties are compared to those of other reactor coolants. Another section addresses some classification criteria that can be used to distinguish between the different reactor designs.

Modern studies favour the use of molten salt fast reactors (MSFR), which is in the focus of investigation in this work. A description of this reactor design is provided in the last part of this chapter.

2.2 Historical Development

Research about molten salt technology for nuclear power applications began in the US after World War II. The US Air Force started a programme to investigate the use of an onboard nuclear power source for aircraft propulsion [5]. In the context of this programme, the Oak Ridge National Laboratory (ORNL) in Tennessee ran the Aircraft Reactor Experiment in 1954 [5]. This 2.5 MW_{th} test reactor employed a molten fluoride carrier salt containing dissolved $\mathrm{UF_4}$ that flowed through BeO moderator blocks in the core [5].

After terminating the nuclear aircraft propulsion programme, research at ORNL focussed on the use of molten salts in nuclear power reactors. In order to investigate the practicability and technology of an MSR for civilian power generation, the Molten Salt Reactor Experiment (MSRE) with 8 MW_{th} power was initiated [5]. In this experimental reactor, the fluoride-based carrier salt flowed through passages in a graphite core [5]. The fuel salt was added in the form of $\mathrm{UF_4}$, first containing $\mathrm{U-235}$, and later $\mathrm{U-233}$ [9]. The MSRE

Figure 2-1: Graphite blocks in the MSRE core [5].

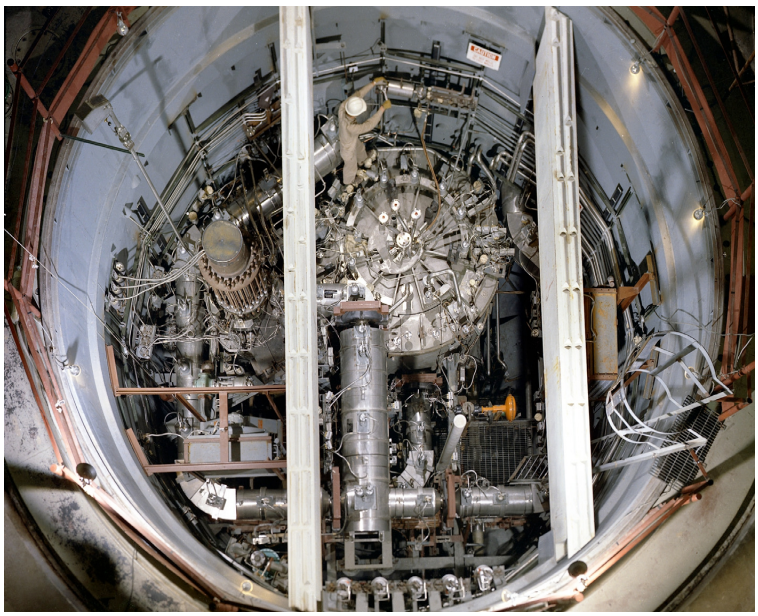

Figure 2-2: Interior of the MSRE containment tank [5].

operated from 1965 to 1969 [5]. One can see photographs of the MSRE facility and its graphite core in Figures 2-1 and 2-2.

With the experience gained from previous MSR research, ORNL initiated the development of a large-scale power reactor – the Molten Salt Breeder Reactor (MSBR). This design was supposed to have a thermal power of 2250 MW_{th} and generate 1000 MW_e of electrical power. The MSBR would breed its own $\mathrm{U-233}$ fuel from $\mathrm{Th-232}$ and a coupled processing plant would remove fission product online [7] [10]. However, it only remained a conceptual design and was never built. In 1976, the United States Atomic Energy Commission stopped the MSR programme at ORNL and decided to focus on the development of liquid metal-cooled fast breeder reactors [11].

After abandoning the programme at Oak Ridge, there was little progress made in MSR research over the following decades [6]. Interest in the MSR concept resurged after the Generation IV International Forum promoted this technology as one of six innovative reactor systems and recommended further research and development in 2002 [4]. In the past two decades research focus has shifted especially towards advanced high-temperature reactors (AHTR) using molten salts as a low-pressure coolant and fast-neutron-spectrum MSRs (MSFR) [12].

2.3 Working Principle of Molten Salt Reactors

The main feature of MSRs is the ulilisation of salt mixtures at such high temperatures that they are molten, i.e. in the liquid state. They are employed as coolants and carrier salts for nuclear fuel particles. The salt compositions contain fissile ($^{233}\mathrm{U}$, $^{235}\mathrm{U}$, $^{239}\mathrm{Pu}$) and fertile isotopes ($^{232}\mathrm{Th}$) as part of salt compounds like $\mathrm{UF_4}$, $\mathrm{PuF_3}$ and $\mathrm{ThF_4}$ [6]. MSRs can operate at temperatures between the melting point of the salt eutectics ($450°\mathrm{C}$ to $550°\mathrm{C}$, depending on the salt) and the working temperature limit for the structural materials used in the reactor components at around $800°\mathrm{C}$ [4].

Figure 2-3 shows an MSR layout draft issued by the General IV International Forum in 2002 [4]. The thermal power generated inside the reactor core is transferred to an intermediate heat exchanger by the molten salt, which circulates through the primary loop. In the heat exchanger a secondary coolant salt gets heated up by the primary coolant salt, which then flows back into the core. The secondary salt passes the heat on to a third loop, which is a Rankine or a Brayton power cycle [6]. A Rankine cycle uses steam as a working fluid to drive a turbine. A coupled generator transforms the rotational energy into electricity. Recent research though suggests the use of a closed Brayton cycle that runs on compressed gases, such as air or helium [4][13]. That would increase efficiency and reduce the risk of a chemical reaction with the coolant salt compared to a steam-driven Rankine cycle [4]. An online chemical processing plant reprocesses the molten salt by removing fission products [14].

Although Figure 2-3 shows some control rods for the core, these are not strictly necessary. The reactivity is easily regulated by online fuel insertion or extraction, and, in case of a shutdown, the core fuel can be drained to subcritical dumb tanks [6].

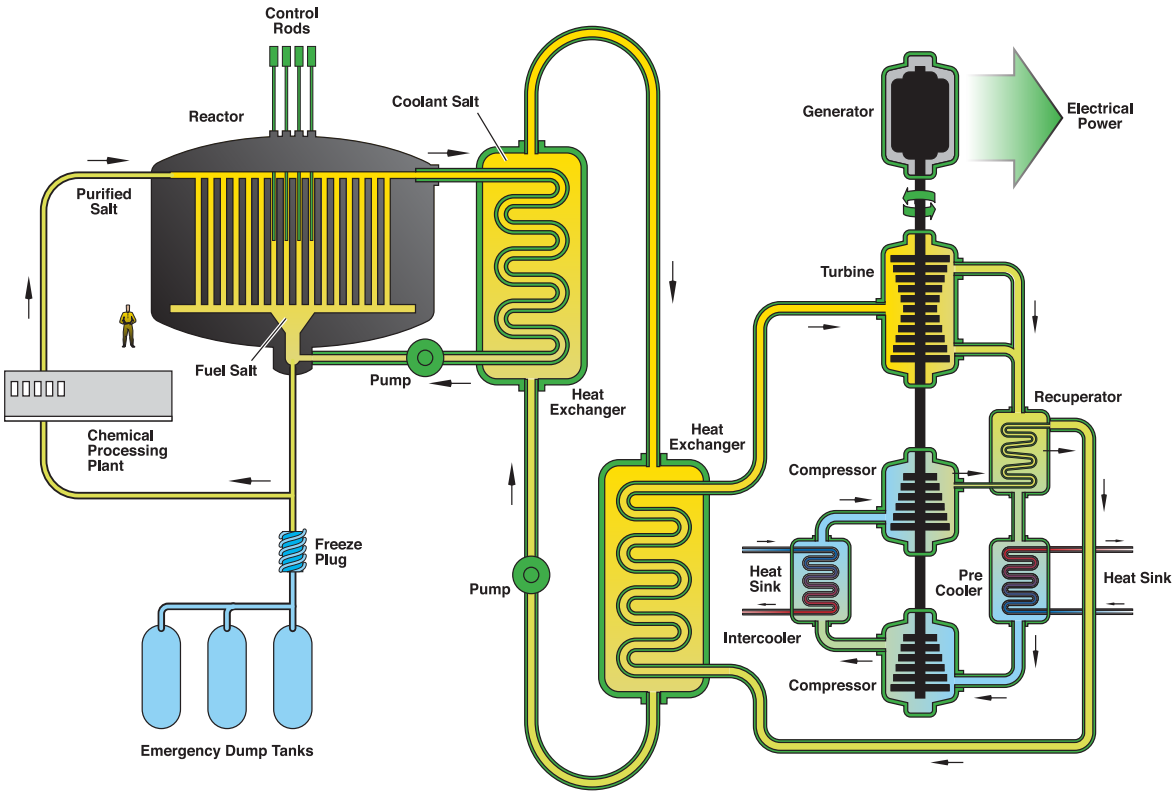

Figure 2-3: Layout of an MSR plant as suggested by the Generation IV International Forum [4].

2.4 Molten Salt Coolants

Fluoride salts are the preferred option for MSR carrier salts because of their chemical stability, radiation resistance, low melting point, compatibility with structural materials and high solubility for the fuel [14]. Especially compositions with LiF and BeF are favourable as lithium and beryllium have small neutron capture cross-sections [13].

Table 2-1 shows some thermodynamical properties of various molten salt compositions and other coolants used in different reactor designs. The most considered carrier salt for MSRs is FLiBe ($\mathrm{LiF\text{-}BeF_2}$) [6]. As can be seen, it has a higher thermal conductivity λ and volumetric heat capacity $\rho \cdot c_p$ than water in conventionally used pressurised water reactors (PWRs). FLiBe's high melting temperature demands the reactor system to operate constantly at high temperatures to avoid freezing. Its high boiling temperature at 1430 °C enables a broad temperature range for the reactor, limited only by the mechanical properties of the structural materials. The kinematic viscosity of FLiBe is also higher than the one of pressurised water, entailing a demand for higher pumping power [14].

Table 2-1: Physical properties of various coolants

Coolant	T_{melt}	T_{boil}	$\rho \cdot c_{\mathrm{p}}$	λ	$\nu \cdot 10^6$	**Reference point**	**Possible application**
	[°C]	[°C]	$[\frac{\mathrm{kJ}}{\mathrm{m^3 \cdot K}}]$	$[\frac{\mathrm{W}}{\mathrm{m \cdot K}}]$	$[\frac{\mathrm{m^2}}{\mathrm{s}}]$		
FLiBe ($\mathrm{LiF\text{-}BeF_2}$)	459	1430	4670	1.0	2.90	$p = 1\,\mathrm{atm}$ $T = 700\,^{\circ}\mathrm{C}$	MSR [13]
FLiNaK ($\mathrm{LiF\text{-}NaF\text{-}KF}$)	454	1610	3820	0.6 - 1.0	1.40	$p = 1\,\mathrm{atm}$ $T = 700\,^{\circ}\mathrm{C}$	MSR [15]
$\mathrm{NaNO_3\text{-}KNO_3}$ [16]	221		2710	0.5	0.79	$p = 1\,\mathrm{atm}$ $T = 500\,^{\circ}\mathrm{C}$	Solar energy applications [17]
Sodium (Na)	98	883	1040	62.0	0.12	$p = 1\,\mathrm{atm}$ $T = 550\,^{\circ}\mathrm{C}$	Sodium-Cooled Fast Reactor [4]
Lead (Pb) [18]	328	1750	1485	18.3	0.16	$p = 1\,\mathrm{atm}$ $T = 550\,^{\circ}\mathrm{C}$ [4]	Lead-Cooled Fast Reactor [4]
Helium (He) [19]			37	0.3	4.56	$p = 9\,\mathrm{MPa}$ $T = 600\,^{\circ}\mathrm{C}$ [4]	Gas-Cooled Fast Reactor [4]
Water ($\mathrm{H_2O}$) [20]	0	340	3973	0.6	0.12	$p = 15\,\mathrm{MPa}$ $T = 300\,^{\circ}\mathrm{C}$ [21]	Pressurised Water Reactor

Data taken from [22] unless indicated otherwise

T_{melt}	melting temperature
T_{boil}	boiling temperature
$\rho \cdot c_p$	volumetric heat capacity
λ	thermal conductivity
ν	kinematic viscosity

2.5 Advantages and Drawbacks

2.5.1 Advantages

MSRs provide a wide variety of advantages compared to conventionally used PWRs:

- Since the fuel is dissolved in the molten salt coolant, the scenario of a reactor core meltdown becomes impossible. Under accident conditions, the reactor fuel can simply be drained into subcritical, passively cooled storage tanks [13].
- Actively cooling a valve below the reactor vessel creates a frozen salt plug. When overheating, the plug will melt and trigger the draining process automatically [23].
- Due to the high melting temperature, the salt naturally freezes when in contact with the ambient temperature [14]. Thus, it has the ability to seal piping leakages and safely contain fission products in the salt compound.
- Operating the molten salts at atmospheric pressure constitutes another significant safety advantage [6]. PWRs work with water pressurised at around 150 bar to ensure that it remains liquid at 300 °C. Because the coolant salts have high boiling temperatures, MSRs do not require pressurisation. This reduces the mechanical stress on the vessel and piping and averts the risk of steam explosions [4].
- MSRs do not require a high excess reactivity since neutron poisons, like xenon and krypton, are continuously removed during operation [24].
- The fissile inventory in the reactor is kept at a low level because additional fuel can quickly be fed into the reactor if needed [14].
- Fewer maintenance shutdowns are required because fuel replacement is carried out online [14].
- Transuranic (TRU) waste may be loaded into the reactor as start-up inventory and will be consumed during operation [6].
- The high operating temperature provides a high energy conversion effiency [24].
- Because molten salts have a high volumetric heat capacity, MSRs have a compact

design [6].

2.5.2 Drawbacks

Some of the challenges that require extra care for the MSR are listed in the following:

- During operation, the coolant salts become contaminated with radioactive fission products, which can react with vessel and piping materials [13]. Therefore much effort is required for salt reprocessing and waste product removal.
- Salt compounds in MSRs have melting temperatures around 450 to 550 °C. Therefore it must be ensured that no area in the reactor cycle falls below this temperature in order to avoid freezing.
- The structural materials of the reactor components are the limiting factor when it comes to high temperatures [13]: Further research must look into how mechanical properties and stability change under the influence of radiation and heat [14].
- Corrosion due to salt-metal-contact is another issue that needs further investigation [14].
- The lithium isotope $^{6}\mathrm{Li}$ in the coolant salt can be transmuted into tritium [13]. Tritium can permeate through the vessel alloy, change its structural integrity and pose a risk to the environment [25].

2.6 Classification

It is necessary to distinguish the MSR concept from the one of the AHTR. In an MSR, the molten salt acts as coolant and fuel carrier salt alike, i.e. the fissile and fertile isotopes are dissolved in the molten salt [13]. On the other hand, AHTRs are reactors with solid, coated fuel particles in the core that use molten salts merely as a coolant [12]. The AHTR is therefore fundamentally different from the considered MSR notion of this thesis and not further discussed.

Depending on the fuel design, MSRs can be grouped into breeders, converters and burn-

ers. While fission reactions occur in the core, fertile isotopes can get transmuted into fissile particles. Breeding reactors employ this effect to produce more fissile fuel than they consume [13], giving them a breeding ratio greater than unity. Many MSR breeder designs apply the thorium-uranium fuel cycle that uses fertile $^{232}\mathrm{Th}$ to breed fissile $^{233}\mathrm{U}$ according to Eq. 2-1 [13]:

$$ {}^{1}_{0}\mathrm{n} + {}^{232}_{90}\mathrm{Th} \longrightarrow {}^{233}_{90}\mathrm{Th} \xrightarrow{\beta^- \, (\mathrm{t}_{1/2}=22\,\mathrm{min})} {}^{233}_{91}\mathrm{Pa} \xrightarrow{\beta^- \, (\mathrm{t}_{1/2}=27\,\mathrm{d})} {}^{233}_{92}\mathrm{U} \; . \tag{2-1} $$

Since the breeding ratio is greater than unity, only $^{232}\mathrm{Th}$ needs to be reloaded into the core in order to obtain enough fuel to keep the fission reaction running [14]. Using thorium has multiple advantages: It is at least three times more abundant than uranium, and breeders using the thorium-uranium fuel cycle produce less TRU waste than conventional reactor designs [6].

Converter reactors have a breeding ratio smaller than unity, meaning they do not gain enough fissile fuel to sustain their operation [13]. Fresh fissile material needs to be added regularly to compensate for the fuel burnup [6]. A third MSR type refers to molten salt burner reactors. These reactors operate on actinides from spent nuclear fuel, thereby transmuting the long-lived radioactive elements [14].

The $^{233}\mathrm{U}$ isotope bred in the reactor is able to undergo nuclear fission after neutron absorption. This releases energy, fission products and further neutrons, which interact with other fertile and fissile particles [26]. Depending on the utilised neutron spectrum for breeding and fission, MSRs can be thermal or fast reactors. Thermal MSRs use a moderator to slow down neutrons. The moderator material in this case is often graphite, which needs to be replaced regularly due to irradiation damage [13]. Fast spectrum reactors operate on high-energy neutrons. They do not use a moderator and therefore have a simpler core design [13].

Figure 2-4 provides a summary of the discussed MSR classification.

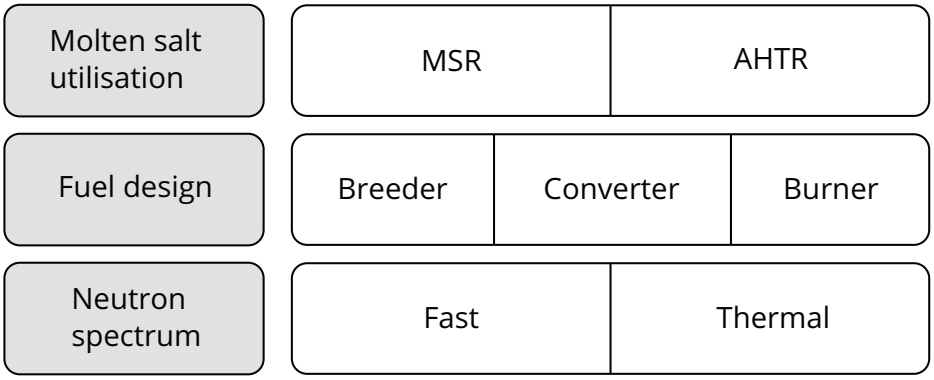

Figure 2-4: MSR classification overview.

2.7 Molten Salt Fast Reactor Design

The focus of the stability analysis in this work is on the MSFR – a fast spectrum breeding reactor. The concept described hereafter follows the reactor design discussed in [27] and [28].

Two fuel options are considered for the initial reactor inventory: $^{233}\mathrm{U}$ or TRU waste. The fuel salt in the core is a compound of LiF, $\mathrm{ThF_4}$ and a fluoride salt with either $^{233}\mathrm{U}$ or TRU elements (plutonium and minor actinides). The melting temperature of the eutectic salt mixture lies at around $T = 550\,^{\circ}\mathrm{C}$. The analysed reactor model in the following chapters considers fresh $^{233}\mathrm{U}$ fuel in the core. Reference data for the characteristics of the proposed MSFR design and initial reactor inventories are provided in Table 2-2.

Figure 2-5 depicts the proposed structure and components of the MSFR design. The circulating fuel gets fissioned within the core as the molten salt flows upwards. It leaves the core passing through salt-bubble separators for the extraction of fission products. In the external part, the salt streams downwards passing the heat on to a secondary coolant salt in the heat exchangers. It gets reinjected at the bottom of the core. The core contains half the salt volume and the external part of the cycle, which consists of sixteen identical modules around the core, the other half. The secondary salt transfers the heat to a tertiary cycle, where it is used to generate electricity (see also Section 2.3).

A fertile blanket forms axial reflectors that protect the external modules with the heat exchangers and pumps. The blanket contains the fertile $\mathrm{LiF\text{-}ThF_4}$ salt compound used for the breeding of fissile $^{233}\mathrm{U}$. It captures most of the escaping neutrons. The remaining

Table 2-2: Characteristics of the proposed MSFR design [27][28]

		^{233}U-started	TRU-started
Fuel salt composition		$\mathrm{LiF\text{-}ThF_4\text{-}}^{233}\mathrm{UF_4}$	$\mathrm{LiF\text{-}ThF_4\text{-}(Pu\text{-}MA)F_3}$
Fertile salt composition in the blanket		$\mathrm{LiF\text{-}ThF_4}$	
Thermal Power		$3000\,\mathrm{MW_{th}}$	
Operating Temperature		650 - $750\,^{\circ}\mathrm{C}$	
Thorium consumption		$1110\,\frac{\mathrm{kg}}{\mathrm{a}}$	
^{233}U production		$93\,\frac{\mathrm{kg}}{\mathrm{a}}$	$188\,\frac{\mathrm{kg}}{\mathrm{a}}$
Breeding ratio		1.085	
Initial inventory	Th	$38\,300\,\mathrm{kg}$	$30\,600\,\mathrm{kg}$
	$^{233}\mathrm{U}$	$5060\,\mathrm{kg}$	
	Pu		$11\,200\,\mathrm{kg}$
	Np		$800\,\mathrm{kg}$
	Am		$680\,\mathrm{kg}$
	Cm		$115\,\mathrm{kg}$

MA: minor actinides

neutron flux is absorbed by a surrounding $\mathrm{B_4C}$ protection layer. At the bottom and the top of the vessel, there are nickel-based axial reflectors.

Keeping track of the molten salt composition is crucial as neutron poisons need to be removed, and the right amount of fuel in the salt has to be provided. Thus an on-site salt processing system is necessary. A gaseous extraction scheme injects helium bubbles at the bottom of the core in order to trap non-soluble and gaseous fission products in the molten salt. The captured substances are removed from the salt in salt-bubble separators at the core outlets. An additional purification measure is the periodic withdrawal of salt portions for the off-line extraction of lanthanide elements. The reprocessed fuel salt is subsequently fed back into the core.

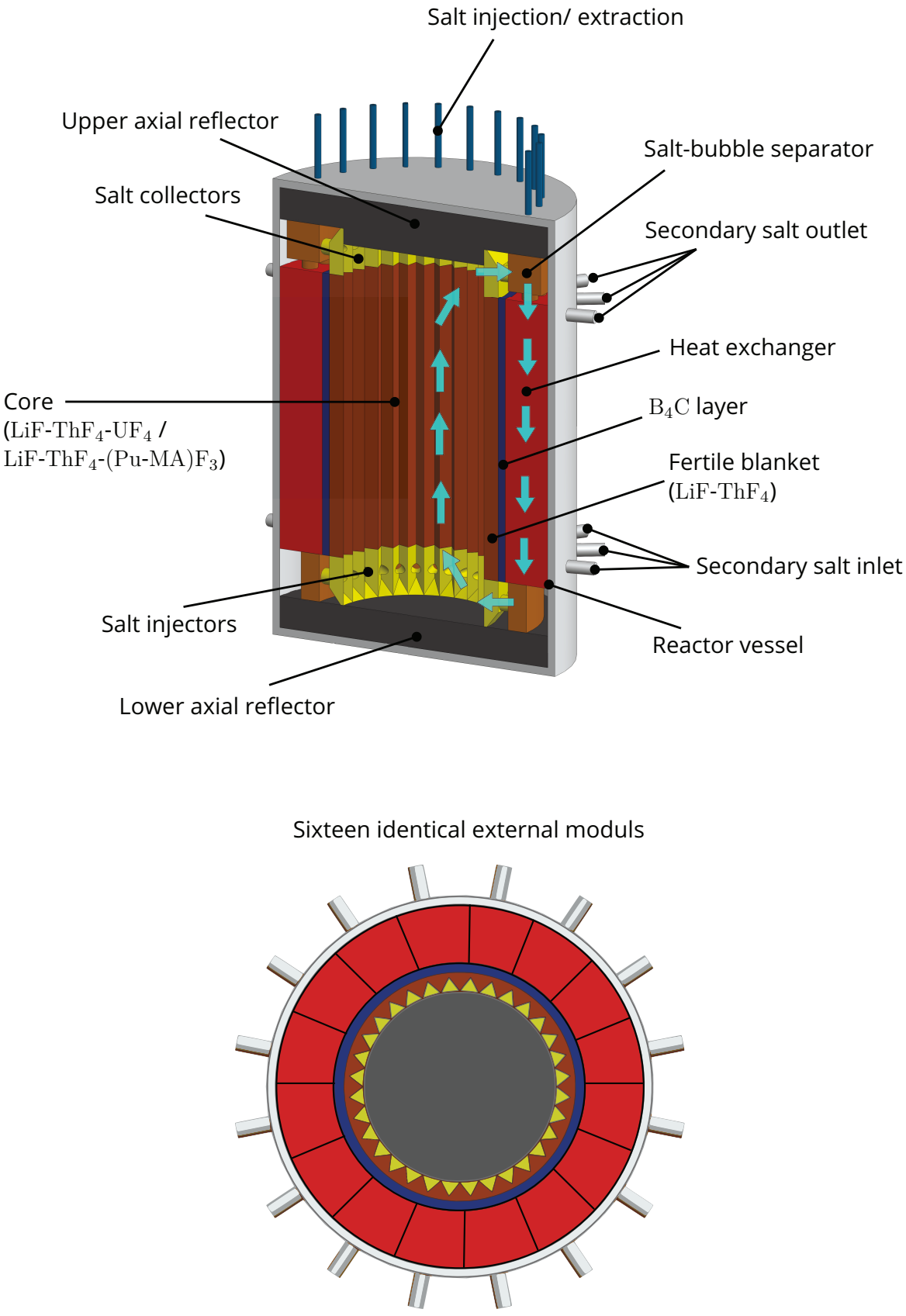

Figure 2-5: Structure of the proposed MSFR design (adopted from [27], edited).

3 STABILITY CHARACTERISTICS OF DYNAMICAL SYSTEMS

3.1 Introduction

This chapter provides an overview of the stability considerations concerning dynamical systems. First, essential terms for the description of dynamical systems are explained, and different definitions of stability are introduced. Two solution types of dynamical systems are then outlined in more detail: fixed-point solutions and periodic solutions. Some methods for determining their stability are presented, and different types of bifurcation phenomena are discussed.

3.2 Dynamical Systems

A dynamical system is characterised by a state that is described by its corresponding state variables. The state vector $\boldsymbol{x}(t) \in \mathbb{R}^{\mathrm{n}}$ combines all state variables of the system [29]. The state changes with time t according to a set of rules, which can be declared, e.g. by ordinary differential equations (ODEs), partial differential equations or maps [30].

The explanations hereafter consider a continuous-time dynamical system, which can be described by a set of ODEs. Said system is assumed to be autonomous, i.e. it is not explicitly time-dependent:

$$\dot{\boldsymbol{x}} = \boldsymbol{F}(\boldsymbol{x}; \boldsymbol{c}) \quad (\boldsymbol{x} \in \mathbb{R}^{\mathrm{n}}, \boldsymbol{c} \in \mathbb{R}^{\mathrm{m}}) \,, \tag{3-1}$$

whereas a nonautonomous system is explicitly dependent on time t:

$$\dot{\boldsymbol{x}} = \boldsymbol{F}(\boldsymbol{x}, t; \boldsymbol{c}) \,. \tag{3-2}$$

In both cases, the vector $\boldsymbol{c}$ contains a set of time-independent quantities that control the evolution of the dynamical system [29]. They are referred to as control parameters and represent certain design or operational features of the dynamical system [30].

In the following, some more definitions for notions relating to the description and beha-

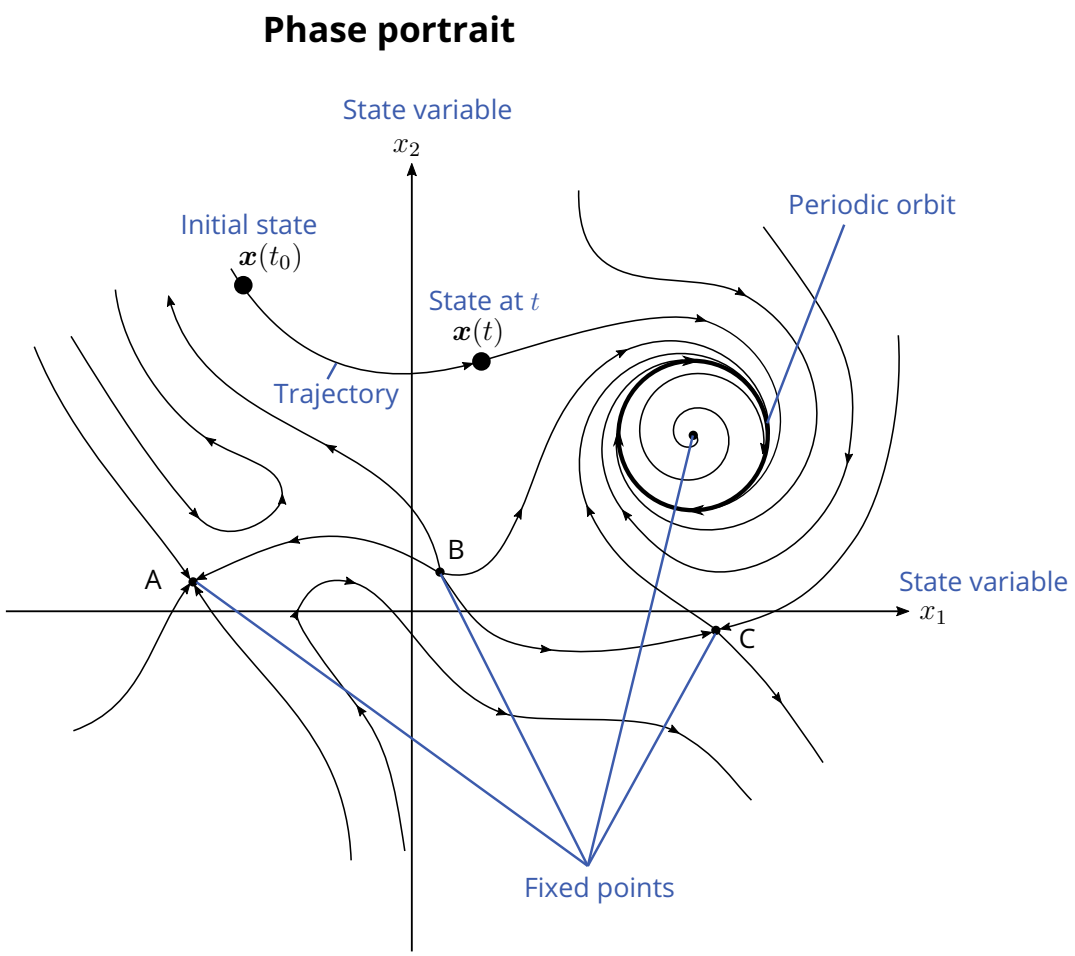

Figure 3-1: Generic phase portrait illustrating the vocabulary used for the description of dynamical systems.

viour of dynamical systems are given. Figure 3-1 provides an illustrated overview of the used terms.

The phase space $X \subset \mathbb{R}^n$, also called state space, contains the entirety of all possible states of system 3-1 with $\boldsymbol{x} \in X$. The flow $\phi_t \equiv \phi(t) : \mathbb{R}^n \to \mathbb{R}^n$ specifies the evolution of the state variables $\boldsymbol{x}(t)$ in the phase space with time t [31][32]. Starting at $\boldsymbol{x}(t_0)$, the flow ϕ_t leads to

$$\phi_t\Big(\boldsymbol{x}(t_0)\Big) = \boldsymbol{x}(t) \; . \tag{3-3}$$

The curves in phase space that represent the solutions of system 3-1 are called trajectories or orbits [29]. They connect various possible initial states $\boldsymbol{x}(t_0)$ with the states $\boldsymbol{x}(t)$ at time t following the flow ϕ_t in the direction of evolution [8]. An ensemble of trajectories forms a phase portrait of the system [29]. It represents a schematic illustration of a phase

space projection and contains a great amount of information that helps with estimating the dynamical behaviour of a system.

The solutions of the dynamical system 3-1 may asymptotically approach a subset of the phase space $A \subset X$ for $t \to \infty$ or $t \to -\infty$ [32]. This subset may correspond to a fixed point or a periodic orbit. A fixed point $\boldsymbol{X}_0$, also called equilibrium point, is a steady-state solution defined as [31]

$$\phi_t(\boldsymbol{X}_0) = \boldsymbol{X}_0 \text{ for all } t. \tag{3-4}$$

The flow at the initial state $\boldsymbol{x}(t_0) = \boldsymbol{X}_0$ leads to the state $\boldsymbol{X}_0$ itself [31].

In contrast, a periodic orbit or cycle Γ_0 is a dynamic, periodic solution. Each point $\boldsymbol{x}_0 \in \Gamma_0$ satisfies [29][31]

$$\begin{gathered} \phi_{t+T}(\boldsymbol{x}_0) = \phi_t(\boldsymbol{x}_0) \text{ with } T > 0, \text{ for all } t. \\ \text{and } \phi_{t+\tau}(\boldsymbol{x}_0) \neq \phi_t(\boldsymbol{x}_0) \text{ with } 0 < \tau < T, \text{ for all } t. \end{gathered} \tag{3-5}$$

For a periodic orbit, the state variables at a point $\boldsymbol{x}_0$ will return to that very point with every minimal period T after passing along the closed curve Γ_0 in phase space [31].

3.3 Stability Concepts

3.3.1 Introduction

The concept of 'stability' has various definitions, a few of which will be listed in this section. This work applies the stability definition according to Lyapunov to fixed-point solutions and the one according to Poincaré to periodic solutions.

3.3.2 Lagrange Stability (Bounded Stability)

A solution $\boldsymbol{u}(t)$ is said to be boundedly stable if $\|\boldsymbol{u}\| \leq M$ with $M < \infty$ for all t [30]. Thus, all state variables of $\boldsymbol{u}(t)$ have to be confined in order to fulfil this condition, and so none of them can go to infinity. This concept is the weakest definition of stability.

3.3.3 Lyapunov Stability

The notion of stability according to Lyapunov distinguishes between uniformly stable or asymptotically stable.

A solution $\boldsymbol{u}(t)$ is called uniformly stable if there exists a small number $\epsilon > 0$ with a corresponding number $\delta(\epsilon) > 0$ such that any other nearby solution $\boldsymbol{v}(t)$ with $\|\boldsymbol{u}(t_0) - \boldsymbol{v}(t_0)\| < \delta(\epsilon)$ remains close to $\boldsymbol{u}(t)$ at all time $t > t_0$ such that $\|\boldsymbol{u}(t) - \boldsymbol{v}(t)\| < \epsilon$ [30].

That means that any trajectories initiated close to solution $\boldsymbol{u}(t)$ will remain in its proximity for all $t > t_0$. Figure 3-2 illustrates the above definition.

A solution $\boldsymbol{u}(t)$ is called asymptotically stable according to Lyapunov if it is uniformly stable and nearby solutions $\boldsymbol{v}(t)$ satisfy [30]

$$\lim_{t\to\infty} \|\boldsymbol{u}(t) - \boldsymbol{v}(t)\| \to 0 \ .$$

In case of a fixed-point solution, one substitutes $\boldsymbol{u}(t)$ with $\boldsymbol{u}_0$. All trajectories close to $\boldsymbol{u}_0$ will remain so (uniformly stable) or tend towards it (asymptotically stable) for $t > t_0$ as can be seen in Figure 3-3.

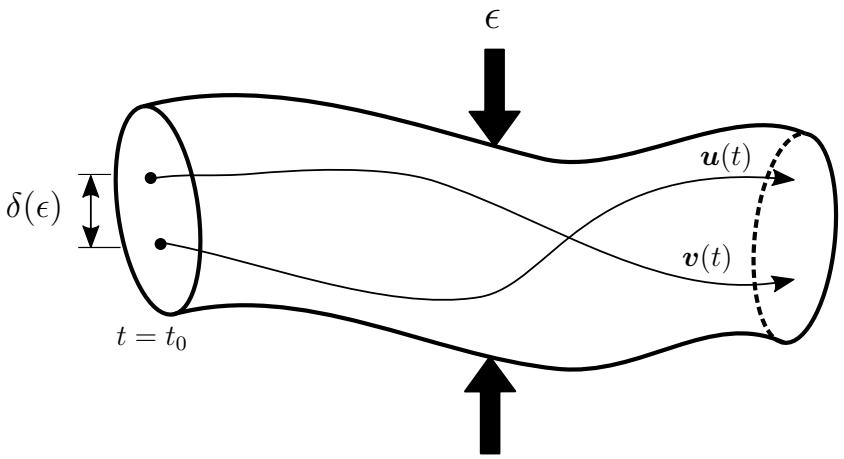

Figure 3-2: Illustrated description of Lyapunov stability for two time-dependent solutions (adopted from [30], edited).

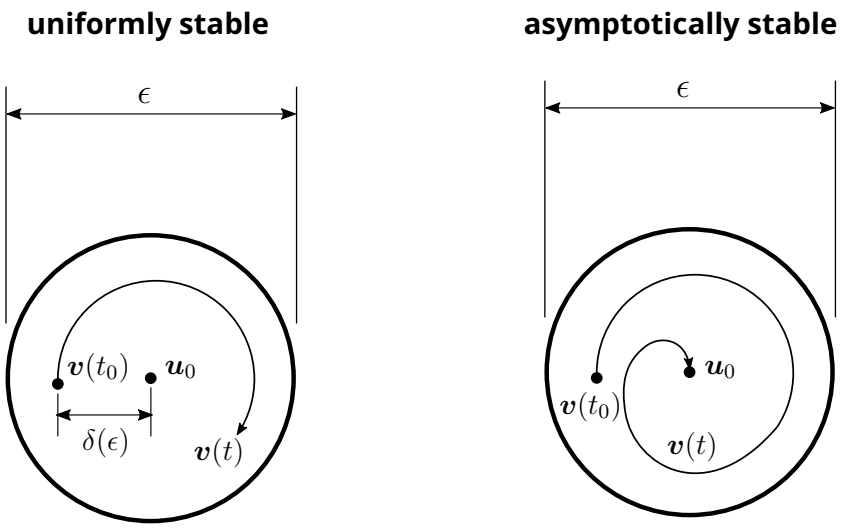

Figure 3-3: Illustrated description of Lyapunov stability for a fixed-point solution (adopted from [32], edited).

3.3.4 Poincaré Stability (Orbital Stability)

According to the definition of asymptotic Lyapunov stability, periodic solutions correspond to an unstable system state. This fact can be explained by considering the trajectories shown in Figure 3-4.

The curves Γ_1 and Γ_2 represent the trajectories of the periodic solutions $\boldsymbol{u}(t)$ and $\boldsymbol{v}(t)$. The solutions $\boldsymbol{u}(t_0)$ and $\boldsymbol{v}(t_0)$ are initially in each other's proximity at $t = t_0$. After the time $t = \tau$ has passed, the solutions $\boldsymbol{u}(\tau)$ and $\boldsymbol{v}(\tau)$ have a much larger distance from each other owing

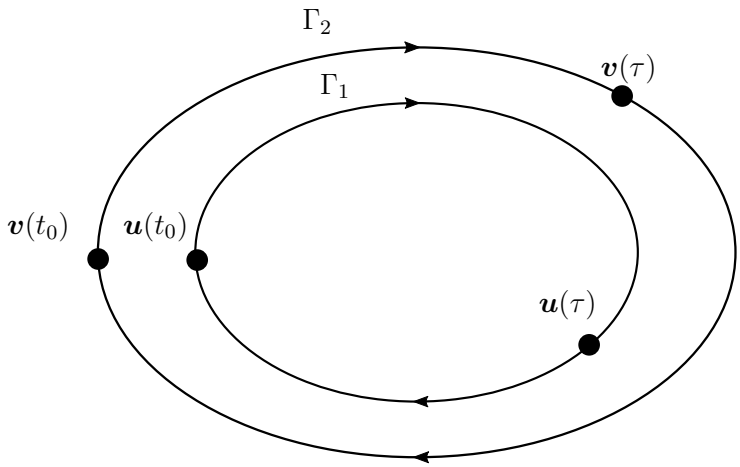

Figure 3-4: Evolution of two periodic solutions along close orbits (adopted from [29], edited).

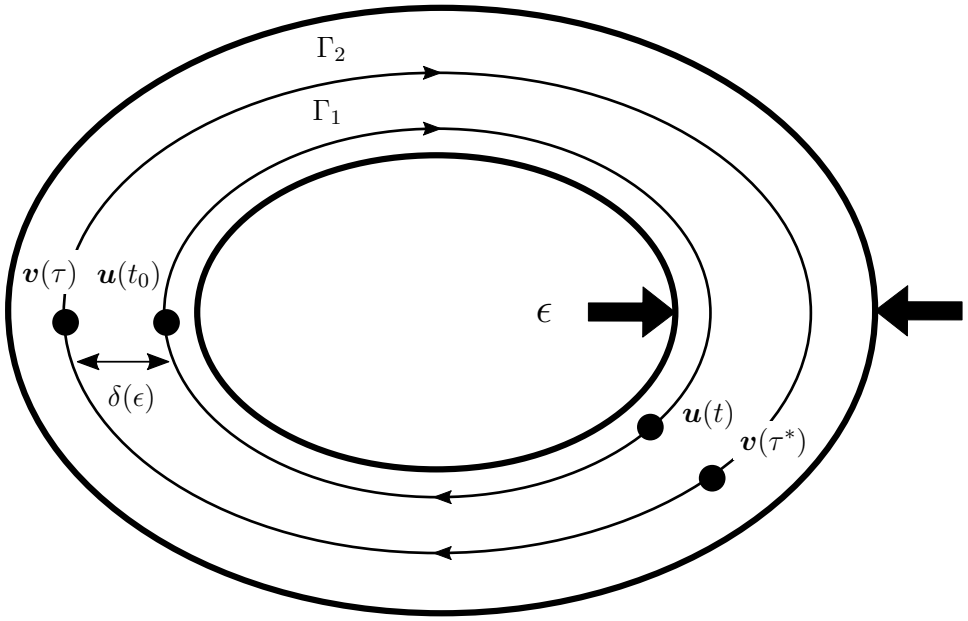

Figure 3-5: Illustrated description of Poincaré stability for two periodic solutions.

to the different orbitally velocities of Γ_1 and Γ_2. Despite the two trajectories being close, the solutions $\boldsymbol{u}(t)$ and $\boldsymbol{v}(t)$ do not remain close to each other as they evolve differently in time. Hence, they would not be considered asymptotically stable following the definition of Lyapunov stability [29]. However, in case ϵ is chosen large enough, the periodic solution $\boldsymbol{u}(t)$ can be considered a stable state according to the definition of uniform Lyapunov stability.

As a consequence, the concept of Poincaré stability is explicitly introduced for periodic solutions and takes their dynamic evolution into account. Let $\boldsymbol{u}(t)$ move along the orbit Γ_1 and $\boldsymbol{v}(t)$ along the orbit Γ_2. The orbit Γ_1 is called orbitally stable if there exists a small number $\epsilon > 0$ with a corresponding number $\delta(\epsilon) > 0$ such that if $\|\boldsymbol{u}(t_0) - \boldsymbol{v}(\tau)\| < \delta(\epsilon)$ for some τ, there is always a $\tau^*(\tau)$, for which $\|\boldsymbol{u}(t) - \boldsymbol{v}(\tau^*)\| < \epsilon$, for $t > t_0$ [29][30].

The definition signifies that the solutions $\boldsymbol{u}(t)$ and $\boldsymbol{v}(t)$ evolve at different time scales following trajectories that are close to each other (see Figure 3-5).

The orbit Γ_1 is said to be asymptotically stable according to Poincaré if orbit Γ_2 tends towards Γ_1 for $t \to \infty$ [29].

3.4 Fixed-Point Solutions

3.4.1 Stability Analysis of Fixed-Point Solutions

A fixed-point solution defined by Eq. 3-4 is an equilibrium state of system $\dot{\boldsymbol{x}} = \boldsymbol{F}(\boldsymbol{x}; \boldsymbol{c})$ (3-1) [29]. Thus, the vector field $\boldsymbol{F}$ at a fixed point $\boldsymbol{X}_0$ equals

$$\boldsymbol{F}(\boldsymbol{X}_0; \boldsymbol{c}) = \boldsymbol{0} \ . \tag{3-6}$$

For the following considerations, system 3-1 is assumed to be a nonlinear one. A time-continuous, nonlinear system is characterised by state variables whose dynamic behaviour is described by nonlinear ODEs. In a system of nonlinear equations, a change in one variable leads to a nonproportional change in one or several of the other variables [30].

A nonlinear dynamical system can be linearised in the vicinity of a fixed point $\boldsymbol{X}_0$ as described hereafter [29]. For a small deviation $\delta\boldsymbol{x}$ from the fixed point $\boldsymbol{X}_0$, Eq. 3-6 leads to

$$\delta\dot{\boldsymbol{x}} = \boldsymbol{F}(\boldsymbol{X}_0 + \delta\boldsymbol{x}; \boldsymbol{c}) \ . \tag{3-7}$$

Using a first-order Taylor series approximation, Eq. 3-7 can be written as

$$\delta\dot{\boldsymbol{x}} = D_{\boldsymbol{x}}\boldsymbol{F}(\boldsymbol{X}_0; \boldsymbol{c})\delta\boldsymbol{x} = \boldsymbol{J}(\boldsymbol{X}_0; \boldsymbol{c})\delta\boldsymbol{x} \ . \tag{3-8}$$

Matrix $\boldsymbol{J}$ is called the Jacobian matrix and its elements are the partial derivatives of $\boldsymbol{F}$:

$$\boldsymbol{J}(\boldsymbol{X}_0; \boldsymbol{c}) = \begin{pmatrix} \frac{\delta F_1}{\delta x_1} & \cdots & \frac{\delta F_1}{\delta x_n} \\ \vdots & \ddots & \vdots \\ \frac{\delta F_n}{\delta x_1} & \cdots & \frac{\delta F_n}{\delta x_n} \end{pmatrix} \ . \tag{3-9}$$

The solution of the linearised ODE system 3-8 can be obtained by using the eigenvalues λ_i of the Jacobian matrix and their corresponding eigenvectors $\boldsymbol{p}_i$. For n distinct eigenvalues and linearly independent eigenvectors, the general solution equals

$$\delta\boldsymbol{x} = \sum_{i=1}^{n} a_i \mathrm{e}^{\lambda_i t}\boldsymbol{p}_i \tag{3-10}$$

with the constants a_i satisfying the initial conditions [32]. As the eigenvalues λ_i appear in the exponents of solution 3-10, they play a crucial part in its time-depending evolution.

For illustration of the different types of fixed points, references are made to points in Figure 3-1 in the following. If none of the eigenvalues has a zero real part, the associated fixed point $\boldsymbol{X}_0$ is said to be hyperbolic [33]. This fixed point is asymptotically stable if the real parts $\mathrm{Re}(\lambda_i)$ of the eigenvalues are negative. In this case, it equals a sink in phase space (Point A). On the other hand, if there are eigenvalues of the Jacobian matrix with a positive real part, the corresponding fixed point is an unstable one. In case all eigenvalues have positive real parts, the fixed point represents a source (Point B). If there are some eigenvalues having positive real parts and others having negative real parts, the analysed point is called a saddle point (Point C) [29].

The phase portraits of two dynamical systems are topologically equivalent in a certain region if both can be related by an orientation-preserving, continuous map in this region [30]. The Hartman-Grobman theorem implies that, in case $\boldsymbol{X}_0$ is a hyperbolic fixed point, there is some surrounding neighbourhood, in which the trajectories of a nonlinear system are qualitatively similar to those of the linearised one [32]. Both systems are considered to be locally topologically equivalent regarding the vicinity of the fixed point. Hence, if a hyperbolic fixed point of the linearised system is stable, the corresponding fixed point of the nonlinear system is as well in a certain domain. The same principle applies for unstable fixed points.

The Hartman-Grobman theorem allows the local stability analysis of fixed points of nonlinear systems by means of linearisation and eigenvalue monitoring. However, the theorem does not specify the size of the topologically equivalent region [29]. If $\boldsymbol{X}_0$ is a nonhyperbolic fixed point, i.e. at least one eigenvalue of the Jacobian matrix has a real part equal to zero, the Hartman-Grobman theorem does not apply. In this case, one cannot provide any stability information with the help of the linearised system, and other investigation techniques are required. Such methods could involve the direct numerical solution of the dynamical system or bifurcation analysis methods [8].

3.4.2 Bifurcations of Fixed-Point Solutions

A bifurcation occurs when the phase portrait changes qualitatively into a new portrait, which is not topologically equivalent, under the variation of one or more control parameters [30]. This may include a change in the type and number of solutions [29]. The value of a control parameter $c_k \in \boldsymbol{c}$ at which a bifurcation occurs is called critical parameter value $c_{k,\mathrm{c}}$. Figure 3-6 shows the phase portrait of an exemplary dynamical system before and after a critical parameter value of this system has been passed.

As the control parameters of a dynamical system are changed gradually such that the values for each step can be considered constants, an associated hyperbolic fixed point may become nonhyperbolic at a critical parameter value. If the phase portrait around that fixed point changes its qualitative appearance after passing this value, a bifurcation of the fixed point has occurred. There are different types of bifurcations for fixed points, such as saddle-node, pitchfork, transcritical and Hopf bifurcations. The framework regarding stability analyses in this study focusses on the detection of Hopf bifurcations. Therefore this type is explained in detail hereafter.

The fixed-point solution $\boldsymbol{X}_0$ of a dynamical system $\boldsymbol{F}$, for which $\boldsymbol{F}(\boldsymbol{X}_0; \boldsymbol{c}) = \boldsymbol{0}$, is subjected to a Hopf bifurcation at a critical value $c_{k,\mathrm{c}}$ of parameter c_k if the following criteria are satisfied [32]:

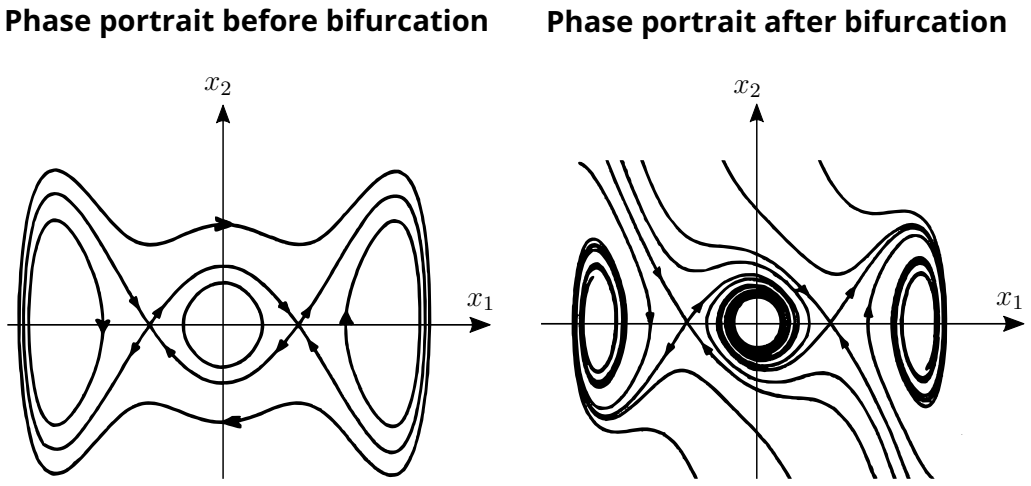

Figure 3-6: Phase portrait of an exemplary dynamical system before and after a bifurcation has occurred (adopted from [29], edited).

1. The Jacobian matrix $\boldsymbol{J}(\boldsymbol{X}_0; c_{k,\mathrm{c}})$ has one pair of purely complex conjugate eigenvalues $\lambda_j(c_{k,\mathrm{c}}) = 0 \pm \mathrm{i}\omega$ for $\lambda_j \in \{\lambda_1 \dots \lambda_n\}$ and $\omega > 0$, with all other eigenvalues having nonzero real parts.

2. $\frac{\partial}{\partial c_k}\mathrm{Re}\Big(\lambda_j(c_{k,\mathrm{c}})\Big) \neq 0$.

When a fixed-point solution undergoes a Hopf bifurcation, a periodic solution with an oscillation period $T = \frac{2\pi}{\omega}$ emerges at $c_{k,\mathrm{c}}$ [29]. At the same time the fixed-point solution changes its local stability characteristics [33]. It can be distinguished between sub- and supercritical Hopf bifurcations.

In case of a supercritical Hopf bifurcation, a stable fixed-point solution bifurcates into a stable periodic solution (see Section 3.3.4 Poincaré stability) and a coexisting unstable fixed point after passing the critical parameter value $c_{k,\mathrm{c}}$ [29]. The local change of a fixed-point or periodic solution in phase space depending on the value of a control parameter can be depicted in a bifurcation diagram. Here, a projection of the phase space around the studied solution follows the varied parameter [31]. Figure 3-7 shows the bifurcation diagram for a supercritical Hopf bifurcation.

When a stable fixed-point solution exists beside an unstable periodic solution, and they both merge into an unstable fixed point when passing the critical parameter value $c_{k,\mathrm{c}}$, the associated Hopf bifurcation is called subcritical [29]. A generic bifurcation diagram for a subcritical Hopf bifurcation is depicted in Figure 3-8.

In the frame of this work, the so-called March-Leuba system is utilised to practise the handling of the numerical bifurcation software MatCont. This ODE system is based on a boiling water reactor model and was presented by March-Leuba and his colleagues in 1986 [34]. The corresponding equations and control parameters can be found in Appendix A. Figure 3-9 shows a MatCont plot of a Hopf bifurcation of the March-Leuba system as an application example of bifurcation analysis.

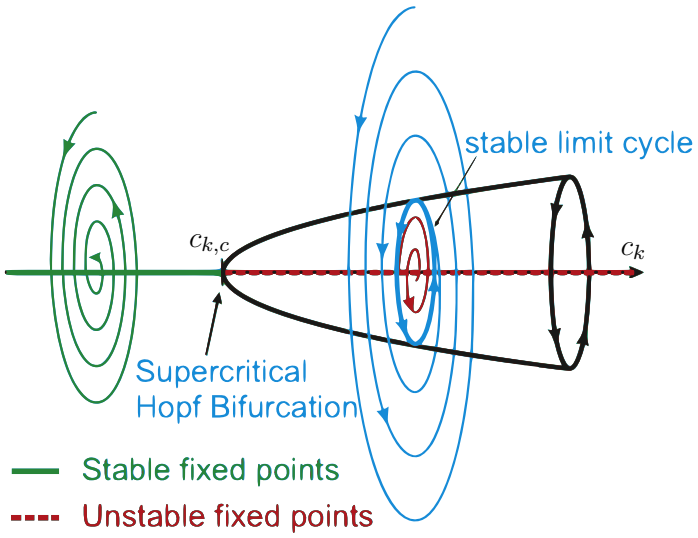

Figure 3-7: Bifurcation diagram for a generic supercritical Hopf bifurcation (adopted from [8]).

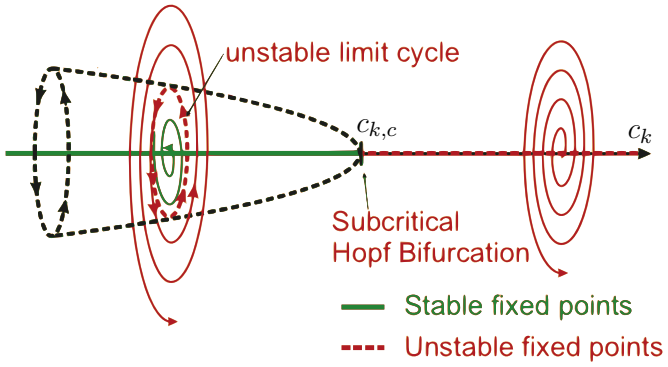

Figure 3-8: Bifurcation diagram for a generic subcritical Hopf bifurcation (adopted from [8]).

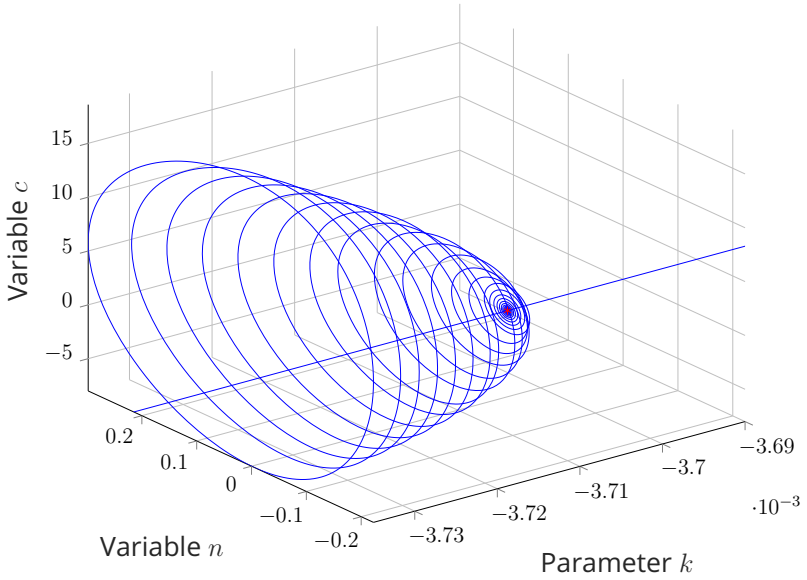

Figure 3-9: MatCont plot of a 3D bifurcation diagram showing a Hopf bifurcation of the March-Leuba system (Appendix A).

3.5 Periodic Solutions

3.5.1 Stability Analysis of Periodic Solutions

A periodic solution satisfies Eq. 3-5 and is represented by a closed orbit Γ_0 in phase space. A periodic orbit that is isolated in phase space with no other periodic orbit in its proximity is called a limit cycle [29]. All solutions close to a limit cycle tend towards it, either for $t \to \infty$, in case of an asymptotically stable limit cycle, or for $t \to -\infty$, in case of an unstable limit cycle [29].

Poincaré Maps

The stability of periodic solutions can be studied with the help of Poincaré sections and maps. For an n-dimensional dynamical system, a Poincaré section, in geometrical terms, is a smooth hypersurface Σ of dimension $n-1$ that intersects the periodic orbit Γ_0 at the point $\boldsymbol{X}_0 \in \Gamma_0$ transversally, i.e. at a nonzero angle [33]. Figure 3-10 illustrates the definition of a Poincaré section.

The limit cycle Γ_0 intersecting Σ at $\boldsymbol{X}_0$ arrives at exactly the same point after the period

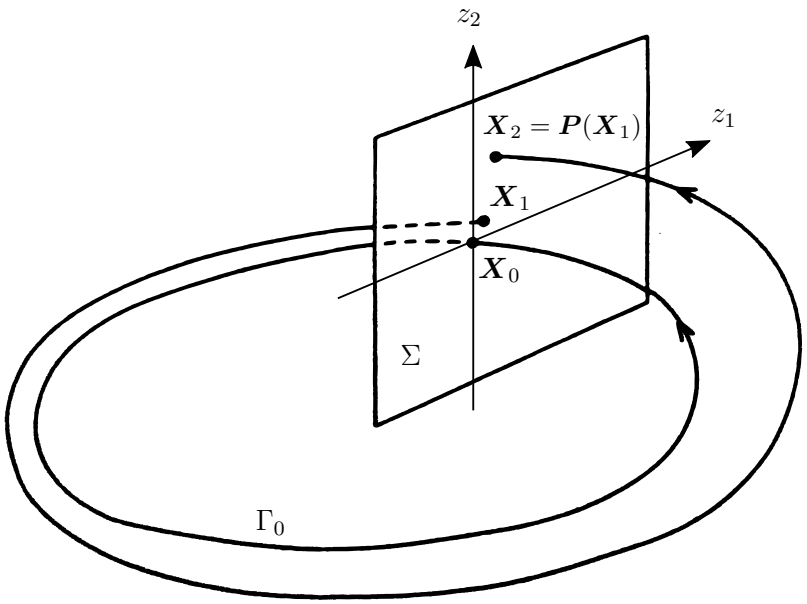

Figure 3-10: Illustration of a Poincaré section (adopted from [33], edited).

T [31]. Another trajectory close to the limit cycle Γ_0 may intersect Σ at $\boldsymbol{X}_1$ close to $\boldsymbol{X}_0$. Following the trajectory to its first return to section Σ gives another intersection point $\boldsymbol{X}_2$ near $\boldsymbol{X}_1$. The map describing the local evolution of one intersection point to a successive intersection point is called Poincaré map $\boldsymbol{P} : \Sigma \to \Sigma$ [29], such that

$$\boldsymbol{X}_j \mapsto \boldsymbol{X}_{j+1} = \boldsymbol{P}(\boldsymbol{X}_j) \; . \tag{3-11}$$

The intersection points on a Poincaré section can also be expressed by using local coordinates $\boldsymbol{z} \in \mathbb{R}^{n-1}$. These coordinates are specified in such a way that $\boldsymbol{Z}_0 = \boldsymbol{0}$ for the fixed intersection point $\boldsymbol{X}_0$ (cf. Figure 3-10) [31]. With regard to the local coordinates $\boldsymbol{z}$, the Poincaré map describes the evolution of subsequent intersection points for trajectories near Γ_0 as

$$\boldsymbol{Z}_j \mapsto \boldsymbol{Z}_{j+1} = \boldsymbol{P}(\boldsymbol{Z}_j) \; . \tag{3-12}$$

The stability of limit cycle Γ_0 can then be determined with the help of the Jacobian matrix $\boldsymbol{J}(\boldsymbol{Z}_0; \boldsymbol{c}) = D_{\boldsymbol{z}}\boldsymbol{P}(\boldsymbol{Z}_0; \boldsymbol{c})$. This matrix consists of the partial derivatives $\frac{\delta P_i}{\delta z_j}$ for $i, j = 1 \ldots (n-1)$ at the fixed intersection point $\boldsymbol{Z}_0$ correspondingly to Eq. 3-9. The limit cycle Γ_0 is asymptotically orbitally stable if all eigenvalues of the Jacobian matrix are inside the unit circle in the complex plane (see Figure 3-11) [29]. If one or more eigenvalues lie outside the unit circle, the periodic solution is unstable.

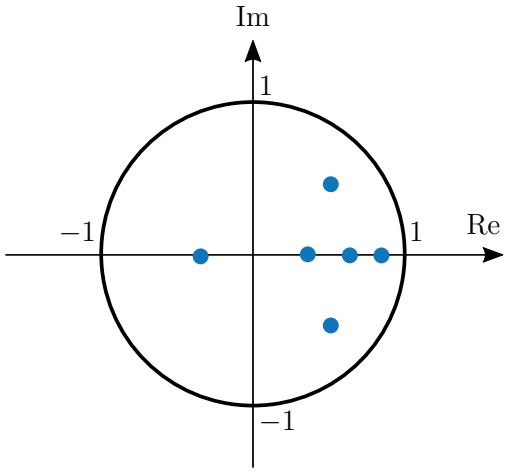

Figure 3-11: Eigenvalues of the Jacobian matrix $\boldsymbol{J}(\boldsymbol{Z}_0; \boldsymbol{c})$ for a generic stable limit cycle.

Floquet Theory

Another method for determining the stability of a periodic solution is based on the Floquet theory and evaluates the so-called monodromy matrix. The derivation of this matrix in the context of Floquet theory is explained in Appendix B.

The eigenvalues μ_i of the monodromy matrix are called Floquet multipliers and provide information about the local orbital stability of the limit cycle Γ_0 [29]. For a periodic solution, at least one Floquet multiplier is always unity, lying on the unit circle in the complex plane. If there is only one multiplier equal to unity, the periodic solution is called a hyperbolic. A hyperbolic periodic solution is asymptotically orbitally stable if all Floquet multipliers other than the one at unity lie inside the unit circle [29]. It is called unstable if one or more Floquet multipliers are located outside the unit circle [29].

Figure 3-12 shows the Floquet multipliers associated with a periodic solution that emerges from a Hopf bifurcation of the March-Leuba system (as shown in Figure 3-9). As the bifurcation tool MatCont does not provide the angle of the Floquet multipliers, they are only depicted with their absolute values. One multiplier lies at unity, and the rest in a range between zero and one. This corresponds to a state for which all multipliers except the one equal to unity are inside the unit circle. Therefore it can be concluded that the analysed limit cycle is stable.

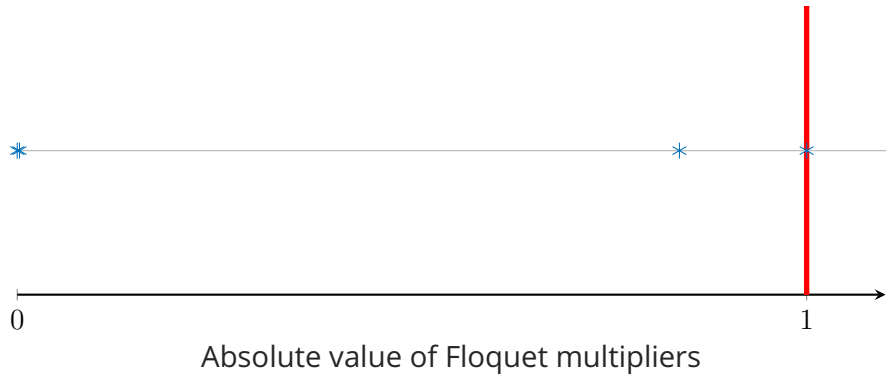

Figure 3-12: Floquet multipliers associated with the periodic solution that emerges from the Hopf bifurcation of the March-Leuba system depicted in Figure 3-9 ($k = -0.0037$).

3.5.2 Bifurcations of Periodic Solutions

Just as fixed-point solutions can undergo bifurcations when one or more control parameters are varied, periodic solutions can bifurcate as well. When changing a control parameter c_k gradually, a hyperbolic limit cycle may become nonhyperbolic at a critical parameter value $c_{k,\mathrm{c}}$. A bifurcation of the limit cycle occurs if the local phase portrait changes qualitatively after passing $c_{k,\mathrm{c}}$ such that it is not topologically equivalent [29]. There are different types of bifurcation for periodic solutions. They can be determined by analysing the behaviour of the Floquet multipliers during the parameter variation [29]. Figure 3-13 shows the motion of the Floquet multipliers in the complex plane for three bifurcation types: Fold, period-doubling and Neimark-Sacker bifurcation. The first two bifurcation types are considered in more detail in the following.

The limit cycle may be subjected to a fold bifurcation, in case a Floquet multiplier crosses the unit circle along the positive real axis [31]. For a cyclic fold bifurcation, a stable and an unstable periodic solution merge into each other as the varied control parameter approaches the critical value $c_{k,\mathrm{c}}$. Both cease to exist after this value has been passed [31]. That implies that two periodic solutions of opposite stability characteristics coexist until they eliminate each other at $c_{k,\mathrm{c}}$. Figure 3-14 depicts an example of two coexisting limit cycles, which conjoin as they undergo a fold bifurcation.

A bifurcation diagram tracking a periodic solution of the March-Leuba system is shown in Figure 3-15. The blue line represents the amplitude of the variable n for each value

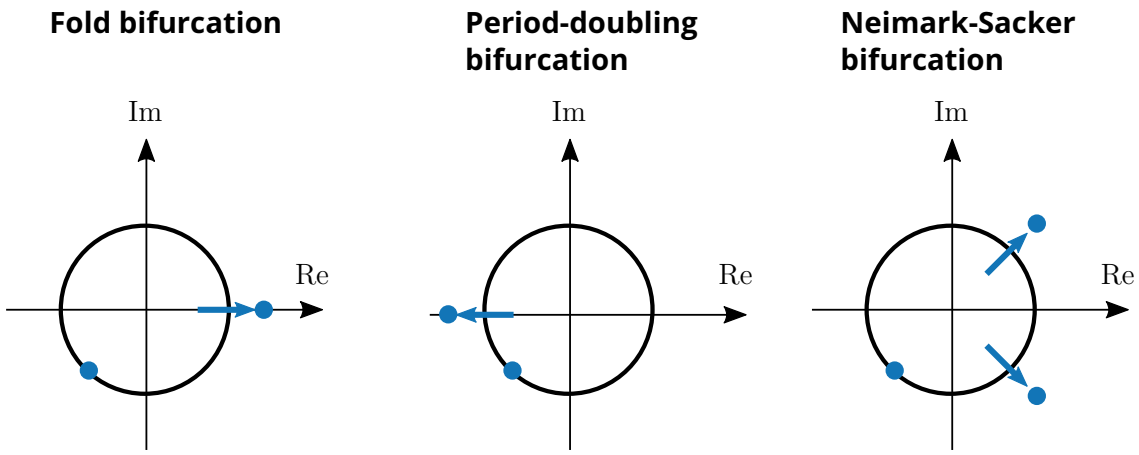

Figure 3-13: Motion of the Floquet multipliers in the complex plane for different bifurcation types of an initially stable limit cycle (adopted from [29], edited).

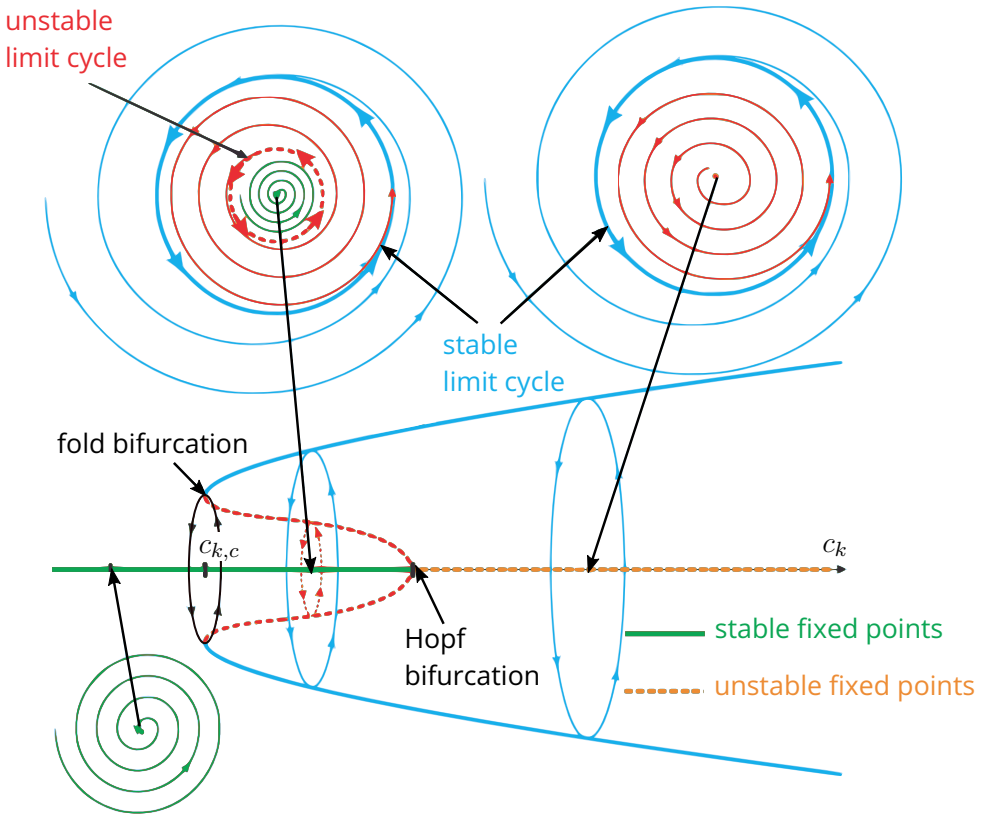

Figure 3-14: Bifurcation diagram for a generic fold bifurcation (adopted from [35], edited).

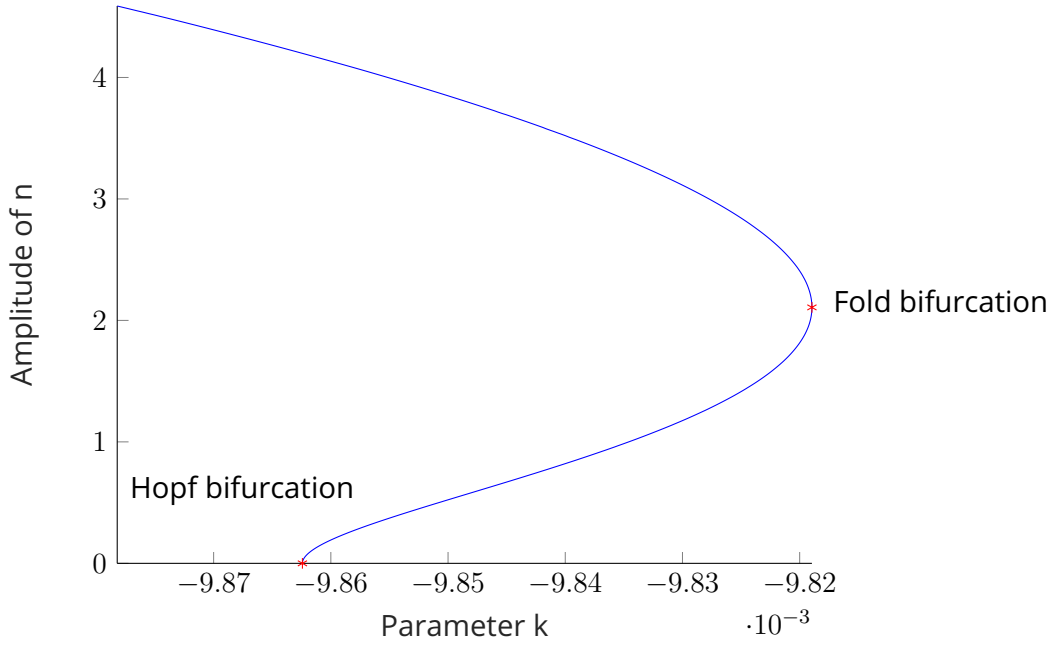

Figure 3-15: MatCont plot of a bifurcation diagram of the March-Leuba system (Appendix A) showing a fold bifurcation.

of the varied parameter k. The coexistence of two periodic solutions for $k = -9.863 \cdot 10^{-3} \ldots -9.82 \cdot 10^{-3}$ is clearly visible. The fold bifurcation occurs at the critical parameter value $k_\mathrm{c} = -9.82 \cdot 10^{-3}$, at which both periodic solutions merge into each other.

If for a stable periodic orbit, a Floquet multiplier leaves the unit circle along the negative real axis, the limit cycle undergoes a period-doubling bifurcation, also called a flip bifurcation [29]. For a supercritical period-doubling bifurcation, the initially stable limit cycle becomes unstable, and a new stable period-doubled solution appears when passing the critical parameter value. In the subcritical case, the original limit cycle also becomes unstable, and an unstable period-doubled cycle, which existed before the bifurcation, vanishes [29][31]. Figure 3-16 depicts these period-doubling phenomena using some generic phase portraits.

For illustration, Figure 3-17 shows the time series of the neutron concentration n for the March-Leuba system after a supercritical period-doubling bifurcation has occurred.

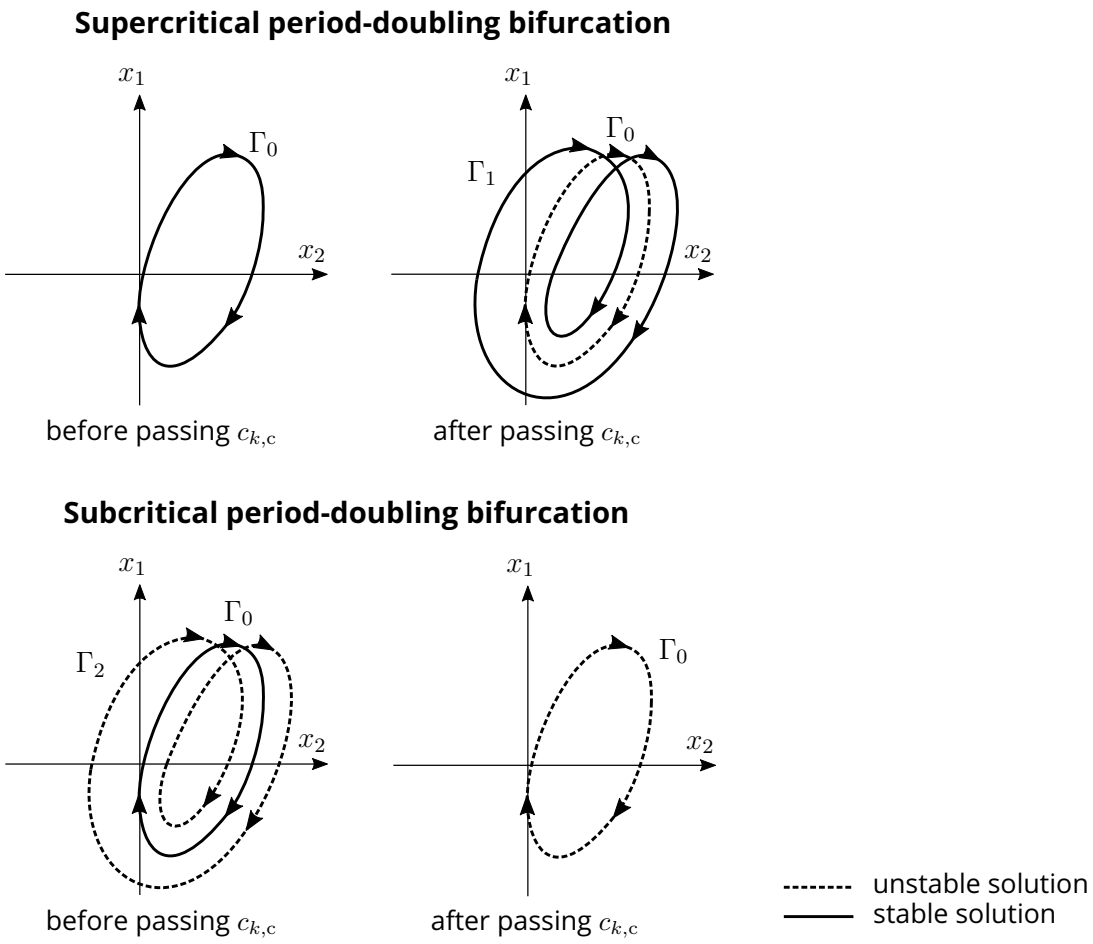

Figure 3-16: Phase portraits before and after a period-doubling bifurcation.

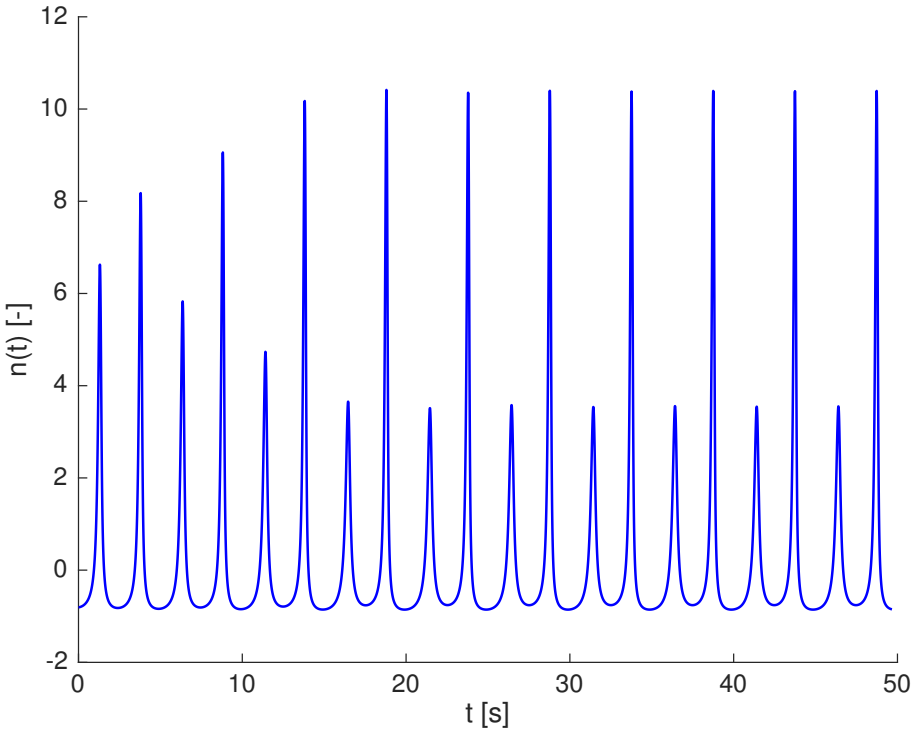

Figure 3-17: MatCont time series plot ($k = -0.006$) of variable n of the March-Leuba system after a supercritical period-doubling bifurcation.

4 ANALYSED REACTOR SYSTEM

4.1 Introduction

This chapter presents the MSFR reactor model, which is later used for the stability analyses. The governing differential equations are taken from a specified reference paper [7] and explained in detail in the following section. For a computational representation, these equations are translated into MATLAB. In order to verify the implementation, a set of plots is generated and compared with some reference graphs for the linearised system. Adaptations are made to correct some mismatched parameters.

The full specified nonlinear model is then presented as a set of delayed differential equations (DDEs). In the next step, these DDEs are rewritten as a system of ordinary differential equations (ODEs) in order to be later used for analysis in the numerical bifurcation tool MatCont. The MATLAB plots of the ODE system are compared to those of the original DDE system for verification.

4.2 Specified Reactor Model

This work analyses the stability of the MSFR design as presented in the article [7] by the Department of Energy of the Politecnico di Milano. The dynamical system and parameters are adopted from the mentioned paper and adjusted where necessary.

Considered state variables are the neutron population of the core $N(t)$, the delayed neutron precursor populations of the core $C_j(t)$ belonging to one of eight precursor groups and the salt temperatures $T_{\mathrm{c},i}(t)$ and $T_{\mathrm{he},i}(t)$ in the different axial regions of the core and heat exchanger, respectively. The given differential equations characterising these variables are provided below. Used symbols and corresponding parameter values can be found in Table 4-1.

The equations describing the neutron population $N(t)$ and delayed precursor populations $C_j(t)$ of the core are based on the point kinetics approach. For the neutron population in

Table 4-1: Reference parametric data for the MSFR model [7]

Parameter	Symbol	Unit	Value
Nominal thermal power	P_{nom}	$\mathrm{MW_{th}}$	3000
Mean neutron generation time	Λ	$\mu\mathrm{s}$	0.963
Total fraction of delayed neutron precursors	β	$-$	$318.06 \cdot 10^{-5}$
Fraction of delayed neutron precursors of group 1	β_1	$-$	$23.74 \cdot 10^{-5}$
Fraction of delayed neutron precursors of group 2	β_2	$-$	$47.25 \cdot 10^{-5}$
Fraction of delayed neutron precursors of group 3	β_3	$-$	$41.32 \cdot 10^{-5}$
Fraction of delayed neutron precursors of group 4	β_4	$-$	$63.94 \cdot 10^{-5}$
Fraction of delayed neutron precursors of group 5	β_5	$-$	$100.55 \cdot 10^{-5}$
Fraction of delayed neutron precursors of group 6	β_6	$-$	$15.22 \cdot 10^{-5}$
Fraction of delayed neutron precursors of group 7	β_7	$-$	$21.44 \cdot 10^{-5}$
Fraction of delayed neutron precursors of group 8	β_8	$-$	$4.60 \cdot 10^{-5}$
Decay constant of delayed neutron precursors of group 1	λ_1	$\mathrm{s^{-1}}$	$1.25 \cdot 10^{-2}$
Decay constant of delayed neutron precursors of group 2	λ_2	$\mathrm{s^{-1}}$	$2.83 \cdot 10^{-2}$
Decay constant of delayed neutron precursors of group 3	λ_3	$\mathrm{s^{-1}}$	$4.25 \cdot 10^{-2}$
Decay constant of delayed neutron precursors of group 4	λ_4	$\mathrm{s^{-1}}$	$1.33 \cdot 10^{-1}$
Decay constant of delayed neutron precursors of group 5	λ_5	$\mathrm{s^{-1}}$	$2.93 \cdot 10^{-1}$
Decay constant of delayed neutron precursors of group 6	λ_6	$\mathrm{s^{-1}}$	$6.67 \cdot 10^{-1}$
Decay constant of delayed neutron precursors of group 7	λ_7	$\mathrm{s^{-1}}$	1.64
Decay constant of delayed neutron precursors of group 8	λ_8	$\mathrm{s^{-1}}$	3.56
Core transit time	τ_{c}	s	1.95
External loop transit time	τ_{e}	s	1.95
Inverse of core transit time	λ_{c}	$\mathrm{s^{-1}}$	0.5128
Inverse of external loop transit time	λ_{e}	$\mathrm{s^{-1}}$	0.5128
Hot leg transit time	τ_1	s	0.6
Cold leg transit time	τ_2	s	0.6
Density feedback coefficient of the salt	α_{ex}	$\mathrm{K^{-1}}$	$-2.45 \cdot 10^{-5}$
Doppler constant	K_{D}	$-$	$-3161.39 \cdot 10^{-5}$
Reference average temperature of the salt	T^*_{c0}	K	973
Mass of salt in the core	M_{c}	kg	$37\,124$
Mass of salt in the heat exchangers	M_{he}	kg	$12\,993$
Specific heat capacity of the primary salt	c	$\mathrm{J\ kg^{-1}\ K^{-1}}$	1594
Salt flow rate in the primary circuit	W	$\mathrm{kg\ s^{-1}}$	$18\,964$
Overall heat transfer coefficient between the primary and intermediate salt	K	$\mathrm{W\ K^{-1}}$	$19.8 \cdot 10^6$

the core, the following expression applies:

$$\frac{\mathrm{d}N(t)}{\mathrm{d}t} = \frac{\rho_0 + \rho_\mathrm{t}(t) + \rho_\mathrm{ex}(t) - \beta}{\Lambda} N(t) + \sum_{j=1}^{8} \lambda_j C_j(t) \tag{4-1}$$

Eq. 4-1 contains three reactivity contributions: ρ_0, ρ_t and ρ_ex. The reactivity term ρ_0 ensures steady-state conditions. It results from the circulation of the delayed neutron precursors leaving and re-entering the core and is calculated as follows:

$$\rho_0 = \beta - \sum_{j=1}^{8} \frac{\beta_j \lambda_j}{\lambda_j + \lambda_c - \lambda_c \, \mathrm{e}^{-\tau_\mathrm{e} \lambda_j}} \tag{4-2}$$

For the given data of Table 4-1, one obtains $\rho_0 = 1.4 \cdot 10^{-3}$.

The reactivity feedback due to temperature changes in the molten salt ρ_t is assumed to result from the density variation and the Doppler effect [7]. The Doppler effect causes the resonance peak widths of the neutron capture cross-sections to vary with changing temperature due to the thermal motion of nuclei [36]. The temperature feedback contribution is modelled according to the expression

$$\rho_\mathrm{t}(t) = \alpha_\mathrm{ex} \left(T_\mathrm{c}^*(t) - T_\mathrm{c0}^* \right) + K_\mathrm{D} \ln \left(\frac{T_\mathrm{c}^*(t)}{T_\mathrm{c0}^*} \right) \tag{4-3}$$

with the time-dependent average salt temperature $T_\mathrm{c}^*(t)$ and the static reference temperature T_c0^*.

The third reactivity term ρ_ex represents the externally supplied reactivity by means of control rod motion and adjustment of the salt composition.

The adapted point kinetics equation for the number of delayed precursors of each group j takes the circulating nature of the carrier fluid into account and is given as

$$\frac{\mathrm{d}C_j(t)}{\mathrm{d}t} = \frac{\beta_j}{\Lambda} N(t) - (\lambda_j + \lambda_\mathrm{c}) C_j(t) + \lambda_\mathrm{c} C_j(t - \tau_\mathrm{e}) \mathrm{e}^{-\tau_\mathrm{e} \lambda_j} \ . \tag{4-4}$$

The article [7] describing the reference design assumes a proportionality between the neutron population of the core $N(t)$ and the generated thermal reactor power $P(t)$. This relation is described by the ratio $\frac{P(t)}{P_0} = \frac{N(t)}{N_0}$. The constants P_0 and N_0 are the steady-state

values for the reactor power and neutron population in the core. Hence, Eq. 4-1 can be expressed in terms of reactor power:

$$\frac{\mathrm{d}P(t)\frac{N_0}{P_0}}{\mathrm{d}t} = \frac{\rho_0 + \rho_\mathrm{t}(t) + \rho_\mathrm{ex}(t) - \beta}{\Lambda} P(t)\frac{N_0}{P_0} + \sum_{j=1}^{8} \lambda_j C_j(t) \qquad | \cdot \frac{P_0}{N_0} \tag{4-5}$$

$$\frac{\mathrm{d}P(t)}{\mathrm{d}t} = \frac{\rho_0 + \rho_\mathrm{t}(t) + \rho_\mathrm{ex}(t) - \beta}{\Lambda} P(t) + \sum_{j=1}^{8} \lambda_j \widetilde{C}_j(t) \tag{4-6}$$

where $\widetilde{C}_j(t) = C_j(t)\frac{P_0}{N_0}$ is the rescaled delayed neutron precursor population of group j. Accordingly, the rescaled version of Eq. 4-4 is obtained as follows:

$$\frac{\mathrm{d}C_j(t)}{\mathrm{d}t} = \frac{\beta_j}{\Lambda} P(t)\frac{N_0}{P_0} - (\lambda_j + \lambda_\mathrm{c})C_j(t) + \lambda_\mathrm{c} C_j(t - \tau_\mathrm{e})\mathrm{e}^{-\tau_\mathrm{e}\lambda_j} \qquad | \cdot \frac{P_0}{N_0} \tag{4-7}$$

$$\frac{\mathrm{d}\widetilde{C}_j(t)}{\mathrm{d}t} = \frac{\beta_j}{\Lambda} P(t) - (\lambda_j + \lambda_\mathrm{c})\widetilde{C}_j(t) + \lambda_\mathrm{c} \widetilde{C}_j(t - \tau_\mathrm{e})\mathrm{e}^{-\tau_\mathrm{e}\lambda_j} \ . \tag{4-8}$$

The differential equations for the salt temperatures in the core $T_{\mathrm{c},i}(t)$ and heat exchangers $T_{\mathrm{he},i}(t)$ originate from a one-dimensional description of the energy balance in these components. A discretisation of this energy conservation equation following the upwind differencing scheme leads to a nodalised reactor model, which can be seen in Figure 4-1.

The MSFR design employs sixteen identical heat exchangers, which pass the heat from the primary salt on to an intermediate salt (see Section 2.7). In the specified model, all heat exchangers are condensed into one in order to reduce the model complexity. The temperatures in the different regions of the core and heat exchanger are described by the following equations:

$$\frac{\mathrm{d}T_{\mathrm{c},i}(t)}{\mathrm{d}t} = \frac{f_i}{M_{\mathrm{c},i}\, c} P(t) + \frac{W}{M_{\mathrm{c},i}} \Big(T_{\mathrm{c},i-1}(t) - T_{\mathrm{c},i}(t) \Big) \qquad \text{for } i = 1, \ldots, N_\mathrm{c} \tag{4-9}$$

$$\frac{\mathrm{d}T_{\mathrm{he},i}(t)}{\mathrm{d}t} = \frac{W}{M_{\mathrm{he},i}} \Big(T_{\mathrm{he},i-1}(t) - T_{\mathrm{he},i}(t) \Big) + \frac{K_i}{M_{\mathrm{he},i}\, c} \Big(T_\mathrm{ic} - T_{\mathrm{he},i}(t) \Big) \qquad \text{for } i = 1, \ldots, N_\mathrm{he} \tag{4-10}$$

with N_c being the number of nodes in the core and N_he the number of nodes in the heat exchanger. The temperature T_ic is the one of the intermediate salt on the secondary side of the heat exchanger and modelled to be uniform. The value of T_ic depends on the initial

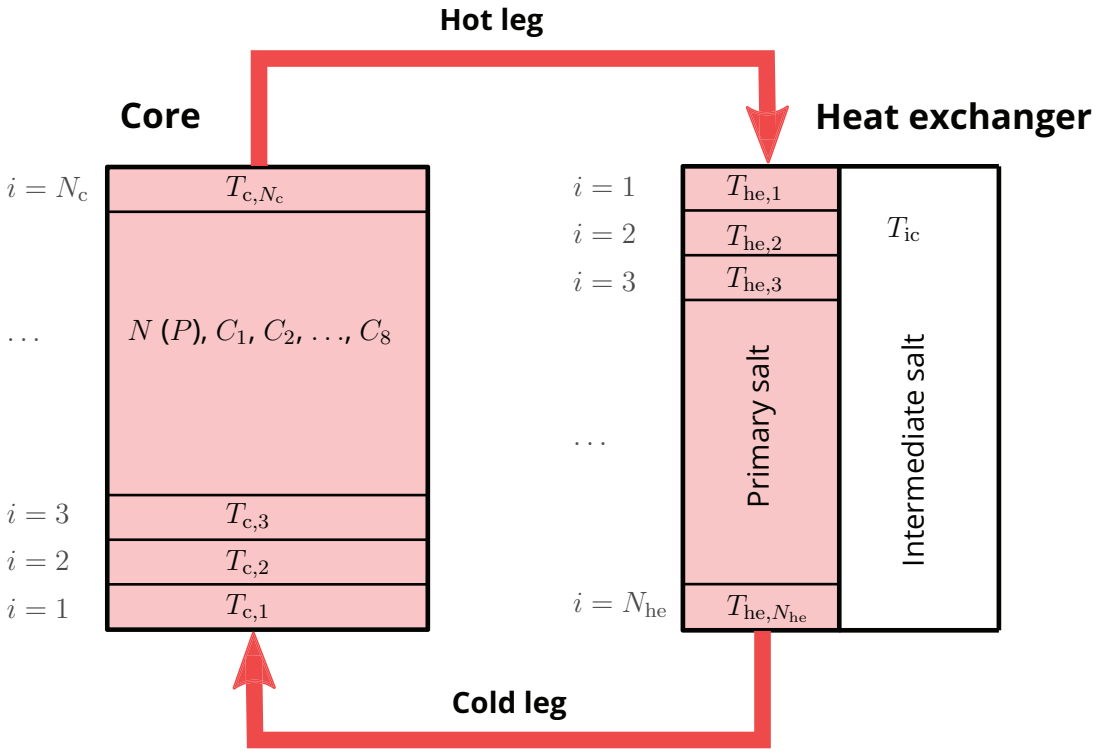

Figure 4-1: Discretised MSFR model and state variables (adopted from [7], edited).

conditions and can be calculated by solving the presented system of equations for steady-state conditions.

The power contribution in each axial region i of the core is weighted with a factor f_i. This factor is calculated according to a cosine function that approximates the axial neutron flux distribution. Figure 4-2 shows a sketch of the considered cosine distribution.

The weighting factors are computed according to the following equation where x_i^- and x_i^+ are associated with the lower and upper boundary of a core region i, respectively:

$$f_i = \frac{\int_{x_i^-}^{x_i^+} \cos x}{\int_{-\frac{\pi}{2}}^{\frac{\pi}{2}} \cos x}\,\mathrm{d}x \tag{4-11}$$

$$\text{with } x_i^- = -\frac{\pi}{2} + \frac{\pi}{N_c} \cdot (i-1)$$

$$\text{and } x_i^+ = -\frac{\pi}{2} + \frac{\pi}{N_c} \cdot i$$

$$\text{for } i = 1, \ldots, N_c\ .$$

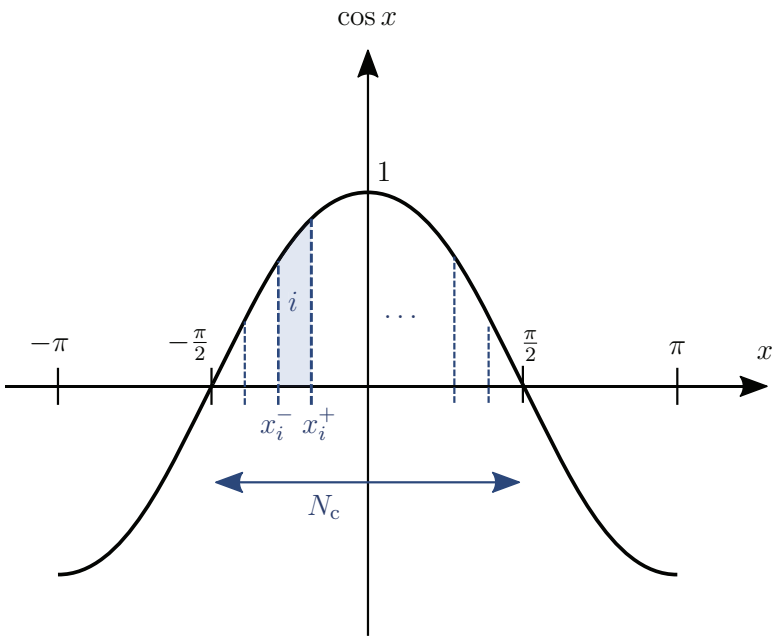

Figure 4-2: Cosine distribution.

The symbols $M_{\mathrm{c},i}$, $M_{\mathrm{he},i}$ and K_i in Eqs. 4-9 and 4-10 represent the masses of the salt and the overall heat transfer coefficient in reference to the respective region i of the core or heat exchanger. They are calculated as $M_{\mathrm{c},i} = \frac{M_{\mathrm{c}}}{N_{\mathrm{c}}}$, $M_{\mathrm{he},i} = \frac{M_{\mathrm{he}}}{N_{\mathrm{he}}}$ and $K_i = \frac{K}{N_{\mathrm{he}}}$.

In case $i = 1$, Eqs. 4-9 and 4-10 are adapted in the following way:

$$\frac{\mathrm{d}T_{\mathrm{c},1}(t)}{\mathrm{d}t} = \frac{f_1}{M_{\mathrm{c},1}\,c}P(t) + \frac{W}{M_{\mathrm{c},1}}\Big(T_{\mathrm{he},N_{\mathrm{he}}}(t-\tau_2) - T_{\mathrm{c},1}(t)\Big) \tag{4-12}$$

$$\frac{\mathrm{d}T_{\mathrm{he},1}(t)}{\mathrm{d}t} = \frac{W}{M_{\mathrm{he},1}}\Big(T_{\mathrm{c},N_{\mathrm{c}}}(t-\tau_1) - T_{\mathrm{he},1}(t)\Big) + \frac{K_1}{M_{\mathrm{he},1}\,c}\Big(T_{\mathrm{ic}} - T_{\mathrm{he},1}(t)\Big) \tag{4-13}$$

where the salt temperature at the core inlet corresponds to the temperature of the last heat exchanger region $T_{\mathrm{he},N_{\mathrm{he}}}$ at time $t - \tau_2$. Accordingly, the inlet temperature of the heat exchanger relates to the temperature of the last core region $T_{\mathrm{c},N_{\mathrm{c}}}$ at time $t - \tau_1$.

Unless specified otherwise, all diagrams of this chapter are calculated assuming a reactivity insertion of $\rho_{\mathrm{ex}}(t_0 = 0) = 1 \cdot 10^{-5}$. In terms of discretisation, $N_{\mathrm{c}} = N_{\mathrm{he}} = 10$ regions in the core and heat exchanger each are considered. These input values are adopted from the reference paper. With the given discretisation data, the following values for the cosine

distribution are obtained:

$$f = \begin{pmatrix} 0.0245 & 0.0710 & 0.1106 & 0.1394 & 0.1545 & 0.1545 & 0.1394 & 0.1106 & 0.0710 & 0.0245 \end{pmatrix}^\top$$

4.3 Implementation and Verification of the Linearised System of Equations

4.3.1 Linearised System of Delayed Differential Equations

The presented model contains nonlinearities in Eq. 4-1 or, more specifically, Eq. 4-6. This refers to the expressions $\rho_\mathrm{t}(t)P(t)$ and $\rho_\mathrm{ex}(t)P(t)$, in which both multiplication factors are time-dependent. Furthermore, the equation for the reactivity contribution $\rho_\mathrm{t}(t)$ itself (see Eq. 4-3) contains the nonlinear logarithmic term $\ln\left(T_\mathrm{c}^*(t)/T_\mathrm{c0}^*\right)$.

In the reference article [7] by the Politecnico di Milano, a linearised version of the model described in the previous section is used for the dynamics and stability analysis. A linearisation of the relevant equations around the fixed point

$$\boldsymbol{X}_0 = \begin{pmatrix} P_0 & \widetilde{C}_{1,0} & \dots & \widetilde{C}_{8,0} & T_{\mathrm{c},1,0} & \dots & T_{\mathrm{c},N_\mathrm{c},0} & T_{\mathrm{he},1,0} & \dots & T_{\mathrm{he},N_\mathrm{he},0} \end{pmatrix}^\top$$

is carried out according to Eqs. 3-8 and 3-9.

This yields the following linearised system of equations:

$$\frac{\mathrm{d}\delta P(t)}{\mathrm{d}t} = \frac{\rho_0 - \beta}{\Lambda}\delta P(t) + \sum_{j=1}^{8}\lambda_j \delta\widetilde{C}_j(t) + \frac{P_0}{\Lambda}\delta\rho_\mathrm{ex}(t) + \alpha_\mathrm{ex}\frac{P_0}{\Lambda}\delta T_c^*(t) + \frac{K_\mathrm{D}P_0}{\Lambda T_\mathrm{c0}^*}\delta T_c^*(t) \tag{4-14}$$

$$\text{with } \delta T_c^*(t) = \frac{1}{N_\mathrm{c}}\sum_{i=1}^{N_\mathrm{c}}\delta T_{c,i}(t)$$

$$\frac{\mathrm{d}\delta\widetilde{C}_j(t)}{\mathrm{d}t} = \frac{\beta_j}{\Lambda}\delta P(t) - (\lambda_j + \lambda_\mathrm{c})\delta\widetilde{C}_j(t) + \lambda_\mathrm{c}\delta\widetilde{C}_j(t-\tau_\mathrm{e})\mathrm{e}^{-\tau_\mathrm{e}\lambda_j} \tag{4-15}$$

$$\text{for } j = 1\dots 8$$

$$\frac{\mathrm{d}\delta T_{\mathrm{c},1}(t)}{\mathrm{d}t} = \frac{f_1}{M_{\mathrm{c},1}\,c}\delta P(t) + \frac{W}{M_{\mathrm{c},1}}\Big(\delta T_{\mathrm{he},N_\mathrm{he}}(t-\tau_2) - \delta T_{\mathrm{c},1}(t)\Big) \tag{4-16}$$

$$\frac{\mathrm{d}\delta T_{\mathrm{c},i}(t)}{\mathrm{d}t} = \frac{f_i}{M_{\mathrm{c},i}\,c}\delta P(t) + \frac{W}{M_{\mathrm{c},i}}\Big(\delta T_{\mathrm{c},i-1}(t) - \delta T_{\mathrm{c},i}(t)\Big) \tag{4-17}$$

for $i = 2, \ldots, N_{\mathrm{c}}$

$$\frac{\mathrm{d}\delta T_{\mathrm{he},1}(t)}{\mathrm{d}t} = \frac{W}{M_{\mathrm{he},1}}\Big(\delta T_{\mathrm{c},N_{\mathrm{c}}}(t-\tau_1) - \delta T_{\mathrm{he},1}(t)\Big) - \frac{K_1}{M_{\mathrm{he},1}\,c}\delta T_{\mathrm{he},1}(t) \tag{4-18}$$

$$\frac{\mathrm{d}\delta T_{\mathrm{he},i}(t)}{\mathrm{d}t} = \frac{W}{M_{\mathrm{he},i}}\Big(\delta T_{\mathrm{he},i-1}(t) - \delta T_{\mathrm{he},i}(t)\Big) - \frac{K_i}{M_{\mathrm{he},i}\,c}\delta T_{\mathrm{he},i}(t) \tag{4-19}$$

for $i = 2, \ldots, N_{\mathrm{he}}$.

4.3.2 Comparison with Reference Plots

The linearised system of Eqs. 4-14 to 4-19 is implemented in MATLAB. There are time delays in Eqs. 4-15 ($t - \tau_{\mathrm{e}}$), 4-16 ($t - \tau_1$) and 4-18 ($t - \tau_2$). Hence, the equations are coded as a system of delayed differential equations (DDEs). The DDE system is integrated time-wise, and the resulting reactor power $\delta P(t)$ is plotted over a reference graph from the framework paper. Both graphs are compared to each other in order to verify the used model and MATLAB implementation. The MATLAB code is saved on the accompanying CD. A list of all files used in this work can be found in Appendix F.

Figure 4-3 shows the time series plot of $\delta P(t)$ at three different power levels P_0 for a reactivity insertion of $\rho_{\mathrm{ex}} = 10^{-5}$. The reference graph is displayed in the background. It is noticeable that both sets are similar, but there is a deviation between the newly plotted curves and the ones from the reference diagram for $t > 1\,\mathrm{s}$.

The reference paper also provides a Bode plot of the linearised MSFR system. For additional verification, the Bode plot is created for the MATLAB implemented system of this work and compared to the reference one. Three different methods are applied for this purpose:

1. using a state-space model of the linearised system,
2. using the Laplace transform of the linearised system,
3. using a Simulink model of the linearised system.

Appendix F lists the associated MATLAB files. The resulting Bode plots of those three ap-

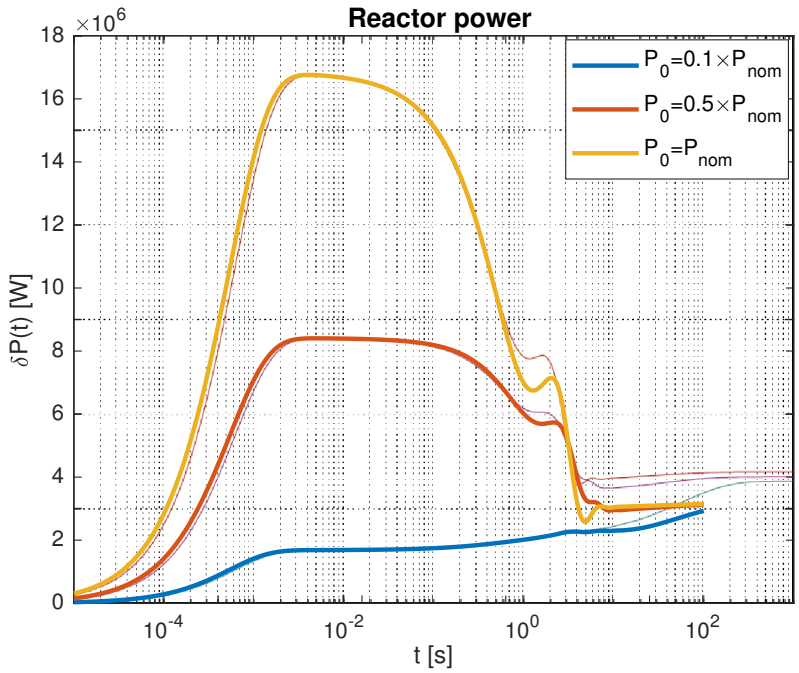

Figure 4-3: Reactor power plot of the linearised DDE system (Eqs. 4-14 to 4-19) at different power levels in comparison with the reference [7], considering a reactivity insertion of $\rho_{\text{ex}} = 10^{-5}$ and the given parameter set of Table 4-1.

proaches are compared with each other, and it is found that they all yield the same curves.

Figure 4-4 shows the closed-loop Bode plots of the linearised DDE system (Eqs. 4-14 to 4-19) using the parameter set of Table 4-1. The plots obtained in the reference paper are depicted in the background. The different-coloured graphs of Figure 4-4 represent the Bode plots for different power levels P_0.

In the magnitude plot as well as the phase plot, there is a deviation between the calculated graphs and the graphs given by the reference [7]. Since all three implementation methods create the same Bode plots in MATLAB, a coding error can be eliminated from being responsible. As a next step, the possibility of an incorrect parameter set is investigated. The difference between both sets of curves seems to be increasing with the power level P_0 in the range $\omega = 10^{-4} \ldots 1 \, \frac{\text{rad}}{\text{s}}$. Hence, one can assume that some parameters in the core temperature equation 4-17, which depends on the reactor power, might be responsible.

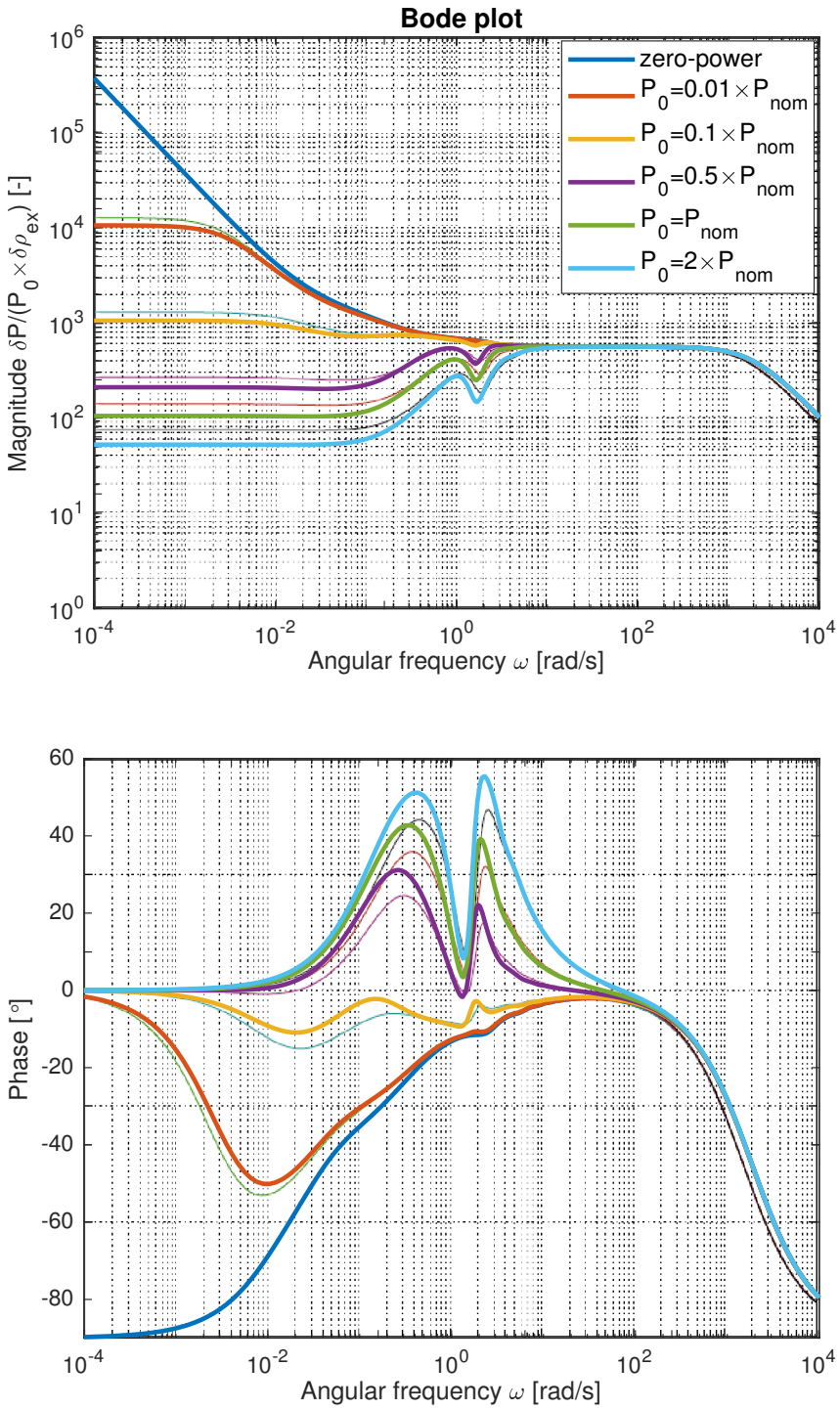

Figure 4-4: Closed-loop Bode plots of the linearised DDE system (Eqs. 4-14 to 4-19) at different power levels in comparison with the reference [7] for the given parameter set of Table 4-1.

4.3.3 Adaptation of Parameter Values

Checking the parameter data of Table 4-1, provided by the reference article, reveals discrepancies for the salt flow rate W and the salt masses in the core M_c and heat exchanger M_{he}:

$$\underbrace{W}_{18\,964\,\frac{\mathrm{kg}}{\mathrm{s}}} \neq \underbrace{\frac{M_c}{\tau_{\mathrm{c}}}}_{19\,038\,\frac{\mathrm{kg}}{\mathrm{s}}} \neq \underbrace{\frac{M_{\mathrm{he}}}{\tau_{\mathrm{e}} - \tau_1 - \tau_2}}_{17\,324\,\frac{\mathrm{kg}}{\mathrm{s}}} . \tag{4-20}$$

It is also found that some fuel salt data provided in the reference article do not match those from the quoted source [37]. Table 4-2 specifies these parameters.

As a consequence, the values for M_{c} and M_{he} are changed so that they fulfil Eq. 4-20 for $W = 18\,964\,\frac{\mathrm{kg}}{\mathrm{s}}$. Regarding the parameters of Table 4-2, the values are adopted from the original source [37] under the assumption of fresh fuel salt.

Table 4-3 contains the updated parameter list for the MSFR model. Using the new parameter set, the time series and Bode plots of the linearised DDE system are calculated again and compared to the diagrams of the reference paper [7]. Figures 4-5 and 4-6 show the updated plots.

The new plots show little difference compared to those using the erroneous parameter set (Figures 4-3 and 4-4). However, the 'zero-power' Bode plot, which disregards the temperature feedback, matches fully with the curve from the reference paper. This is due to changing the value of Λ. The remaining deviations for the other power levels must be originating from another mismatching parameter that is used for calculating the salt temperatures in the core or heat exchangers.

Table 4-2: Parameters with mismatching values comparing data from [7] and [37]

Parameter	Symbol	Value according to reference paper [7]	Value according to source paper [37]
Mean neutron generation time	Λ	$0.963\,\mu\mathrm{s}$	$1.12\,\mu\mathrm{s}$
Density feedback coefficient	α_{ex}	$-2.45 \cdot 10^{-5}\,\mathrm{K}^{-1}$	$-2.53 \cdot 10^{-5}\,\mathrm{K}^{-1}$
Doppler constant	K_{D}	$-3161.39 \cdot 10^{-5}$	$-4046 \cdot 10^{-5}$

Table 4-3: Updated parametric data for the MSFR model, changes in red

Parameter	Symbol	Unit	Value
Nominal thermal power	P_{nom}	$\mathrm{MW_{th}}$	3000
Mean neutron generation time	Λ	µs	1.12
Total fraction of delayed neutron precursors	β	–	$318.06 \cdot 10^{-5}$
Fraction of delayed neutron precursors of group 1	β_1	–	$23.74 \cdot 10^{-5}$
Fraction of delayed neutron precursors of group 2	β_2	–	$47.25 \cdot 10^{-5}$
Fraction of delayed neutron precursors of group 3	β_3	–	$41.32 \cdot 10^{-5}$
Fraction of delayed neutron precursors of group 4	β_4	–	$63.94 \cdot 10^{-5}$
Fraction of delayed neutron precursors of group 5	β_5	–	$100.55 \cdot 10^{-5}$
Fraction of delayed neutron precursors of group 6	β_6	–	$15.22 \cdot 10^{-5}$
Fraction of delayed neutron precursors of group 7	β_7	–	$21.44 \cdot 10^{-5}$
Fraction of delayed neutron precursors of group 8	β_8	–	$4.60 \cdot 10^{-5}$
Decay constant of delayed neutron precursors of group 1	λ_1	$\mathrm{s^{-1}}$	$1.25 \cdot 10^{-2}$
Decay constant of delayed neutron precursors of group 2	λ_2	$\mathrm{s^{-1}}$	$2.83 \cdot 10^{-2}$
Decay constant of delayed neutron precursors of group 3	λ_3	$\mathrm{s^{-1}}$	$4.25 \cdot 10^{-2}$
Decay constant of delayed neutron precursors of group 4	λ_4	$\mathrm{s^{-1}}$	$1.33 \cdot 10^{-1}$
Decay constant of delayed neutron precursors of group 5	λ_5	$\mathrm{s^{-1}}$	$2.93 \cdot 10^{-1}$
Decay constant of delayed neutron precursors of group 6	λ_6	$\mathrm{s^{-1}}$	$6.67 \cdot 10^{-1}$
Decay constant of delayed neutron precursors of group 7	λ_7	$\mathrm{s^{-1}}$	1.64
Decay constant of delayed neutron precursors of group 8	λ_8	$\mathrm{s^{-1}}$	3.56
Core transit time	τ_{c}	s	1.95
External loop transit time	τ_{e}	s	1.95
Inverse of core transit time	λ_{c}	$\mathrm{s^{-1}}$	0.5128
Inverse of external loop transit time	λ_{e}	$\mathrm{s^{-1}}$	0.5128
Hot leg transit time	τ_1	s	0.6
Cold leg transit time	τ_2	s	0.6
Density feedback coefficient of the salt	α_{ex}	$\mathrm{K^{-1}}$	$-2.53 \cdot 10^{-5}$
Doppler constant	K_{D}	–	$-4046 \cdot 10^{-5}$
Reference average temperature of the salt	T^*_{c0}	K	973
Mass of salt in the core	M_{c}	kg	36 980
Mass of salt in the heat exchangers	M_{he}	kg	14 223
Specific heat of the primary salt	c	$\mathrm{J\ kg^{-1}\ K^{-1}}$	1594
Salt flow rate in the primary circuit	W	$\mathrm{kg\ s^{-1}}$	18 964
Overall heat transfer coefficient between the primary and intermediate salt	K	$\mathrm{W\ K^{-1}}$	$19.8 \cdot 10^6$

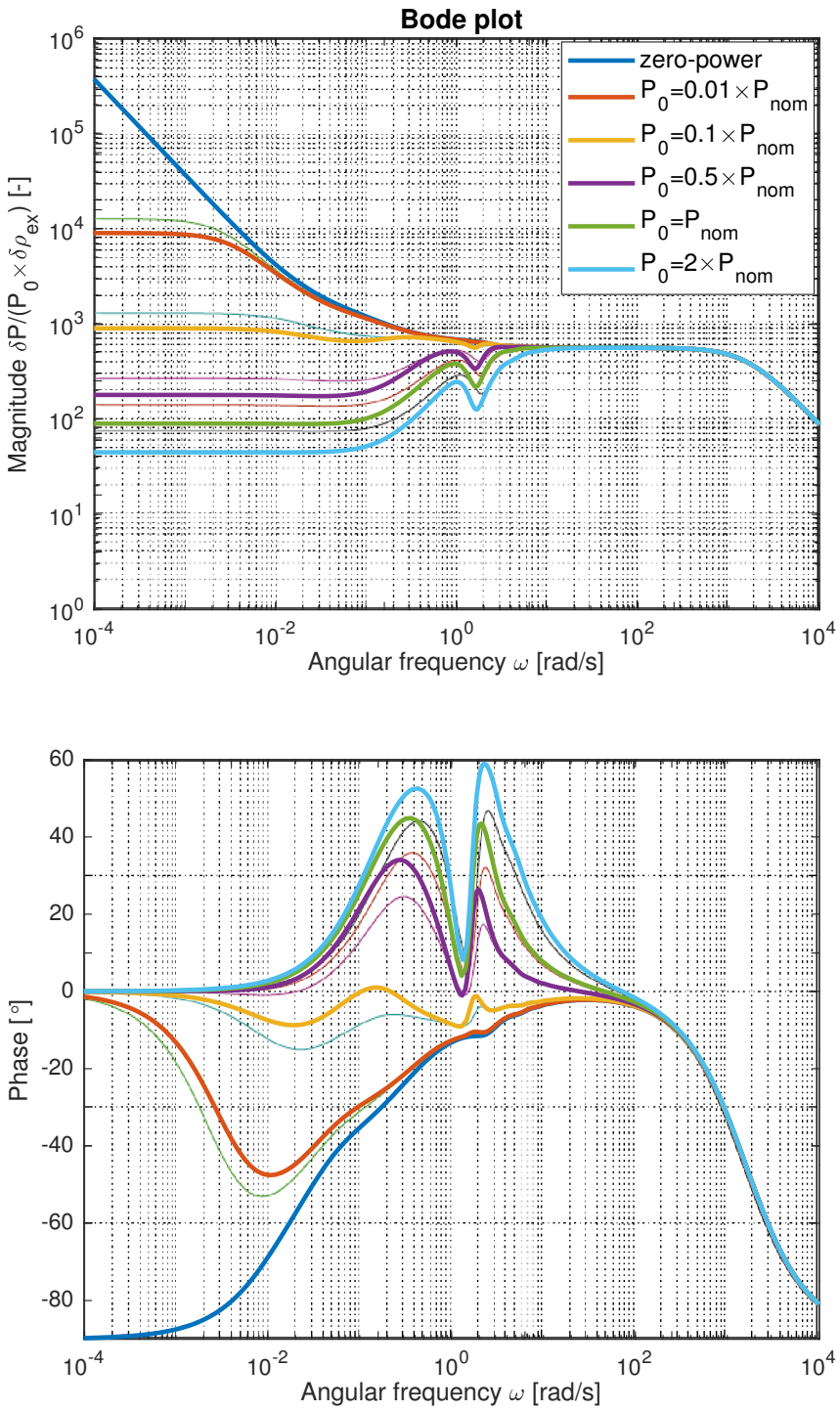

Figure 4-5: Updated closed-loop Bode plots of the linearised DDE system (Eqs. 4-14 to 4-19) in comparison with the reference [7] for the corrected parameter set of Table 4-3.

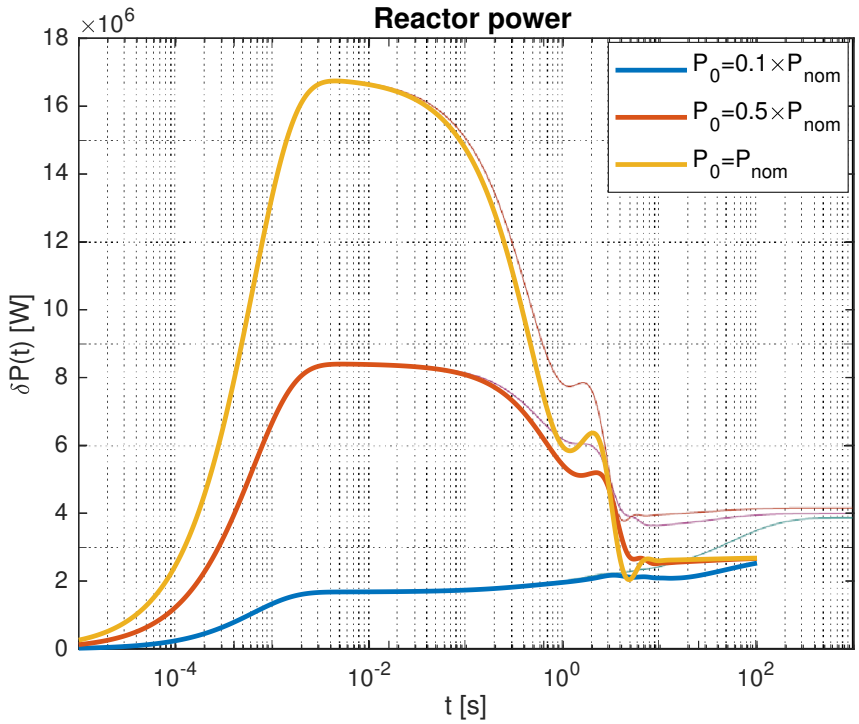

Figure 4-6: Updated reactor power plot of the linearised DDE system (Eqs. 4-14 to 4-19) in comparison with the reference [7] for the corrected parameter set of Table 4-3.

The responsible parameter might be the overall heat transfer coefficient K of the heat exchanger. However, it is not possible to confirm this assumption since the relevant source for this parameter cannot be determined from the reference paper. The specific value for K is not of great importance since this parameter is going to get varied for bifurcation analysis in any case. Therefore K is left unchanged, and no further parameter adaptations are undertaken.

4.4 Implementation and Verification of the Nonlinear System of Equations

4.4.1 Nonlinear System of Delayed Differential Equations

In the next step, the full, nonlinearised system of equations describing the MSFR model is implemented as MATLAB code. The relevant equations are explained in detail in Section 4.2 and listed hereafter once more in a compact form:

$$\frac{\mathrm{d}P(t)}{\mathrm{d}t} = \frac{\rho_0 + \rho_\mathrm{t}(t) + \rho_\mathrm{ex}(t) - \beta}{\Lambda} P(t) + \sum_{j=1}^{8} \lambda_j \widetilde{C}_j(t) \tag{4-21}$$

$$\text{with } \rho_{\mathrm{t}}(t) = \alpha_{\mathrm{ex}}\Big(T_{\mathrm{c}}^{*}(t) - T_{\mathrm{c0}}^{*}\Big) + K_{\mathrm{D}} \ln\left(\frac{T_{\mathrm{c}}^{*}(t)}{T_{\mathrm{c0}}^{*}}\right)$$

$$\text{and } T_{c}^{*}(t) = \frac{1}{N_{\mathrm{c}}} \sum_{i=1}^{N_{\mathrm{c}}} T_{c,i}(t)$$

$$\frac{\mathrm{d}\widetilde{C}_j(t)}{\mathrm{d}t} = \frac{\beta_j}{\Lambda} P(t) - (\lambda_j + \lambda_{\mathrm{c}})\widetilde{C}_j(t) + \lambda_{\mathrm{c}}\widetilde{C}_j(t - \tau_{\mathrm{e}})\mathrm{e}^{-\tau_{\mathrm{e}}\lambda_j} \tag{4-22}$$

$$\text{for } j = 1 \ldots 8$$

$$\frac{\mathrm{d}T_{\mathrm{c},1}(t)}{\mathrm{d}t} = \frac{f_1}{M_{\mathrm{c},1}\, c} P(t) + \frac{W}{M_{\mathrm{c},1}}\Big(T_{\mathrm{he},N_{\mathrm{he}}}(t - \tau_2) - T_{\mathrm{c},1}(t)\Big) \tag{4-23}$$

$$\frac{\mathrm{d}T_{\mathrm{c},i}(t)}{\mathrm{d}t} = \frac{f_i}{M_{\mathrm{c},i}\, c} P(t) + \frac{W}{M_{\mathrm{c},i}}\Big(T_{\mathrm{c},i-1}(t) - T_{\mathrm{c},i}(t)\Big) \tag{4-24}$$

$$\text{for } i = 2, \ldots, N_{\mathrm{c}}$$

$$\frac{\mathrm{d}T_{\mathrm{he},1}(t)}{\mathrm{d}t} = \frac{W}{M_{\mathrm{he},1}}\Big(T_{\mathrm{c},N_{\mathrm{c}}}(t - \tau_1) - T_{\mathrm{he},1}(t)\Big) + \frac{K_1}{M_{\mathrm{he},1}\, c}\Big(T_{\mathrm{ic}} - T_{\mathrm{he},1}(t)\Big) \tag{4-25}$$

$$\frac{\mathrm{d}T_{\mathrm{he},i}(t)}{\mathrm{d}t} = \frac{W}{M_{\mathrm{he},i}}\Big(T_{\mathrm{he},i-1}(t) - T_{\mathrm{he},i}(t)\Big) + \frac{K_i}{M_{\mathrm{he},i}\, c}\Big(T_{\mathrm{ic}} - T_{\mathrm{he},i}(t)\Big) \tag{4-26}$$

$$\text{for } i = 2, \ldots, N_{\mathrm{he}}.$$

Just as in the linearised version, there are time delays incorporated in Eqs. 4-22 ($t - \tau_{\mathrm{e}}$), 4-23 ($t - \tau_1$) and 4-25 ($t - \tau_2$). Consequently, the system of Eqs. 4-21 to 4-26 is coded as a DDE system in MATLAB and integrated time-wise. Appendix F provides the corresponding MATLAB filename.

Figure 4-7 shows the MATLAB plot of the reactor power $P(t)$ of the nonlinear DDE system relative to the steady-state power level P_0, considering a reactivity insertion of $\rho_{\mathrm{ex}} = 10^{-5}$ and the corrected parameter set of Table 4-3. Three different curves for three different operational power levels P_0 are plotted. It is important to note that each of those curves belongs to an individual dynamical system with a different operating point. Specifying the steady-state value P_0 leads to different temperatures of the intermediate salt T_{ic}, which are calculated by solving the above equation system at the steady state. Each operating point has its distinctive value of T_{ic}.

The numerical bifurcation tool MatCont [38], which operates on MATLAB, shall be used for

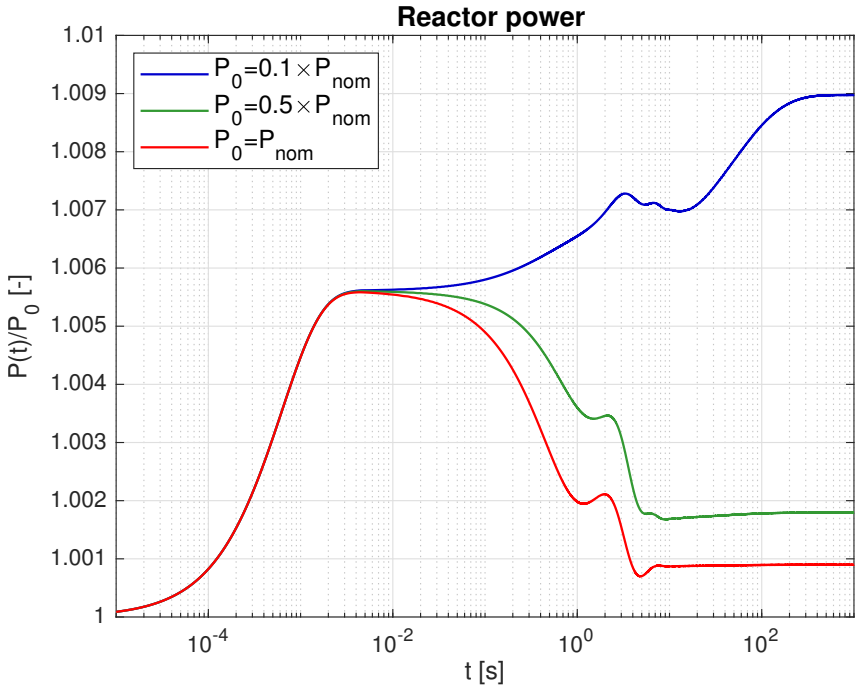

Figure 4-7: Reactor power plot of the nonlinear DDE system (Eqs. 4-21 to 4-26) at different power levels, considering a reactivity insertion of $\rho_{\mathrm{ex}} = 10^{-5}$ and the parameter set of Table 4-3.

the bifurcation analysis of the nonlinear MSFR model. Since MatCont requires the input equations to be ODEs, the nonlinear DDE system (Eqs. 4-21 to 4-26) has to be rewritten as an ODE system. Therefore, the variables containing time delays $\widetilde{C}_j(t-\tau_{\mathrm{e}})$, $T_{\mathrm{c},N_{\mathrm{c}}}(t-\tau_1)$ and $T_{\mathrm{he},N_{\mathrm{he}}}(t-\tau_2)$ must be replaced by new variables that are defined by additional ODEs.

4.4.2 Delayed Neutron Precursor Equation Adjustments

Regarding the delayed neutron precursor population of a group j inside the core, the describing delayed differential equation is made up of the following parts:

$$\underbrace{\frac{\mathrm{d}\widetilde{C}_j(t)}{\mathrm{d}t}}_{\substack{\text{change of precursor}\\ \text{population with time}}} = \underbrace{\frac{\beta_j}{\Lambda}P(t)}_{\substack{\text{precursors generated}\\ \text{from fission reaction}}} - \underbrace{\lambda_j\widetilde{C}_j(t)}_{\text{decaying precursors}} - \underbrace{\lambda_{\mathrm{c}}\widetilde{C}_j(t)}_{\substack{\text{precursors flowing}\\ \text{out of the core}}} + \underbrace{\lambda_{\mathrm{c}}\widetilde{C}_j(t-\tau_{\mathrm{e}})\mathrm{e}^{-\tau_{\mathrm{e}}\lambda_j}}_{\substack{\text{precursors flowing}\\ \text{into the core}}} . \tag{4-27}$$

The part that represents the precursors flowing into the core is specified as

$$\underbrace{\lambda_{\mathrm{c}}}_{\substack{\text{inflowing 'velocity'}\\ \lambda_{\mathrm{c}}=\tau_{\mathrm{c}}^{-1}}} \quad \underbrace{\widetilde{C}_j(t-\tau_{\mathrm{e}})}_{\substack{\text{precursor population in core}\\ \text{at } t-\tau_e \,\hat{=}\, \text{before passing}\\ \text{through external loop}}} \quad \underbrace{\mathrm{e}^{-\tau_{\mathrm{e}}\lambda_j}}_{\substack{\text{decay of precursors}\\ \text{in external loop}}} . \tag{4-28}$$

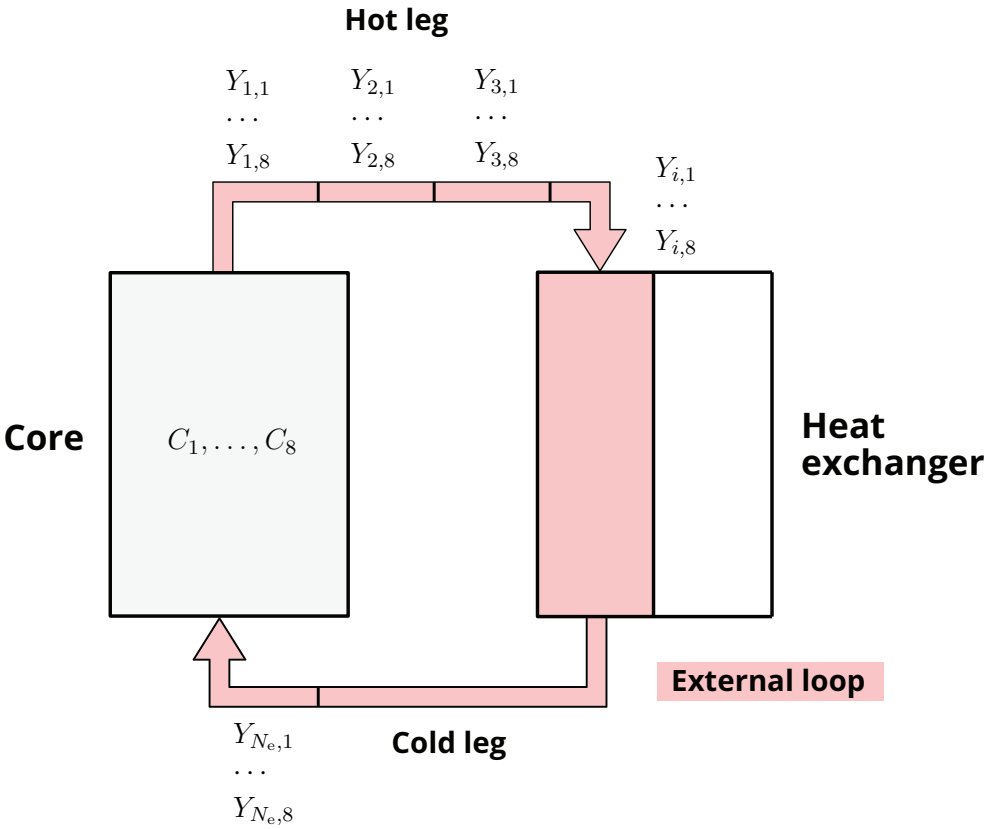

Figure 4-8: Discretised regions for the delayed neutron precursors of the MSFR model.

The time delay can be removed by introducing a new variable $Y_{i,j}(t)$, which represents the delayed neutron precursor population of group j in a region i of the external loop of the MSFR. The external loop comprises the hot leg, the heat exchanger and the cold leg of the plant. Figure 4-8 depicts the discretisation of the external loop regarding the delayed neutron precursors.

Using the variable $Y_{i,j}(t)$, Eq. 4-28 can be recast as

$$\lambda_c \widetilde{C}_j(t-\tau_e) e^{-\tau_e \lambda_j} = \lambda_c Y_{N_e,j}(t) \ . \tag{4-29}$$

where N_e refers to the last region of the external loop before the inlet of the core. Thus, Eq. 4-27 can be rewritten without any delayed variable as

$$\frac{d\widetilde{C}_j(t)}{dt} = \frac{\beta_j}{\Lambda} P(t) - \lambda_j \widetilde{C}_j(t) - \lambda_c \widetilde{C}_j(t) + \lambda_c Y_{N_e,j}(t) \ . \tag{4-30}$$

The ODE equation for characterising the dynamical development of the precursors $Y_{i,j}(t)$

in the external loop is presented here:

$$\underbrace{\frac{\mathrm{d}Y_{i,j}(t)}{\mathrm{d}t}}_{\substack{\text{change of precursor}\\ \text{population in external region } i}} = \underbrace{\lambda_\mathrm{e} N_\mathrm{e} Y_{i-1,j}(t)}_{\substack{\text{precursors flowing}\\ \text{into external region } i}} - \underbrace{\lambda_j Y_{i,j}(t)}_{\text{decaying precursors}} - \underbrace{\lambda_\mathrm{e} N_\mathrm{e} Y_{i,j}(t)}_{\substack{\text{precursors flowing}\\ \text{out of external region } i}} \quad \begin{aligned} &\text{for } i = 2 \dots N_\mathrm{e} \\ &\text{and } j = 1 \dots 8 \end{aligned} \tag{4-31}$$

and for $i = 1$:

$$\frac{\mathrm{d}Y_{1,j}(t)}{\mathrm{d}t} = \lambda_\mathrm{e} N_\mathrm{e} \widetilde{C}_j(t) - \lambda_j Y_{1,j}(t) - \lambda_\mathrm{e} N_\mathrm{e} Y_{1,j}(t) \quad \text{for } j = 1 \dots 8\,. \tag{4-32}$$

The factor $\lambda_\mathrm{e} N_\mathrm{e} = \frac{1}{\frac{\tau_\mathrm{e}}{N_\mathrm{e}}}$ represents the inverse of the time needed to pass through a region i.

Rewriting the differential equation of the delayed neutron precursors affects the associated reactivity contribution ρ_0. The term ρ_0 compensates for the in- and outflux of the precursors in the core and can be determined by solving the equation system 4-21, 4-30, 4-31 and 4-32 for steady-state conditions. This yields

$$\rho_0 = \beta - \sum_{j=1}^{n} \frac{\beta_j \lambda_j}{\lambda_j + \lambda_c - \lambda_c \Big(\frac{\lambda_\mathrm{e} N_\mathrm{e}}{\lambda_j + \lambda_\mathrm{e} N_\mathrm{e}} \Big)^{N_\mathrm{e}}}\,. \tag{4-33}$$

4.4.3 Salt Temperature Equation Adjustments

The equations for the salt temperatures in the first region of the core and heat exchanger contain the delayed variables $T_{\mathrm{c},N_\mathrm{c}}(t-\tau_1)$ and $T_{\mathrm{he},N_\mathrm{he}}(t-\tau_2)$:

$$\frac{\mathrm{d}T_{\mathrm{c},1}(t)}{\mathrm{d}t} = \frac{f_1}{M_{\mathrm{c},1}\, c} P(t) + \frac{W}{M_{\mathrm{c},1}} \Big(T_{\mathrm{he},N_\mathrm{he}}(t-\tau_2) - T_{\mathrm{c},1}(t) \Big) \tag{4-34}$$

$$\frac{\mathrm{d}T_{\mathrm{he},1}(t)}{\mathrm{d}t} = \frac{W}{M_{\mathrm{he},1}} \Big(T_{\mathrm{c},N_\mathrm{c}}(t-\tau_1) - T_{\mathrm{he},1}(t) \Big) + \frac{K_1}{M_{\mathrm{he},1}\, c} \Big(T_\mathrm{ic} - T_{\mathrm{he},1}(t) \Big)\,. \tag{4-35}$$

As can be seen, the inlet temperature of the core corresponds to the temperature of the last heat exchanger region $T_{\mathrm{he},N_\mathrm{he}}$ at $t - \tau_2$ before passing through the cold leg of the ex-

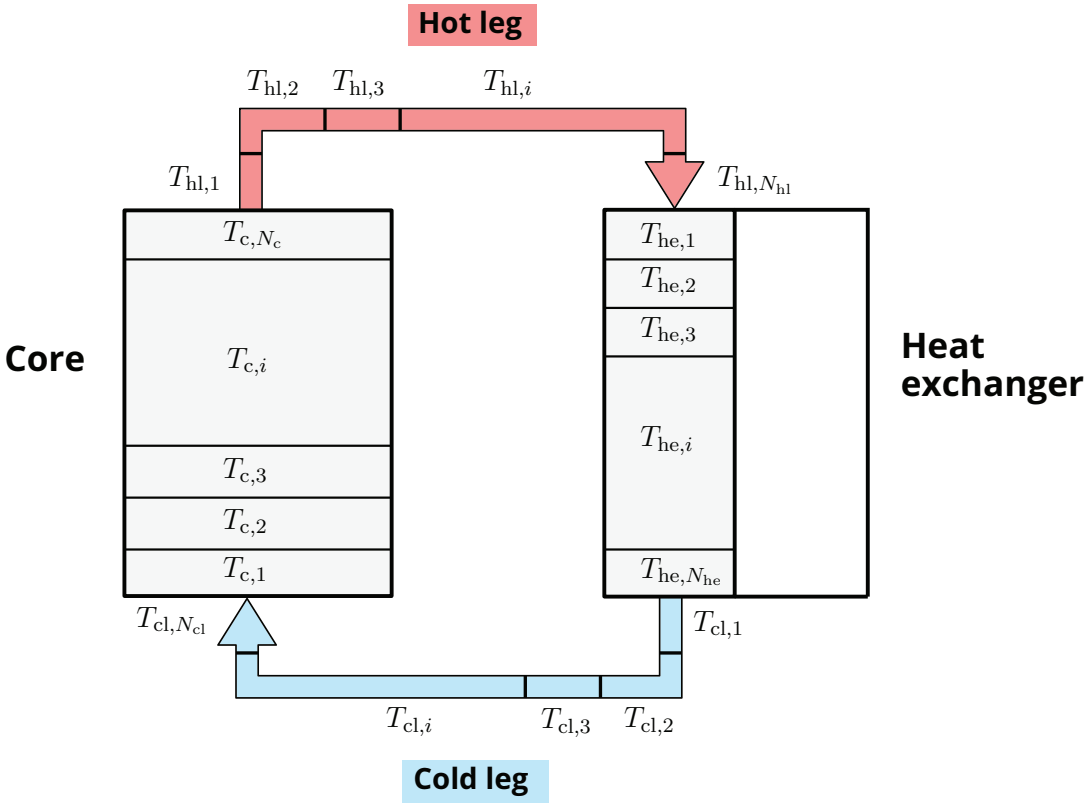

Figure 4-9: Discretised regions for the salt temperatures of the MSFR model.

ternal loop. Likewise, the salt temperature at the heat exchanger inlet is assumed to be the temperature of the last core region $T_{\mathrm{c},N_{\mathrm{c}}}$ at $t - \tau_1$ before flowing through the hot leg. The terms τ_1 and τ_2 denote the passage times of the hot and cold leg of the external loop, respectively.

Both delays are removed by introducing additional temperature variables $T_{\mathrm{cl},i}(t)$ and $T_{\mathrm{hl},i}(t)$. These variables denote the salt temperatures in a region i of the cold leg and hot leg of the external loop. Figure 4-9 illustrates the salt temperature discretisation of the model.

The delayed variables are substituted in the following way:

$$T_{\mathrm{he},N_{\mathrm{he}}}(t - \tau_2) = T_{\mathrm{cl},N_{\mathrm{cl}}}(t) \tag{4-36}$$

$$T_{\mathrm{c},N_{\mathrm{c}}}(t - \tau_1) = T_{\mathrm{hl},N_{\mathrm{hl}}}(t) \tag{4-37}$$

where N_{cl} corresponds to the last region of the cold leg before entering the core, and N_{hl} corresponds to the last region of the hot leg before entering the heat exchanger.

Using $T_{\mathrm{cl},N_{\mathrm{cl}}}(t)$ and $T_{\mathrm{hl},N_{\mathrm{hl}}}(t)$, Eqs. 4-34 and 4-35 can be expressed as ODEs:

$$\frac{\mathrm{d}T_{\mathrm{c},1}(t)}{\mathrm{d}t} = \frac{f_1}{M_{\mathrm{c},1}\,c}P(t) + \frac{W}{M_{\mathrm{c},1}}\Big(T_{\mathrm{cl},N_{\mathrm{cl}}}(t) - T_{\mathrm{c},1}(t)\Big) \tag{4-38}$$

$$\frac{\mathrm{d}T_{\mathrm{he},1}(t)}{\mathrm{d}t} = \frac{W}{M_{\mathrm{he},1}}\Big(T_{\mathrm{hl},N_{\mathrm{hl}}}(t) - T_{\mathrm{he},1}(t)\Big) + \frac{K_1}{M_{\mathrm{he},1}\,c}\Big(T_{\mathrm{ic}} - T_{\mathrm{he},1}(t)\Big)\,. \tag{4-39}$$

The dynamical evolution of variables $T_{\mathrm{cl},i}(t)$ and $T_{\mathrm{hl},i}(t)$ is described by the following equations:

$$\frac{\mathrm{d}T_{\mathrm{cl},i}(t)}{\mathrm{d}t} = \frac{W}{M_{\mathrm{cl},i}}\Big(T_{\mathrm{cl},i-1}(t) - T_{\mathrm{cl},i}(t)\Big) \quad \text{for } i = 2\ldots N_{\mathrm{cl}} \tag{4-40}$$

$$\frac{\mathrm{d}T_{\mathrm{hl},i}(t)}{\mathrm{d}t} = \frac{W}{M_{\mathrm{hl},i}}\Big(T_{\mathrm{hl},i-1}(t) - T_{\mathrm{hl},i}(t)\Big) \quad \text{for } i = 2\ldots N_{\mathrm{hl}} \tag{4-41}$$

and for $i = 1$ as

$$\frac{\mathrm{d}T_{\mathrm{cl},1}(t)}{\mathrm{d}t} = \frac{W}{M_{\mathrm{cl},1}}\Big(T_{\mathrm{he},N_{\mathrm{he}}}(t) - T_{\mathrm{cl},1}(t)\Big) \tag{4-42}$$

$$\frac{\mathrm{d}T_{\mathrm{hl},1}(t)}{\mathrm{d}t} = \frac{W}{M_{\mathrm{hl},1}}\Big(T_{\mathrm{c},N_{\mathrm{c}}}(t) - T_{\mathrm{hl},1}(t)\Big)\,. \tag{4-43}$$

The mass of the salt in each region i of the cold leg of the external loop $M_{\mathrm{cl},i}$ can be determined as

$$M_{\mathrm{cl},i} = \frac{M_{\mathrm{cl}}}{N_{\mathrm{cl}}} = \frac{W\tau_2}{N_{\mathrm{cl}}} = \frac{11\,378\,\mathrm{kg}}{N_{\mathrm{cl}}} \tag{4-44}$$

for the parameter set of Table 4-3. The mass $M_{\mathrm{hl},i}$ can be calculated analogously.

4.4.4 Nonlinear System of Ordinary Differential Equations

Using Eqs. 4-30, 4-38 and 4-39, the nonlinear DDE system (Eqs. 4-21 to 4-26) can be rewritten as the following nonlinear ODE system:

$$\frac{\mathrm{d}P(t)}{\mathrm{d}t} = \frac{\rho_0 + \rho_{\mathrm{t}}(t) + \rho_{\mathrm{ex}}(t) - \beta}{\Lambda}P(t) + \sum_{j=1}^{8}\lambda_j\widetilde{C}_j(t) \tag{4-45}$$

with $\rho_{\mathrm{t}}(t) = \alpha_{\mathrm{ex}}\Big(T_{\mathrm{c}}^{*}(t) - T_{\mathrm{c0}}^{*}\Big) + K_{\mathrm{D}} \ln\left(\frac{T_{\mathrm{c}}^{*}(t)}{T_{\mathrm{c0}}^{*}}\right)$

and $T_{c}^{*}(t) = \frac{1}{N_{\mathrm{c}}} \sum_{i=1}^{N_{\mathrm{c}}} T_{c,i}(t)$

$$\frac{\mathrm{d}\widetilde{C}_j(t)}{\mathrm{d}t} = \frac{\beta_j}{\Lambda} P(t) - (\lambda_j + \lambda_{\mathrm{c}})\widetilde{C}_j(t) + \lambda_{\mathrm{c}} Y_{N_{\mathrm{e}},j}(t) \tag{4-46}$$

for $j = 1 \ldots 8$

$$\frac{\mathrm{d}T_{\mathrm{c},1}(t)}{\mathrm{d}t} = \frac{f_1}{M_{\mathrm{c},1}\, c} P(t) + \frac{W}{M_{\mathrm{c},1}}\Big(T_{\mathrm{cl},N_{\mathrm{cl}}}(t) - T_{\mathrm{c},1}(t)\Big) \tag{4-47}$$

$$\frac{\mathrm{d}T_{\mathrm{c},i}(t)}{\mathrm{d}t} = \frac{f_i}{M_{\mathrm{c},i}\, c} P(t) + \frac{W}{M_{\mathrm{c},i}}\Big(T_{\mathrm{c},i-1}(t) - T_{\mathrm{c},i}(t)\Big) \tag{4-48}$$

for $i = 2, \ldots, N_{\mathrm{c}}$

$$\frac{\mathrm{d}T_{\mathrm{he},1}(t)}{\mathrm{d}t} = \frac{W}{M_{\mathrm{he},1}}\Big(T_{\mathrm{hl},N_{\mathrm{hl}}}(t) - T_{\mathrm{he},1}(t)\Big) + \frac{K_1}{M_{\mathrm{he},1}\, c}\Big(T_{\mathrm{ic}} - T_{\mathrm{he},1}(t)\Big) \tag{4-49}$$

$$\frac{\mathrm{d}T_{\mathrm{he},i}(t)}{\mathrm{d}t} = \frac{W}{M_{\mathrm{he},i}}\Big(T_{\mathrm{he},i-1}(t) - T_{\mathrm{he},i}(t)\Big) + \frac{K_i}{M_{\mathrm{he},i}\, c}\Big(T_{\mathrm{ic}} - T_{\mathrm{he},i}(t)\Big) \tag{4-50}$$

for $i = 2, \ldots, N_{\mathrm{he}}$.

$$\frac{\mathrm{d}Y_{1,j}(t)}{\mathrm{d}t} = \lambda_{\mathrm{e}} N_{\mathrm{e}} \widetilde{C}_j(t) - \lambda_j Y_{1,j}(t) - \lambda_{\mathrm{e}} N_{\mathrm{e}} Y_{1,j}(t)$$

for $j = 1 \ldots 8$

$$\frac{\mathrm{d}Y_{i,j}(t)}{\mathrm{d}t} = \lambda_{\mathrm{e}} N_{\mathrm{e}} Y_{i-1,j}(t) - \lambda_j Y_{i,j}(t) - \lambda_{\mathrm{e}} N_{\mathrm{e}} Y_{i,j}(t) \tag{4-51}$$

for $i = 2 \ldots N_{\mathrm{e}}$ and $j = 1 \ldots 8$

$$\frac{\mathrm{d}T_{\mathrm{cl},1}(t)}{\mathrm{d}t} = \frac{W}{M_{\mathrm{cl},1}}\Big(T_{\mathrm{he},N_{\mathrm{he}}}(t) - T_{\mathrm{cl},1}(t)\Big) \tag{4-52}$$

$$\frac{\mathrm{d}T_{\mathrm{cl},i}(t)}{\mathrm{d}t} = \frac{W}{M_{\mathrm{cl},i}}\Big(T_{\mathrm{cl},i-1}(t) - T_{\mathrm{cl},i}(t)\Big) \tag{4-53}$$

for $i = 2 \ldots N_{\mathrm{cl}}$

$$\frac{\mathrm{d}T_{\mathrm{hl},1}(t)}{\mathrm{d}t} = \frac{W}{M_{\mathrm{hl},1}}\Big(T_{\mathrm{c},N_{\mathrm{c}}}(t) - T_{\mathrm{hl},1}(t)\Big) \tag{4-54}$$

$$\frac{\mathrm{d}T_{\mathrm{hl},i}(t)}{\mathrm{d}t} = \frac{W}{M_{\mathrm{hl},i}}\Big(T_{\mathrm{hl},i-1}(t) - T_{\mathrm{hl},i}(t)\Big) \tag{4-55}$$

for $i = 2 \dots N_{\mathrm{hl}}$

4.4.5 Verification of the Nonlinear System of Ordinary Differential Equations

Different discretisation steps of the external loop are investigated for the nonlinear ODE system of Eqs. 4-45 to 4-55. In order to ensure reasonable computation times in MatCont, the number of equations, and therefore system variables, has to be kept as low as possible. Nevertheless, the quality of the model should not be significantly changed. Table 4-4 shows some of the different discretisation sets that have been analysed and the resulting total number of variables.

The nonlinear ODE system is implemented in MATLAB using the parameter set of Table 4-3. For each of the specified discretisation versions, the solutions for $P(t)$ and $T_{\mathrm{c},1}(t)$ are plotted over time t. The resulting graphs are compared to those of the nonlinear DDE system (Eqs. 4-21 to 4-26), in order to ascertain whether the ODEs reproduce the same dynamical behaviour.

Figure 4-10 shows the results of the ODE system in comparison to those of the DDE system with $N_{\mathrm{c}} = N_{\mathrm{he}} = 10$, considering a reactivity insertion of $\rho_{\mathrm{ex}} = 10^{-5}$. The corresponding MATLAB file is listed in Appendix F.

As can be seen in Figure 4-10, there is a deviation between the plots of the DDE and the ODE system for option 1 of the presented discretisation sets. Also, some oscillation peaks are smoothed away in the ODE plots. The ODE system using the second discretisation option approximates the time series plots of the delayed system more precisely. For option

Table 4-4: Some of the analysed discretisation sets of the nonlinear ODE MSFR model (Eqs. 4-45 to 4-55)

Option	$\boldsymbol{N}_{\mathrm{c}}$	$\boldsymbol{N}_{\mathrm{he}}$	$\boldsymbol{N}_{\mathrm{e}}$	$\boldsymbol{N}_{\mathrm{cl}} = \boldsymbol{N}_{\mathrm{hl}}$	**Total number of variables**
1	6	6	1	1	31
2	10	10	4	4	69
3	10	10	10	10	129

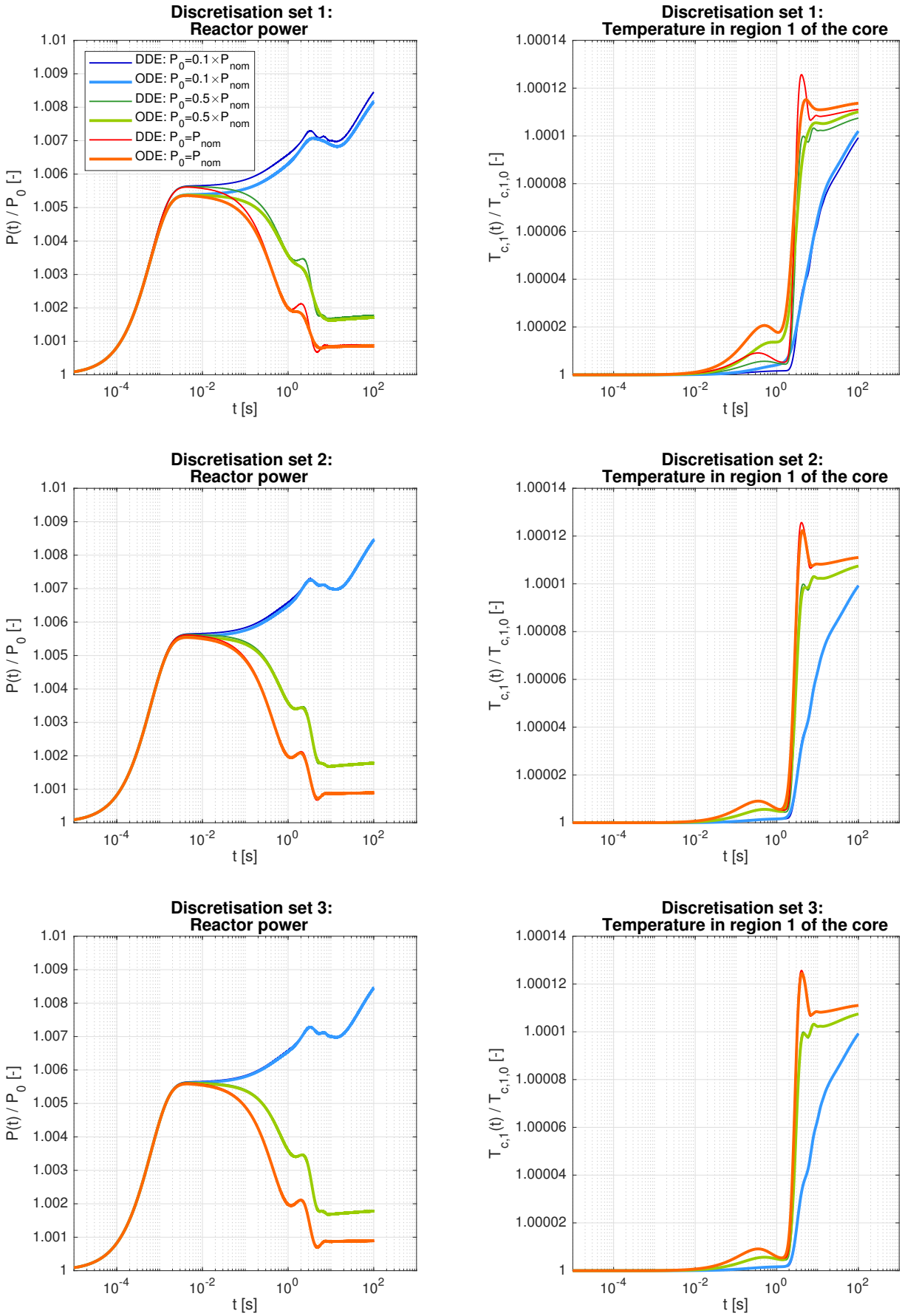

Figure 4-10: Time series plots of $P(t)$ and $T_{\mathrm{c},1}(t)$ of the nonlinear ODE system (Eqs. 4-45 to 4-55) for the discretisation sets of Table 4-4, compared to those of the nonlinear DDE system (Eqs. 4-21 to 4-26, $N_{\mathrm{c}} = N_{\mathrm{he}} = 10$).

3, which uses the highest number of variables, there is hardly any difference observable between the curves of the ODE and DDE system.

Altogether, discretisation data set 2 is chosen for the numerical system in MatCont, as it provides the most favourable compromise between model quality and simplicity.

5 CONDUCTED STABILITY ANALYSES

5.1 Introduction

This chapter contains the stability analyses performed for the specified ODE system of the MSFR. The equation system is prepared for MatCont by expressing the state variables $\boldsymbol{x}(t)$ relative to their fixed-point values $\boldsymbol{X}_0$ of the steady state. MatCont analyses the fixed point of the MSFR system while the values of selected control parameters are varied. The relevant parameters and their domain of variation are presented in this chapter, as well as the resulting MatCont plots. In order to help interpreting and explaining the results, appropriate time series plots are created and analysed.

The next step focusses on a linear stability analysis of the MSFR model. First, the time series plots of the linearised system are compared to those of the nonlinear one in order to assess the quality of the linearised version. Then the eigenvalues of the Jacobian matrix at the fixed point are evaluated in order to investigate the stability at this state in linear terms. This method is applied for different parameter sets, and the results are compared to the findings of the nonlinear stability analysis.

At last, the general reliability of the MatCont software and the precision of its stability assessments are examined. Therefore, an additional reactor model is analysed – the Molten Salt Breeder Reactor (MSBR). The stability boundaries of this reactor design have been specified by the reference article [7], and it is checked whether MatCont obtains a similar outcome.

5.2 Nonlinear Stability Analysis

5.2.1 Implementation

The nonlinear ODE system (Eqs. 4-45 to 4-55) of the presented MSFR model has the following fixed point for steady-state conditions, satisfying Eq. 3-6:

$$\boldsymbol{X}_0 = \Big(P_0 \quad \widetilde{C}_{1,0} \dots \widetilde{C}_{8,0} \quad T_{\mathrm{c},1,0} \dots T_{\mathrm{c},N_\mathrm{c},0} \quad T_{\mathrm{he},1,0} \dots T_{\mathrm{he},N_\mathrm{he},0} \quad \dots \\ Y_{1,1,0} \dots Y_{N_\mathrm{he},8,0} \quad T_{\mathrm{cl},1,0} \dots T_{\mathrm{cl},N_\mathrm{cl},0} \quad T_{\mathrm{hl},1,0} \dots T_{\mathrm{hl},N_\mathrm{hl},0} \Big)^\top .$$

The system of equations is transformed so that the evolution of the system variables

$$\boldsymbol{x}(t) = \Big(P(t) \quad \widetilde{C}_1(t) \dots \widetilde{C}_8(t) \quad T_{\mathrm{c},1}(t) \dots T_{\mathrm{c},N_\mathrm{c}}(t) \quad T_{\mathrm{he},1}(t) \dots T_{\mathrm{he},N_\mathrm{he}}(t) \quad \dots \\ Y_{1,1}(t) \dots Y_{N_\mathrm{he},8}(t) \quad T_{\mathrm{cl},1}(t) \dots T_{\mathrm{cl},N_\mathrm{cl}}(t) \quad T_{\mathrm{hl},1}(t) \dots T_{\mathrm{hl},N_\mathrm{hl}}(t) \Big)^\top$$

can be referred to the values of the fixed point $\boldsymbol{X}_0$. This helps MatCont to converge its computations since all variables are in a similar order of magnitude.

Said transformation is achieved by introducing new variables

$$\widehat{x}_i(t) = \frac{x_i(t)}{X_{0,i}} \tag{5-1}$$

which express the change of a state variable $x_i(t) \in \boldsymbol{x}(t)$ relative to its fixed-point value $X_{0,i} \in \boldsymbol{X}_0$.

The MSFR equation system is adapted accordingly using the new, relative state variables:

$$\widehat{\boldsymbol{x}}(t) = \Big(\widehat{P}(t) \quad \widehat{C}_1(t) \dots \widehat{C}_8(t) \quad \widehat{T}_{\mathrm{c},1}(t) \dots \widehat{T}_{\mathrm{c},N_\mathrm{c}}(t) \quad \widehat{T}_{\mathrm{he},1}(t) \dots \widehat{T}_{\mathrm{he},N_\mathrm{he}}(t) \quad \dots \\ \widehat{Y}_{1,1}(t) \dots \widehat{Y}_{N_\mathrm{he},8}(t) \quad \widehat{T}_{\mathrm{cl},1}(t) \dots \widehat{T}_{\mathrm{cl},N_\mathrm{cl}}(t) \quad \widehat{T}_{\mathrm{hl},1}(t) \dots \widehat{T}_{\mathrm{hl},N_\mathrm{hl}}(t) \Big)^\top .$$

The transformation of the equation system is explained in detail in Appendix C.1. The transformed system is subsequently implemented in MATLAB code with a discretisation according to option 2 of the given sets in Table 4-4.

The numerical tool MatCont uses the MATLAB code to perform dynamical and bifurcation analyses. Within the frame of this work, a fixed-point analysis for the MSFR system is carried out in MatCont. Therefore, the software varies selected parameter values and tracks the behaviour of the fixed point.

The parameters c_k to be investigated are chosen such that only parameters depending on the reactor design or the salt composition are considered. That excludes the neutronic data, as well as the externally supplied reactivity ρ_{ex}, which can be treated as an input variable. The temperature of the intermediate salt T_{ic} is not considered either because it is not a design parameter. In fact, it should be regarded as a variable since it depends on the other state variables. However, this work considers the model presented in paper [7], and therefore a constant value of $806.4\,\mathrm{K}$ is assigned to T_{ic}, which is obtained by solving the specified system for the steady-state conditions provided in Appendix C.1. Further studies should include an additional correlation for $T_{\mathrm{ic}}(t)$.

Table 5-1 presents the parameters c_k to be investigated, their default values $c_{k,0}$ and their domain of variation $c_{k,\mathrm{min}} \ldots c_{k,\mathrm{max}}$. Most parameter values are taken from Table 4-3. Eq. 4-44 provides the values of the salt masses M_{cl} and M_{hl} in the cold and hot leg.

Table 5-1: Varied parameters for the bifurcation analysis in MatCont

Parameter	**Symbol**	**Unit**	**Default Value**	**Domain of variation**
	$\boldsymbol{c_k}$		$\boldsymbol{c_{k,0}}$	$\boldsymbol{c_{k,\mathrm{min}} \ldots c_{k,\mathrm{max}}}$
Density feedback coefficient of the salt	α_{ex}	K^{-1}	$-2.53 \cdot 10^{-5}$	$-1 \cdot 10^{-4} \ \ldots \ 0$
Doppler constant	K_{D}	$-$	$-4046 \cdot 10^{-5}$	$-0.1 \ \ldots \ 0$
Mass of salt in the core	M_{c}	kg	$36\,980$	$0 \ \ldots \ 100\,000$
Mass of salt in the heat exchangers	M_{he}	kg	$14\,223$	$0 \ \ldots \ 100\,000$
Salt flow rate in the primary circuit	W	$\mathrm{kg\ s}^{-1}$	$18\,964$	$0 \ \ldots \ 100\,000$
Overall heat transfer coefficient between the primary and intermediate salt	K	$\mathrm{W\ K}^{-1}$	$19.8 \cdot 10^6$	$0 \ \ldots \ 1 \cdot 10^8$
Mass of salt in the cold leg	M_{cl}	kg	$11\,378$	$0 \ \ldots \ 100\,000$
Mass of salt in the hot leg	M_{hl}	kg	$11\,378$	$0 \ \ldots \ 100\,000$

The domain for the parameter variation was chosen broadly such that a wide range of

values can be evaluated. Parameter values that are distant from the default values nevertheless need to be investigated since bifurcating solutions could possibly be traced back to the default parameter region, in case bifurcations are found. Yet, parameter values that fall below physically reasonable limits, e.g. negative values for the salt masses, are not considered. The upper boundary for most parameters was selected to be one order of magnitude greater than the default value. Regarding the feedback parameters α_{ex} and K_{D}, the maximum value is set to zero, because a change of sign is considered physically unrealistic.

The parameters τ_{c} and τ_{e}, representing the core and external loop transit times, as well as their inverse values λ_{c} and λ_{e}, depend on the changing values of the salt masses and flow rate. These relationships are described by the following equations, which are also included in the MatCont model:

$$\tau_{\mathrm{c}} = \frac{M_{\mathrm{c}}}{W} \tag{5-2}$$

$$\tau_{\mathrm{e}} = \frac{M_{\mathrm{he}} + M_{\mathrm{cl}} + M_{\mathrm{hl}}}{W} \tag{5-3}$$

$$\lambda_{\mathrm{c}} = \frac{1}{\tau_{\mathrm{c}}} \tag{5-4}$$

$$\lambda_{\mathrm{e}} = \frac{1}{\tau_{\mathrm{e}}} \,. \tag{5-5}$$

The overall heat transfer coefficient K also depends on the salt temperatures in the primary and secondary side of the heat exchanger $T_{\mathrm{he},i}$ and T_{ic}. However, setting up an equation for this correlation and including it in the MatCont model is beyond the scope of this work.

5.2.2 Results

In order to determine bifurcation points, MatCont evaluates the fixed point of the ODE system at each value during the parameter variation. Concerning the outcome of the analysis, it is irrelevant, which variable of the fixed point is displayed on the ordinate axis in the resulting plots. The reactor power is considered to be the key variable, and hence it is chosen here.

The plots in Figure 5-1 show the relative reactor power $\widehat{P}_0(c_k)$ at the fixed point as the

selected control parameters c_k get varied. All other parameters correspond to the given values in Table 4-3. The relative reactor power of the fixed point $\widehat{P}_0(c_k) = \frac{P_0(c_k)}{P_0(c_{k,0})}$ expresses the fixed-point power $P_0(c_k)$ at the changing parameter value with respect to the fixed-point power $P_0(c_{k,0})$ at the original parameter value. The black point markers indicate $\widehat{P}_0 = 1$ at the default parameter values. The MatCont settings for those analyses are listed in Appendix C.2.

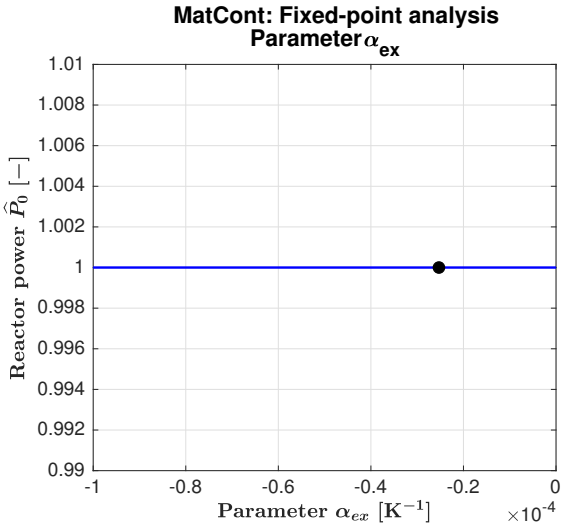

(a) Fixed-point analysis for parameter α_{ex}

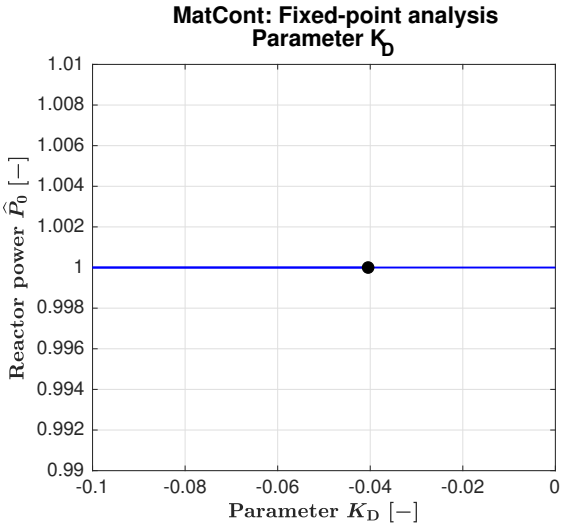

(b) Fixed-point analysis for parameter K_{D}

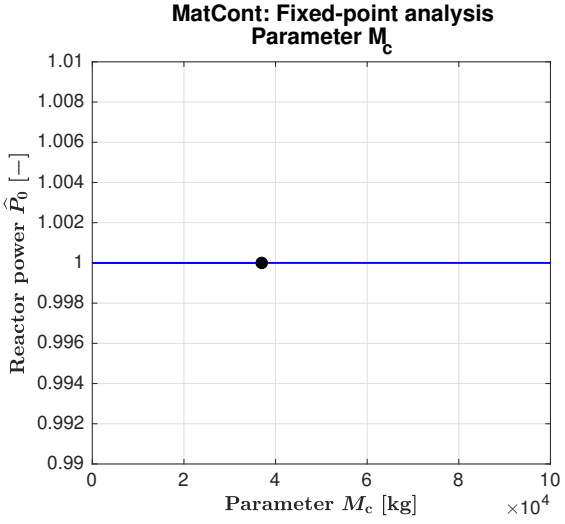

(c) Fixed-point analysis for parameter M_{c}

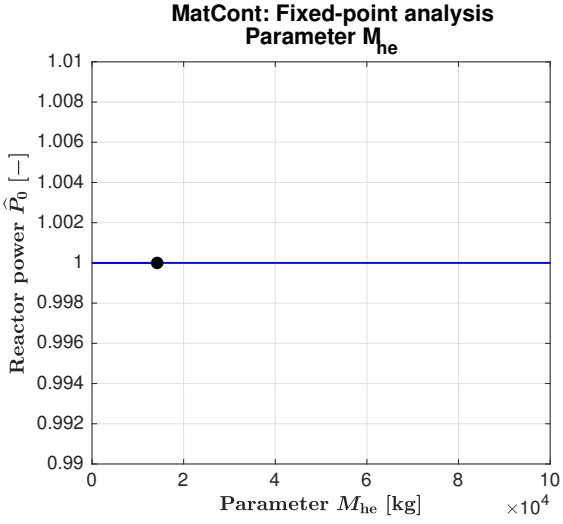

(d) Fixed-point analysis for parameter M_{he}

Figure 5-1: Relative reactor power $\widehat{P}_0$ of the steady-state fixed point of the MSFR as selected control parameters c_k get varied (continued on the following page).

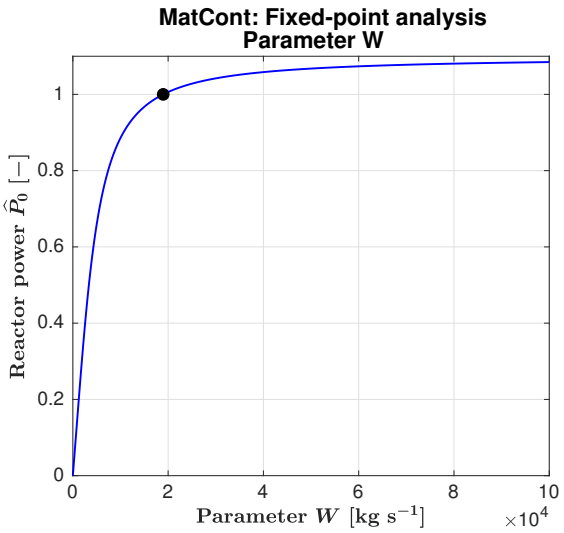

(e) Fixed-point analysis for parameter W

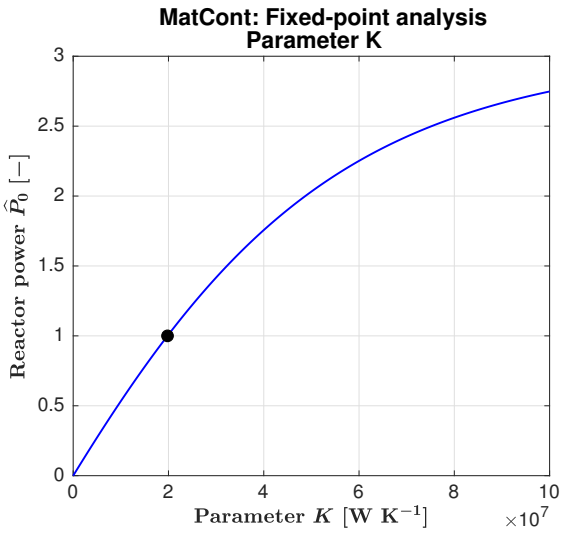

(f) Fixed-point analysis for parameter K

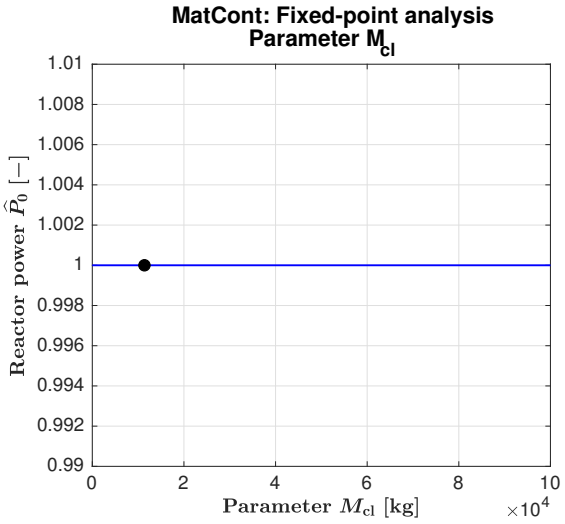

(g) Fixed-point analysis for parameter M_{cl}

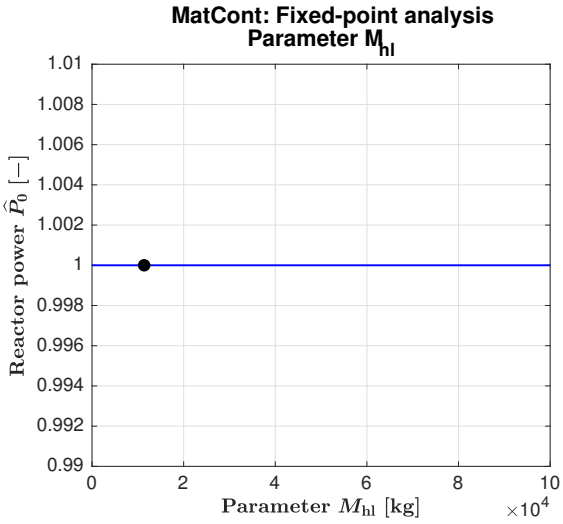

(h) Fixed-point analysis for parameter M_{hl}

Figure 5-1: Relative reactor power $\widehat{P}_0$ of the steady-state fixed point of the MSFR as selected control parameters c_k get varied.

5.2.3 Interpretation

The plots of Figure 5-1 show no bifurcation points for the selected parameters in their domain of variation. Hence, the steady-state fixed point does not change its stability state for any of the considered parameter changes.

It is assumed that the fixed point $\boldsymbol{X}_0$ is an asymptotically stable one, and therefore all state variables $\boldsymbol{x}(t)$ would approach $\boldsymbol{X}_0$ for $t \to \infty$. This would happen irrespective of the initial conditions $\boldsymbol{x}(t_0)$. Those assumptions are verified when analysing the phase space of the

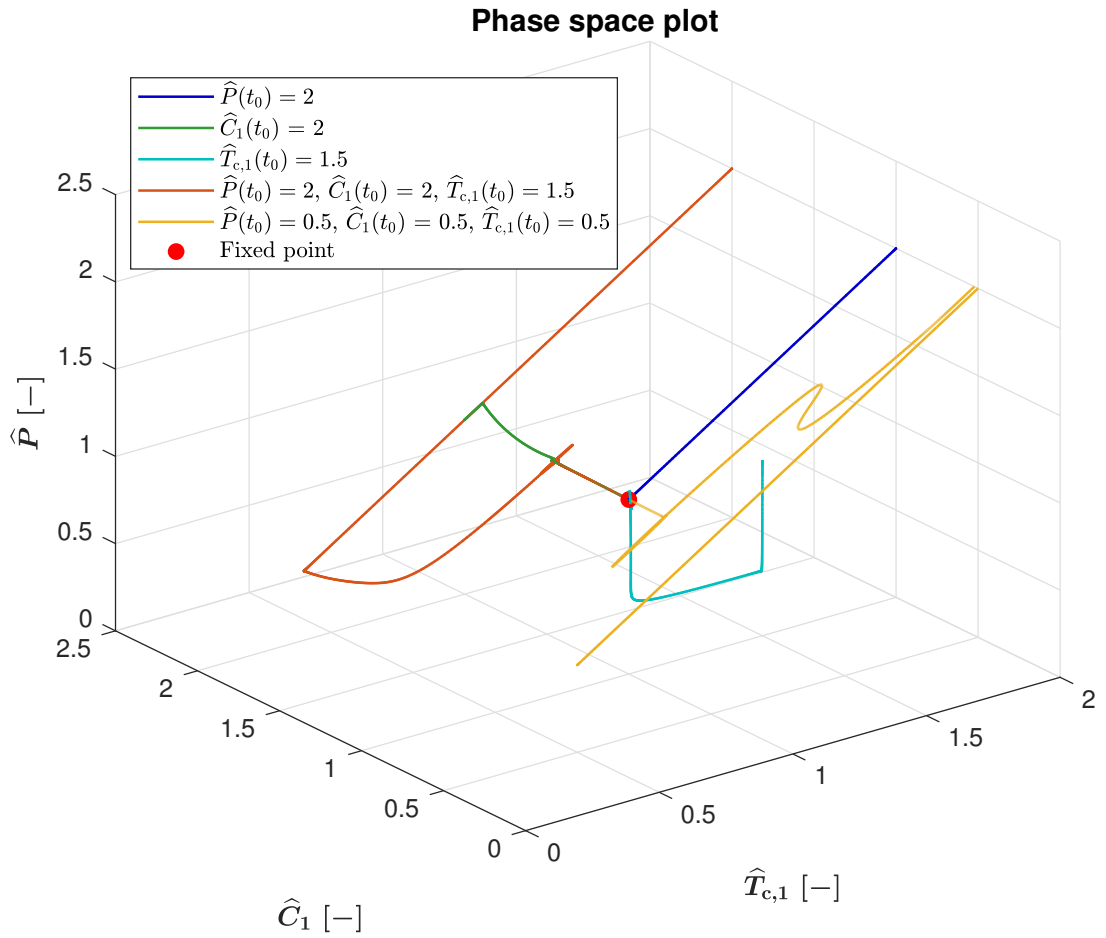

Figure 5-2: Plot of some trajectories of the specified MSFR system for different initial conditions in a three-dimensional phase space projection.

system. Figure 5-2 shows some plotted trajectories of the MSFR system for different initial conditions in a three-dimensional phase space projection. The red point marker indicates the steady-state fixed point. It is visible that all trajectories approach the fixed point with progressing time.

Thus, the fixed point $\boldsymbol{X}_0$ is confirmed to be asymptotically stable according to Lyapunov (see Section 3.3.3). Furthermore, it is very likely to be globally stable in phase space since no bifurcations have been found. Based on the specified model (Eqs. 4-45 to 4-55), the MSFR system is considered to be a stable one for all parameter variations given in Table 5-1.

It should be noted that the considered parameter changes only constitute straight lines in the parameter space, which is spanned by all independent control parameters c_k. The majority of possible multidimensional parameter combinations is left unexplored. How-

ever, concerning the specified parameter set of the MSFR, it is sufficient to consider one-dimensional variations, since the stability analysis is done under the assumption of normal operation and not for accident conditions.

A detailed analysis and verification of all fixed-point plots (Figure 5-1) is carried out in the following.

Parameters α_{ex} and K_D

The variation of the feedback parameters α_{ex} and K_{D} does not influence the fixed-point value of the reactor power according to the MatCont plots 5-1a and 5-1b.

This behaviour can be explained by analysing the time-depending evolution of the power and temperature in the core. Figure 5-3 shows the time series plots of the reactor power and salt temperature (core region 10) for different values of α_{ex} with an initial power deflection $\widehat{P}(t_0 = 0) = 1.1$.

The parameters K_{D} and α_{ex} determine the reactivity feedback resulting from the average salt temperature in the core. If the density feedback coefficient α_{ex} gets more negative, and therefore the corresponding feedback contribution as well, the reactor power falls slightly. The power curves in Figure 5-3 do not seem to show any significant variation for different α_{ex}. However, looking at a zoomed-in segment reveals that the reactor power does evolve differently. It is obvious that more negative values of α_{ex} result in sharper power drops.

As can be seen, a lower reactor power leads to lower core temperature peaks. This results in a less negative reactivity feedback, which causes the power to rise again. The cycle of interaction between reactor power, core salt temperature and reactivity feedback adapts dynamically and eventually leads to the fixed-point value $\widehat{P}_0 = 1$. The same principle applies for the variation of K_{D}.

All power curves in Figure 5-3 end at the same steady-state fixed point $\widehat{P}_0 = 1$, therefore verifying the results obtained in the MatCont plots 5-1a and 5-1b.

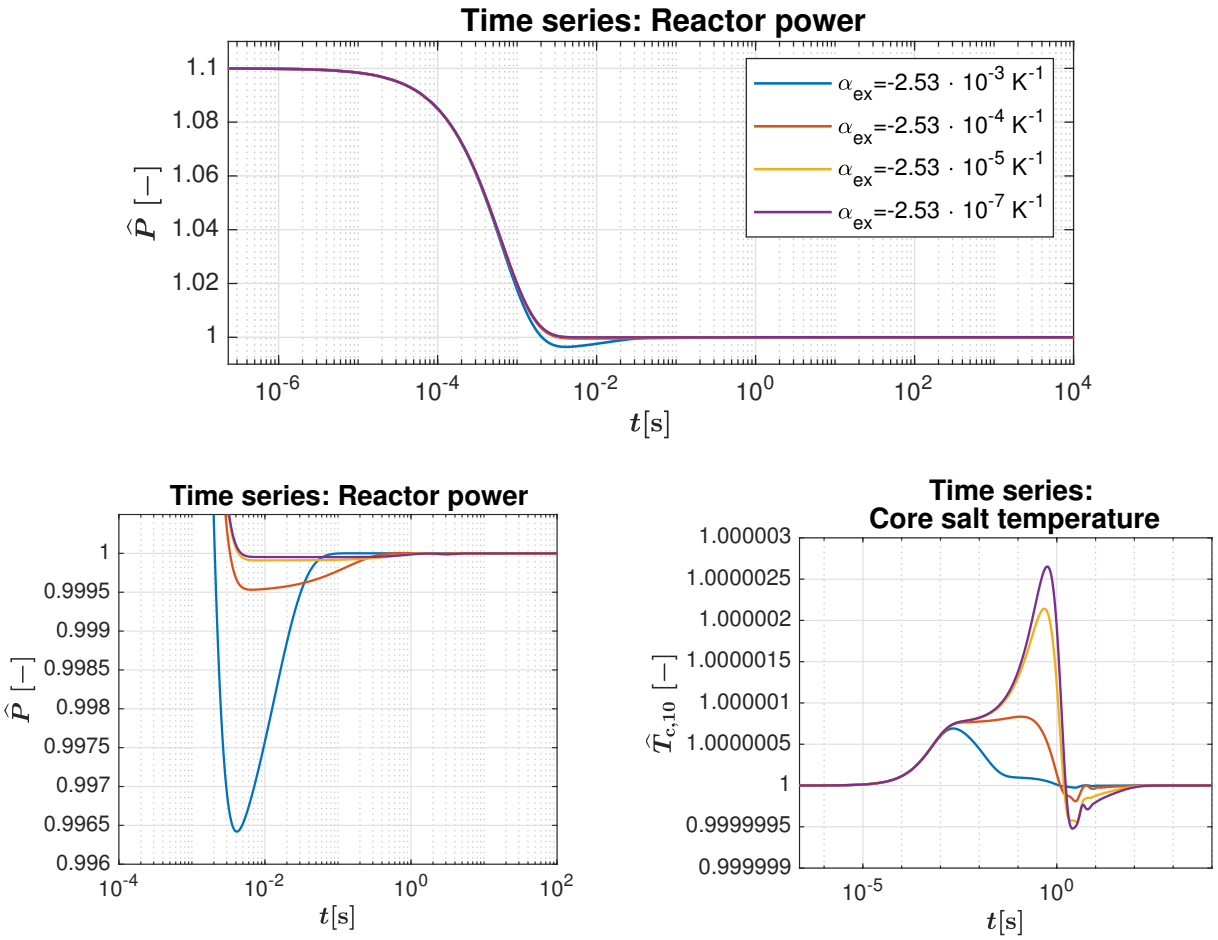

Figure 5-3: Time series plots of the reactor power $\widehat{P}$ and the salt temperature $\widehat{T}_{\mathrm{c},10}$ for the initial condition $\widehat{P}(t_0 = 0) = 1.1$ and different values of α_{ex}.

Parameters M_c, M_{he}, M_{cl} and M_{hl}

Like the feedback parameters α_{ex} and K_{D}, the salt masses M_{c}, M_{he}, M_{cl} and M_{hl} do not affect the value of $\widehat{P}_0$ when being varied.

The behaviour shall be explained in an exemplary way for parameter M_{c}, representing the mass of salt in the core. For this purpose, the time series of the reactor power, core salt temperature (core region 10) and delayed neutron precursors (group 1) are presented in Figure 5-4 in regard to an initial power deflection.

In the following, an increase of M_{c} is considered. A higher salt mass in the core leads to an increase of the core transit time τ_{c} (see Eq. 5-2), and the delayed neutron precursors remain in the core for longer. As a consequence, the reactivity contribution ρ_0 that results from the circulation of the delayed neutron precursors gets smaller according to Eq. 4-33.

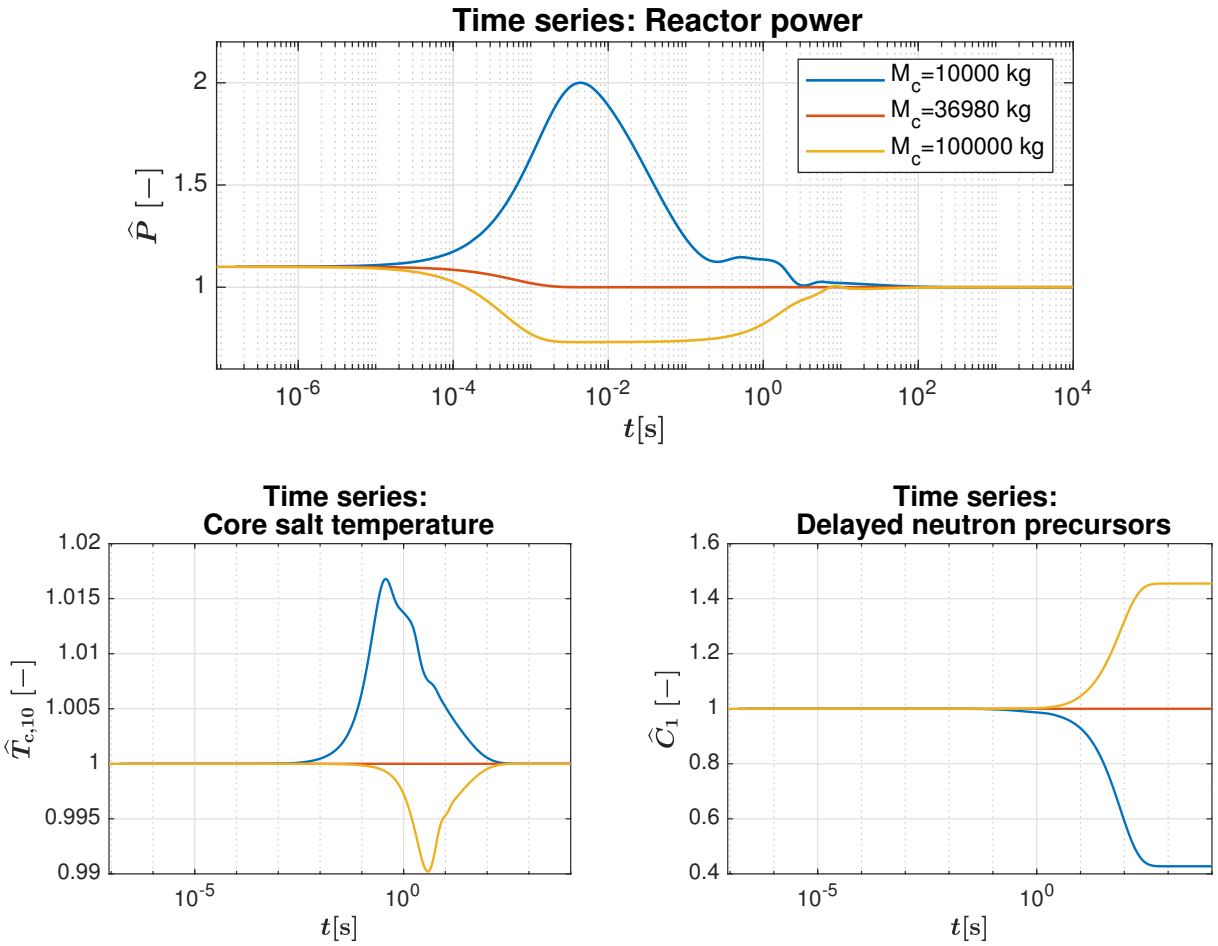

Figure 5-4: Time series plots of the reactor power $\widehat{P}$, the salt temperature $\widehat{T}_{\mathrm{c},10}$ and the delayed neutron precursors $\widehat{C}_1$ for the initial condition $\widehat{P}(t_0 = 0) = 1.1$ and different values of M_c.

This leads to a drop in the reactor power as can be observed in Figure 5-4.

It is also visible that if M_c increases, the temperature in the core is inclined to fall. Therefore, the reactivity contribution ρ_t is less negative and causes the power to rise again.

As described, an increased parameter M_c results in more delayed neutron precursors in the core. These eventually decay and lead to more fission reactions, also increasing the reactor power. The steady-state values for the delayed neutron precursor populations are higher for a greater value of M_c, as can be seen in Figure 5-4.

Eventually, both contributions, the increased decay rate and the reduced reactivity term ρ_0, level each other out and lead back to the fixed-point value $\widehat{P}_0 = 1$. The same principle applies for the variation of M_he, M_cl and M_hl, which induce a change in the external loop transit time τ_e (see Eq. 5-3).

The plotted reactor power returns to the fixed-point value $\widehat{P}_0 = 1$ for all values of M_c, which confirms the MatCont results of plot 5-1c.

Parameter W

Plot 5-1e shows that a higher salt flow rate W moves the fixed point to a higher power level $\widehat{P}_0$. On the other hand, if the salt flow rate reaches zero, the steady-state reactor power is zero as well. The behaviour can be explained by analysing the time plots in Figure 5-5.

It can be observed that the core temperatures are moving to a higher steady-state value if the salt flow rate decreases. Consequently, the reactivity contribution from the negative temperature feedback coefficient α_{ex} leads to a lower reactor power. If the salt flow rate

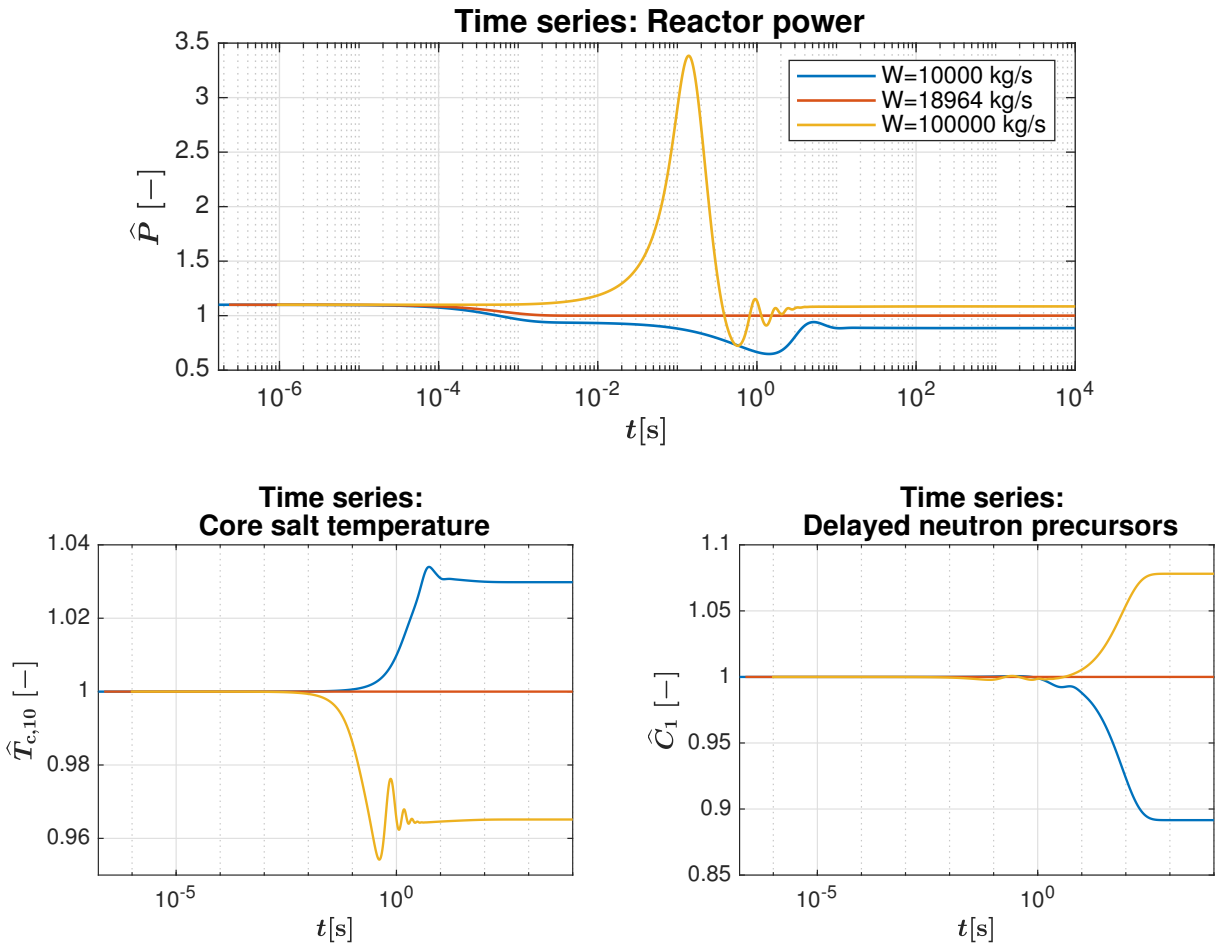

Figure 5-5: Time series plots of the reactor power $\widehat{P}$, the salt temperature $\widehat{T}_{c,10}$ and the delayed neutron precursors $\widehat{C}_1$ for the initial condition $\widehat{P}(t_0 = 0) = 1.1$ and different values of W.

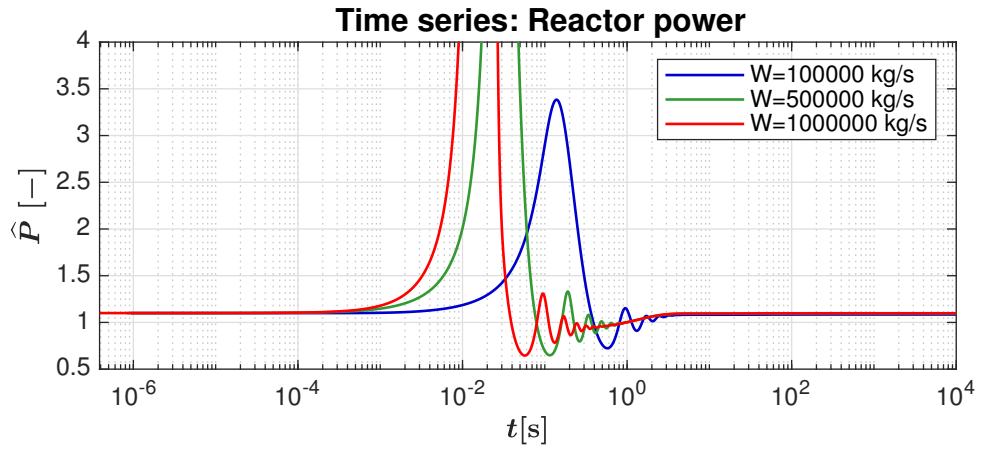

Figure 5-6: Time series plots of the reactor power $\widehat{P}$ for the initial condition $\widehat{P}(t_0 = 0) = 1.1$ and values $W \geq W_{max}$.

is $W = 0$, the temperatures in the core are that high, that they regulate the reactor power to zero. The opposite is the case for an increasing salt flow rate.

It is visible that for every peak in the temperature time series, there is a peak in the opposite direction in the power plot resulting from the negative sign of the temperature feedback. Also, one can observe that the system is inclined to oscillate for higher values of W. However, even an increase beyond the specified $W_{max} = 100\,000\,\frac{\text{kg}}{\text{s}}$ does not result in a continued periodic behaviour (see Figure 5-6). Since a higher power level in the core leads to more fission reactions and more delayed neutron precursors being produced, the time series plot of $\widehat{C}_1$ reflects the changed steady-state power levels.

The fixed-point power levels $\widehat{P}_0(W = 10\,000\,\frac{\text{kg}}{\text{s}}) = 0.89$ and $\widehat{P}_0(W = 100\,000\,\frac{\text{kg}}{\text{s}}) = 1.08$ are consistent with the respective values obtained in Figure 5-1e and verify the MatCont results.

Parameter K

According to the MatCont plot 5-1f, the power level of the fixed point increases with a higher value of the overall heat transfer coefficient K. The same behaviour can be observed in the time series plot of the reactor power $\widehat{P}$ in Figure 5-7. It is also visible that the smaller the value of K, the smaller the fixed-point power. For $K = 0$, the heat of the primary loop cannot leave through the heat exchanger any more, and the model corresponds to an adiabatic system. The reactor is 'saturated' with heat, and it cannot be fed

any more energy into the system. Therefore, the reactor power tends to zero, as can be seen in the MatCont plot.

In Figure 5-7, one can observe that the change in the reactor power sets in at $t = 0.6\,\mathrm{s}$, which corresponds to the passage time between the heat exchanger and core (cold leg transit time τ_2). For a higher value of K, more heat can be transferred to the secondary loop in the heat exchanger. The temperature $\widehat{T}_{\mathrm{he},10}$ decreases as more heat leaves the primary loop. At the same time, more energy is released in the core in order to compensate for the additional heat 'loss' in the heat exchanger, and the reactor power increases. More heat in the core leads to an increase of the core temperatures, which is visible in the corresponding plot.

The steady-state power levels $\widehat{P}_0(K = 1 \cdot 10^7\,\frac{\mathrm{kg}}{\mathrm{s}}) = 0.53$ and $\widehat{P}_0(K = 1 \cdot 10^8\,\frac{\mathrm{kg}}{\mathrm{s}}) = 2.75$ of Figure 5-7 are the same as those obtained in the MatCont plot 5-1f at these values of K.

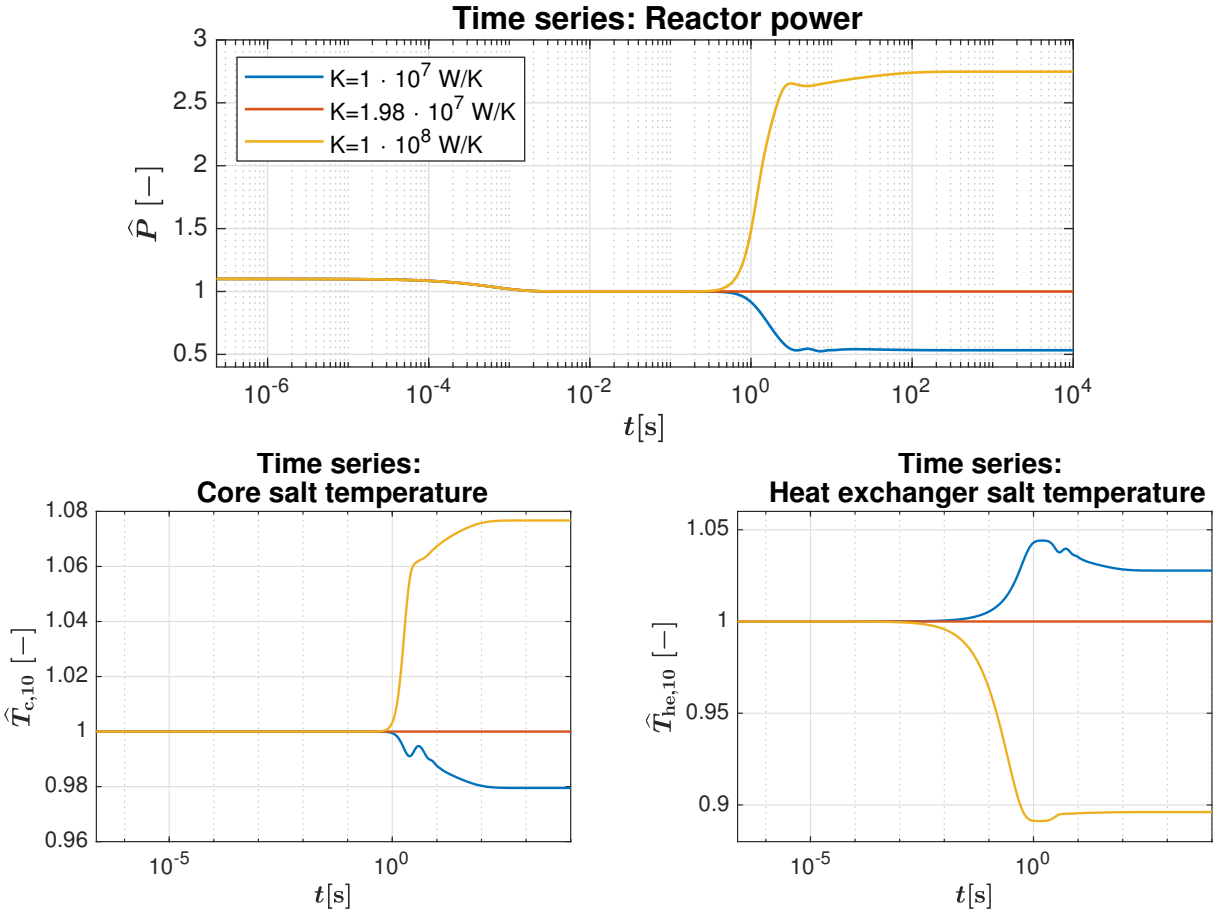

Figure 5-7: Time series plots of the reactor power $\widehat{P}$, the salt temperature in the core $\widehat{T}_{\mathrm{c},10}$ and heat exchanger $\widehat{T}_{\mathrm{he},10}$ for the initial condition $\widehat{P}(t_0 = 0) = 1.1$ and different values of K.

5.3 Linear Stability Analysis

5.3.1 Comparison Between the Linearised and Nonlinearised MSFR System of Equations

Before analysing the MSFR model by means of a linear stability criterion, the linearised system of Eqs. 4-14 to 4-19 is compared to its original nonlinear system of Eqs. 4-21 to 4-26 in order to assess the quality of the linearised version. Therefore, the time series of the reactor power and the core salt temperature are plotted for both systems and it is examined whether they yield similar results.

The comparison is conducted for different parameter sets, which are specified in the following:

Parameter set 1: all parameters as specified in Table 4-3,

Parameter set 2: $W = 100\,000\,\frac{\mathrm{kg}}{\mathrm{s}}$, other parameters as specified in Table 4-3,

Parameter set 3: $M_{\mathrm{c}} = 10\,000\,\mathrm{kg}$, other parameters as specified in Table 4-3.

Parameter set 1 comprises the given parameter list of Table 4-3. For sets 2 and 3, the parameters W and M_{c} are raised, and all the other parameters are kept at their specified values. The salt flow rate W and the mass of salt in the core M_{c} are selected because they feature in most equations of the analysed systems. They directly affect the equations for the salt temperatures and also influence the transit times τ_{c} and τ_{e}, which determine the delayed neutron precursor populations.

Figure 5-8 shows the time series plots of the reactor power $P(t)$ and the salt temperature $T_{\mathrm{c},1}(t)$ of core region 1 for the linearised and nonlinear system of equations. The results are plotted relative to the initial fixed-point values for a reactivity insertion of $\rho_{\mathrm{ex}} = 1 \cdot 10^{-3}$. The plots for the linearised system would normally describe a curve starting at zero since it only considers the deviations $\delta P(t)$ and $\delta T_{\mathrm{c},1}(t)$ from the fixed point. In order to compare the plots of the nonlinear and linearised system, the power and temperature of the latter are expressed as $P(t) = P_0 + \delta P(t)$ and $T_{\mathrm{c},1}(t) = T_{\mathrm{c},1,0} + \delta T_{\mathrm{c},1}(t)$, where P_0 and $T_{\mathrm{c},1,0}$ represent the initial fixed-point values. Thus, the graphs of both systems start at the same point.

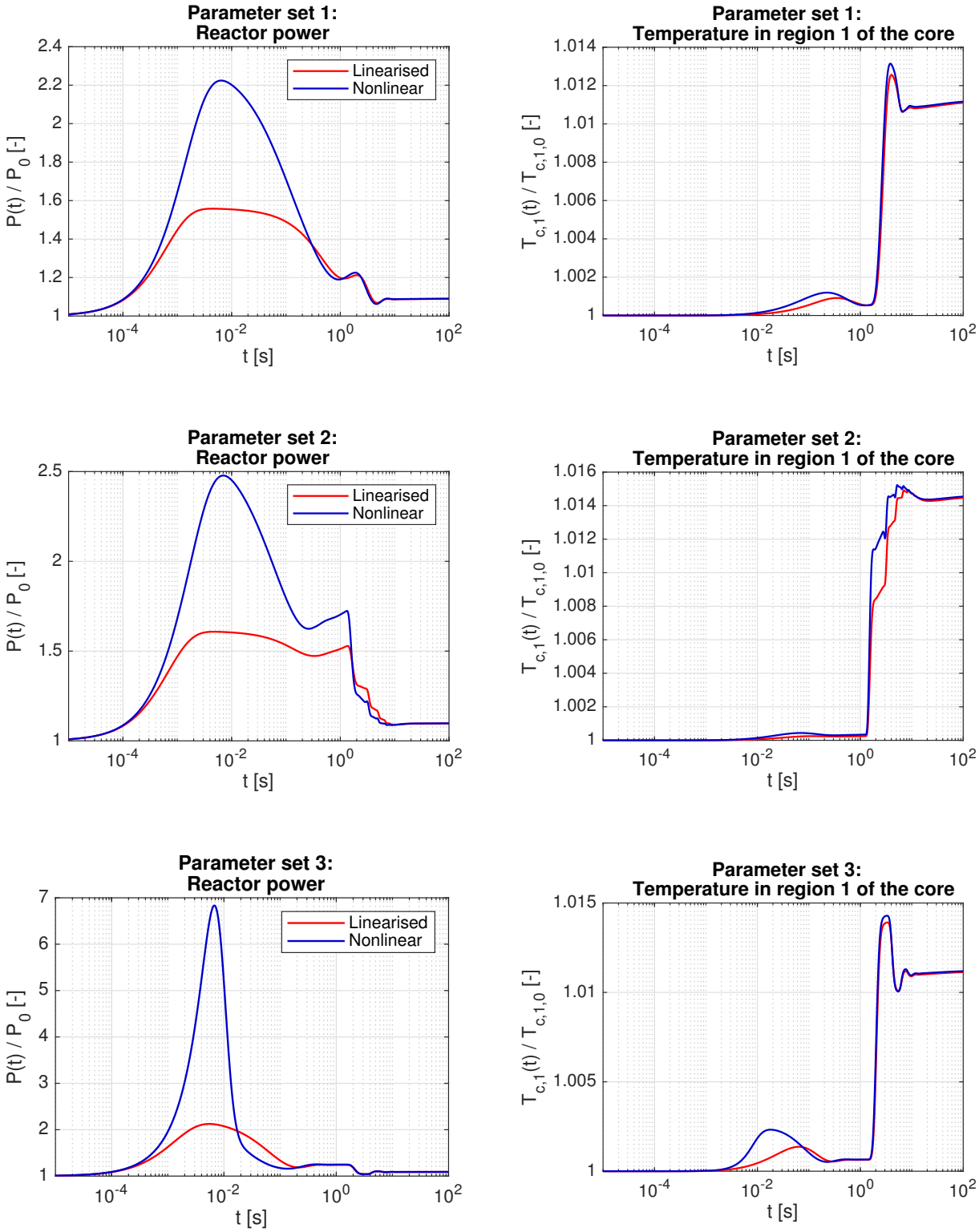

Figure 5-8: Time series plots of the reactor power $P(t)$ and the salt temperature $T_{\mathrm{c},1}(t)$ for the linearised and nonlinear system of equations of the MSFR model, considering a reactivity insertion of $\rho_{\mathrm{ex}} = 10^{-3}$.

Regarding the power plots, it is visible that the peak resulting from the external reactivity insertion is higher for the nonlinear system than for the linearised system. However, the graphs of both systems lead to the same steady-state values. The linearised system yields qualitatively the same power evolution over time as the nonlinear one. The temperature plots of both systems show approximately the same results, qualitatively and quantitatively. Only for parameter set 2, which contains an increased value of the salt flow rate, the linearised system does not reproduce every oscillation peak of the nonlinear system.

Altogether, one can conclude that the linearised equation system provides a qualitatively sufficient approximation of the nonlinear system, and it can be used to describe the dynamic behaviour of the MSFR.

5.3.2 Stability Investigations Using a Linear Criterion

In the following, a linear criterion is applied to analyse the stability of the steady-state fixed point of the MSFR model

$$\boldsymbol{X}_0 = \Big(P_0 \quad \widetilde{C}_{1,0} \dots \widetilde{C}_{8,0} \quad T_{\mathrm{c},1,0} \dots T_{\mathrm{c},N_\mathrm{c},0} \quad T_{\mathrm{he},1,0} \dots T_{\mathrm{he},N_\mathrm{he},0} \quad \dots \\ Y_{1,1,0} \dots Y_{N_\mathrm{he},8,0} \quad T_{\mathrm{cl},1,0} \dots T_{\mathrm{cl},N_\mathrm{cl},0} \quad T_{\mathrm{hl},1,0} \dots T_{\mathrm{hl},N_\mathrm{hl},0} \Big)^\top .$$

and it is checked whether the results are consistent with those of the nonlinear stability analysis. The chosen linear method examines the eigenvalues of the Jacobian matrix of the MSFR equation system in order to evaluate the stability of the associated fixed point. This approach requires the partial derivatives of the nonlinear system of Eqs. 4-21 to 4-26 without time delays for linearisation. The method is described in detail in Section 3.4.1.

The Jacobian matrix at the steady-state fixed point of the MSFR system is presented in Appendix D. The eigenvalues of the Jacobian matrix are evaluated for three different parameter sets that are defined in the previous section 5.3.1. Figure 5-9 shows the eigenvalues plotted in the complex plane for each parameter set. The first eigenvalue in each case has a strongly negative real part value and is not depicted in order to keep the graphical representation clear. All numerical values are listed in Appendix D.

As can be seen in Figure 5-9, all 69 eigenvalues (one for each state variable) have negative

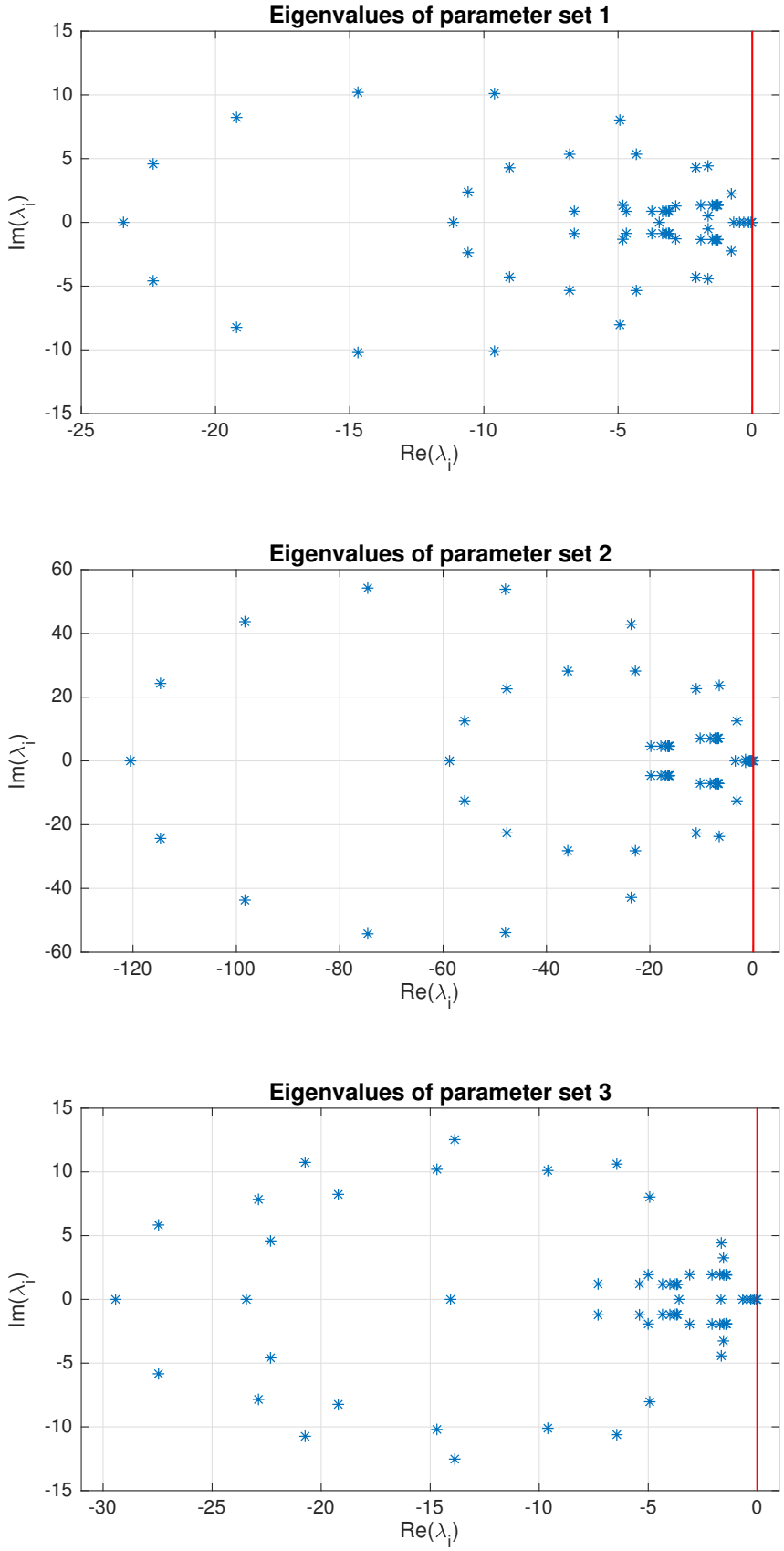

Figure 5-9: Eigenvalues of the Jacobian matrix of the MSFR model plotted in the complex plane for the specified parameter sets of Section 5.3.1.

real parts irrespective of the applied parameter sets. In the plots, some eigenvalues seem to lie close to zero on the real axis. But in fact, the largest value for each parameter set has a negative real part value of $\mathrm{Re}(\lambda_{69}) = -0.48 \ldots -0.47$ (see Table D-1 in Appendix D). With all real parts of the eigenvalues being negative, the fixed point $\boldsymbol{X}_0$ is considered to be stable for all three parameter sets. According to the Hartman-Grobman theorem, the assumption of stability for the MSFR fixed point is valid for small deflections of the state variables in a confined phase space neighbourhood.

The results of this linear stability investigation are consistent with those of the nonlinear stability analysis carried out in MatCont. Moreover, linearisation can give a qualitatively precise approximation of the original MSFR system for most parameter sets, as the previous section shows. The evaluation of the eigenvalues of the Jacobian matrix requires little preparation, time and computational performance in order to analyse a selected fixed point for a certain parameter set. It is therefore a convenient stability analysis method for spot checks regarding the investigated MSFR model. In general, however, it is not a reliable approach for making statements about the stability of a dynamical system. When the eigenvalues of the Jacobian matrix determine a fixed point to be stable or unstable, the Hartman-Grobman theorem does not specify the size of the respective sink or source in phase space. Consequently, the eigenvalue evaluation can only provide local stability information and disregards coexisting solutions.

5.4 MatCont Reliability Test Using an MSBR Model

In order to check the reliability of the MatCont software with regard to its ability and precision to determine stability boundaries, another reactor type is studied. This additional reactor design is the MSBR – a breeder reactor that was developed at the ORNL in the 1960s (see Section 2.2). It uses a graphite-moderated core, inside of which the molten fuel salt flows upwards through passages. The salt then passes its heat on to a secondary salt in the heat exchangers [39].

This reactor design is selected because its stability was investigated alongside the MSFR in the reference paper [7] that is used as the base for the stability investigations of this work. This reference article gives specific stability boundaries for the MSBR system concerning

the temperature feedback coefficient of the graphite α_{g}. Consequently, a fixed-point analysis is carried out in MatCont under the variation of the parameter α_{g} in order to test whether similar boundary values can be determined with this software.

The MSBR model adopts most equations of the MSFR system, but contains some adjustments regarding the graphite in the core. The delayed system of the MSBR has to be rewritten as an ODE system, in a procedure similar to the one explained in Sections 4.4.2 and 4.4.3. The DDE and ODE system of the MSBR, as well as their verifications and the corresponding parameter list, are presented in Appendix E.

The default value of the temperature feedback coefficient of the graphite is given as $\alpha_{\mathrm{g}} = -0.605{\cdot}10^{-5}\,\mathrm{K}^{-1}$ in the reference paper. However, the parameter source [39] quoted in that paper specifies a feedback coefficient of $\alpha_{\mathrm{g}} = +2.349 \cdot 10^{-5}\,\mathrm{K}^{-1}$. This discrepancy results from different fuel compositions that influence α_{g} [7]. The negative value of α_{g} applies for fresh fuel salt with some added erbium, whereas the positive value refers to fuel salt without erbium. The stability of the fixed point is analysed for a parameter variation of $\alpha_{\mathrm{g}} = -1 \cdot 10^{-4} \ldots 1 \cdot 10^{-4}$.

Figure 5-10 shows the MatCont plot for the relative reactor power $\widehat{P}_0(\alpha_{\mathrm{g}})$ at the steady-state fixed point as the parameter α_{g} gets varied. The black point markers denoted with 'Value 1' and 'Value 2' indicate the parameter values for α_{g} with and without erbium in the fuel salt, respectively.

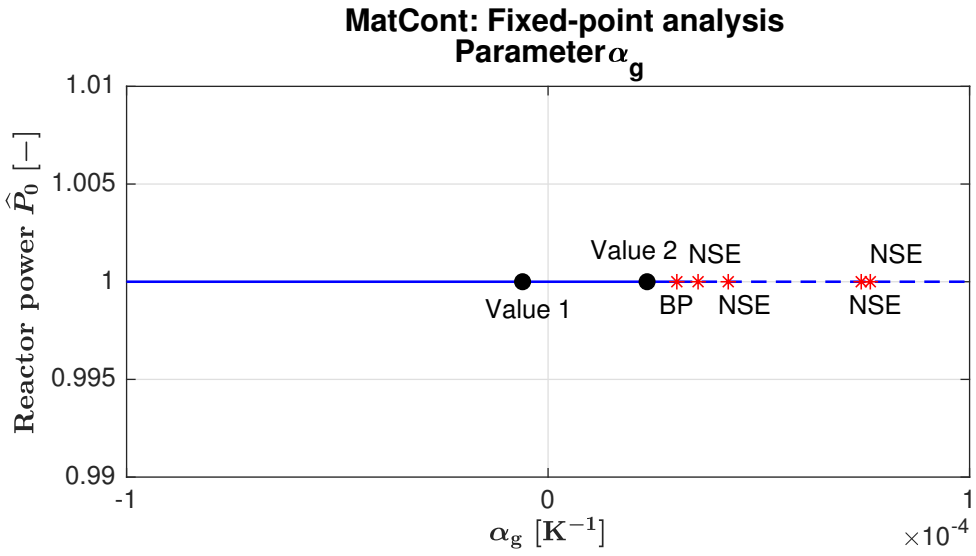

Figure 5-10: Relative reactor power $\widehat{P}_0$ of the steady-state fixed point of the MSBR as the parameter α_{g} gets varied.

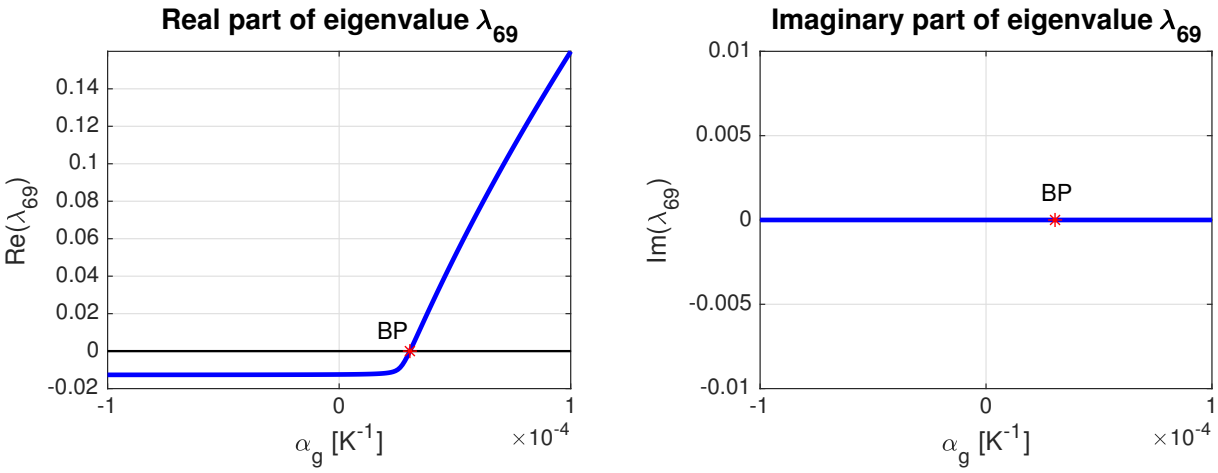

Figure 5-11: Real and imaginary part of the eigenvalue λ_{69} of the steady-state fixed point of the MSBR as the parameter α_g gets varied.

MatCont displays a branch point ('BP') and several neutral saddle equilibria ('NSE') during the parameter variation. According to the MatCont user manual, the application determines branch points by evaluating the eigenvalues of the Jacobian matrix of the analysed ODE system. In order to investigate these points, the real and imaginary part of the largest eigenvalue λ_{69} are plotted over the varied parameter α_g. This plot is depicted in Figure 5-11.

One can observe that the real part of the eigenvalue gets positive at $\alpha_{\mathrm{g,lim}} = +3.0549 \cdot 10^{-5}\,\mathrm{K}^{-1}$, which is the value, at which the branch point is found. This implies that the steady-state fixed point becomes unstable. It is also visible that the imaginary part of the largest eigenvalue is invariably equal to zero. Therefore, the Hopf conditions are not fulfilled, and the emergence of a periodic solution at the branch point can be ruled out.

With regards to the neutral saddle equilibria, the real part of λ_{69} does remain positive. However, at each point denoted as neutral saddle equilibrium, there exists a real negative eigenvalue, which sums up to zero together with the positive one. The values of α_g, at which these points are found, lie in a range above the stability boundary, and they are irrelevant for the reliability check of the MatCont software.

The influence of parameter α_g on the time evolution of the reactor power $\widehat{P}$ is shown in Figure 5-12.

For an initial deflection $\widehat{P}(t_0 = 0) = 1.1$, the reactor power returns to the fixed point $\widehat{P}_0 = 1$ as long as $\alpha_\mathrm{g} < \alpha_{\mathrm{g,lim}}$ (the plots for the first three values of α_g overlay each other). When

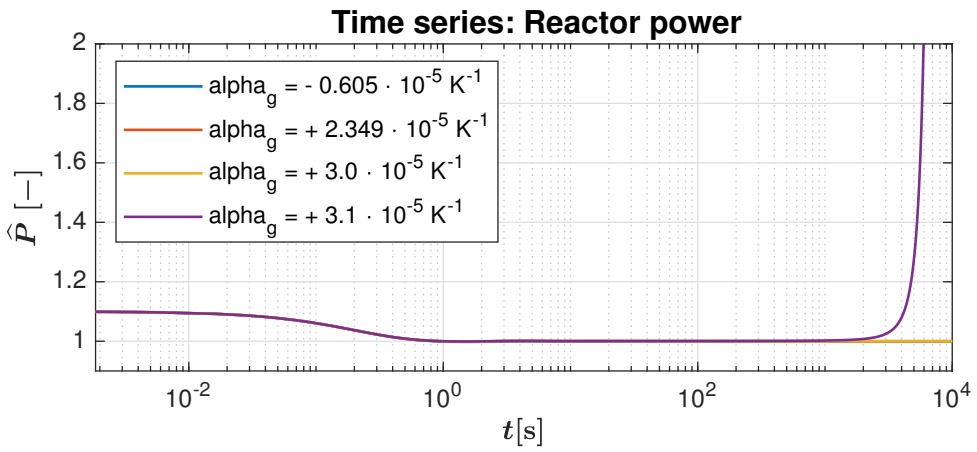

Figure 5-12: Time series plot of the reactor power $\widehat{P}$ for the initial condition $\widehat{P}(t_0 = 0) = 1.1$ and different values of α_{ex}.

α_{g} exceeds the limit value of $\alpha_{\mathrm{g,lim}}$, the power does not return to a steady state. This is consistent with the assumption that the fixed point becomes unstable at $\alpha_{\mathrm{g,lim}}$.

However, this fixed point continues to exist, since the characteristic equation $\boldsymbol{F}(\boldsymbol{X}_0; \boldsymbol{c}) = \boldsymbol{0}$ is still fulfilled. The feedback term $\alpha_{\mathrm{g}}\left(T^*_{\mathrm{g}}(t) - T^*_{\mathrm{g0}}\right)$ equals zero at the steady-state fixed point $\boldsymbol{X}_0$. This shows that α_{g} does not influence the behaviour of the state variables at that point. It can be concluded that the fixed point $\boldsymbol{X}_0$ does not disappear but its stability property changes from stable to unstable when exceeding $\alpha_{\mathrm{g,lim}}$. The specified values of the graphite feedback coefficient for fuel with and without erbium are both in the region for the stable fixed point (see 'Value 1' and 'Value 2' in Figure 5-10).

Comparing the limit value of the temperature feedback coefficient $\alpha_{\mathrm{g,lim}} = +3.0549 \cdot 10^{-5}\,\mathrm{K}^{-1}$ determined by MatCont to the value calculated in the reference paper $\alpha_{\mathrm{g,lim}} = +3.029 \cdot 10^{-5}\,\mathrm{K}^{-1}$, it is obvious that there is only a minor deviation. This might be due to some mismatching parameters, the use of a linearised approach in the reference or the influence of the numerical settings in MatCont. Altogether, one can conclude that the software MatCont has the ability and precision to determine the stability boundary of the MSBR fixed point. It therefore proves to be a reliable tool for stability analysis.

6 CONCLUSIONS AND RECOMMENDATIONS FOR FUTURE STUDIES

In this work, the stability behaviour of the Molten Salt Fast Reactor (MSFR) design was investigated by analysing a specified model. This model was adopted from a reference article by the Politecnico di Milano [7], which provided the system equations and parameter values. In order to receive a numerical representation for the analyses, the equations had to be translated into MATLAB code. The implementation was verified, as the MATLAB time series and Bode plots of the linearised version reproduced the results of the reference. Only minor deviations were found. Those differences were thought to originate from some mismatching parameters and did not alter the quality of the plots. In the next step, the model equations were adjusted to be analysed in the numerical bifurcation software MatCont.

With the help of MatCont, the steady-state fixed point of the full nonlinear MSFR system was analysed for multiple parameter variations, and it was found that it does remain stable for any of the considered modifications. Furthermore, no bifurcating solutions were detected. As a consequence, the examined MSFR model is considered a stable system, in which the transients of all state variables return to a steady state for all the analysed parameter changes. The precision of the MatCont software was checked by regarding the MSBR as an additional reactor model for which specific stability boundaries were already determined in the reference paper. A fixed-point analysis with MatCont delivered the same results and therefore confirmed that this application is a reliable tool for stability analysis.

It has to be noted that only variations of single parameter values were considered. This approach is assumed to be sufficient since the model was analysed for normal operational conditions, and accident scenarios were not studied. Regular operation implies that the parameters can deviate from their default values independently of each other, and therefore a multidimensional variation is unlikely. However, certain design data, like the transit times in the core or external loop, are related to multiple parameters, and corresponding correlations were included in the model. Changes of the inherent neutronic data were not taken into account.

Analysing the stability of the linearised system offers the advantage of requiring less effort and computational resources. The eigenvalue evaluation of the Jacobian matrix was selected as a linear stability method because it demands little preparation, and the transition to the nonlinear approach is visible (see Chapter 3). Other linear engineering tools, like the Nyquist criterion, were already analysed in the reference article. In this work, the fixed point of the MSFR model was investigated for specific parameter sets using the mentioned linear approach. It was found that this method provides results that conform with those of MatCont. Altogether, the linearisation and application of linear stability criteria is a valid method for stability spot checks under the condition of small deflections of the state variables from the fixed point. However, because linear methods cannot provide information about coexisting solutions and the size of a stable or unstable region in phase space, their use is not recommended for making statements of the system stability. For this purpose, a nonlinear analysis by means of programs like MatCont should be the preferred option.

This work analysed the MSFR design in nonlinear terms and therefore offers a complementary investigation to the linear stability considerations of [7]. Although the results of the nonlinear and linear approach were consistent in this work, it is always important to take the possibility of bifurcations, which can have catastrophic consequences, into account when analysing the stability of a system. In case of the MSFR, no such bifurcations were found, and indeed the analysed model proved to be stable within physically realistic parameter boundaries. The outcome of this work reinforces the MSFR design, which is considered a safe, sustainable and effective way of power generation, and offers a meaningful contribution to the further development of this technology.

The model adopted for the analyses in this work is low-dimensional and neglects certain aspects. Further investigations could use this study as a base and extend the existing model in several ways:

- The current model assumes one 'collective' heat exchanger although the original MSFR design plans on employing 16 identical, yet independent heat exchangers. A more detailed model should therefore treat each heat exchanger separately.

- A separate correlation for the overall heat transfer coefficient K of the heat exchanger should be included. In this work, K is modelled as a fixed parameter, al-

though in reality, it depends strongly on the temperatures of the surrounding fluids and structural material.

- The secondary and possibly tertiary loop of the MSFR plant should be included in the model since the temperature of the secondary side of the heat exchanger should not be modelled as a constant but as a state variable.
- The pressure in the reactor loop should be introduced as an additional state variable by considering the equation of momentum conservation.
- It should be investigated whether a simpler and more efficient way exists for transforming the delayed differential equations into ordinary differential equations. This could help to reduce the computational cost.

The knowledge and experience gained during this work can also be applied for stability investigations of other innovative nuclear projects, like sodium-cooled fast reactors or the Dual Fluid Reactor [40].

BIBLIOGRAPHY

[1] International Energy Agency. www.iea.org/reports/electricity-information-2019 – accessed on 18th March 2020.

[2] International Atomic Energy Agency. www.iaea.org/topics/nuclear-power-and-climate-change – accessed on 18th March 2020.

[3] van Zalka, J., Behrensa, P. The spatial extent of renewable and non-renewable power generation: A review and meta-analysis of power densities and their application in the U.S. *Energy Policy*, 123:83–91, August 2018.

[4] Generation IV International Forum. A Technology Road Map for Generation IV Nuclear Energy Systems. Technical report, US DOE Nuclear Energy Research Advisory Committee and the Generation IV International Forum, December 2002.

[5] Rosenthal, M. An account of Oak Ridge National Laboratory's thirteen nuclear reactors. Technical report, Oak Ridge National Laboratory, Oak Ridge, 2009.

[6] LeBlanc, D. Molten salt reactors: A new beginning for an old idea. *Nuclear Engineering and Design*, 240(6):1644–1656, June 2010.

[7] Guerrieri, C., Cammi, A., Luzzi, L. An approach to the MSR dynamics and stability analysis. *Progress in Nuclear Energy*, 67:56–73, August 2013.

[8] Lange, C., Hennig, D., Schulze, M., Hurtado, A. Comments on the application of bifurcation analysis in BWR. *Progress in Nuclear Energy*, 68:1–15, 2013.

[9] Haubenreich, P. N., Engel, J. R. Experience with the molten-salt reactor experiment. *Nuclear Applications and Technology*, 8(2):118–136, 1970.

[10] Whatley, M. E., McNeese, L. E., Carter, W. L., Ferris, L. M., Nicholson, E. L. Engineering development of the MSBR fuel recycle. *Nuclear Applications and Technology*, 8(2):170–178, 1970.

[11] MacPherson, H. G. The molten salt reactor adventure. *Nuclear Science and Engineering*, 90:374–380, 1985.

[12] Generation IV International Forum. Technology Roadmap Update for Generation IV Nuclear Energy Systems. Technical report, OECD Nuclear Energy Agency, January 2014.

[13] Ho, M. K. M., Yeoh, G. H., Braoudakis, G. *Molten salt reactors, Materials and processes for energy: communicating current research and technological developments*. January 2013.

[14] Luzzi, L., Marcello, V. D., Cammi, A. *Multi-Physics Approach to the Modeling and Analysis of Molten Salt Reactors*. Nova Science Publishers, New York, 2012.

[15] Yu, C., Li, X., Cai, X., Zou, C., Ma, Y., Wu, J., Han, J., Chen, J. Minor actinide incineration and Th-U breeding in a small FLiNaK molten salt fast reactor. *Annals of Nuclear Energy*, 99:335–344, January 2017.

[16] Janz, G., Allen, C., Bansal, N. *Physical Properties Data Compilations Relevant to Energy Storage: II. Molten Salts: Data on Single and Multi-Component Salt Systems*. U.S. Department of Commerce / National Bureau of Standards, New York, 1979.

[17] Zhao, Q. G., Hu, C. X., Liu, S. J., Guo, H., Wu, Y. T. The thermal conductivity of molten NaNO3, KNO3 and their mixtures. *Energy Procedia*, 143:774–779, December 2017.

[18] Sobolev, V. Database of thermophysical properties of liquid metal coolants for GEN-IV. Technical report, SCK CEN Belgian Nuclear Research Centre, Mol, November 2010.

[19] Arp, V. D., McCarty, R. D., Friend, D. G. Thermophysical Properties of Helium-4 from 0.8 to 1500 K with Pressures to 2000 MPa. Technical report, United States Department of Commerce, Technology Administration, National Institute of Standards and Technology, Washington, 1998.

[20] Kabelac, S. et al. *VDI-Wärmeatlas, 11. bearbeite und erweiterte Auflage*. VDI-Gesellschaft Verfahrenstechnik und Chemieingenieurwesen, Düsseldorf, 2013.

[21] Breeze, P. *Power Generation Technologies*. Elsevier Ltd., 2 edition, 2014.

[22] Forsberg, C., Renault, C., Brun, C. L., Merle-Lucotte, E., Ignatiev, V. Liquid salt applications and molten salt reactors. *Revue Générale Nucléaire*, April 2002.

[23] Li, Q., Tang, Z., Fu, Y., Li, Z., Wang, N. Preliminary study of the use of freeze-valves for a passive shutdown system in molten salt reactors. volume 9, 2014.

[24] Furukawa, K. et al. A road map for the realization of global-scale thorium breeding fuel cycle by single molten-fluoride flow. *Energy Conversion and Management*, 49:1832–1848, 2008.

[25] Huang, Y., Liu, W., Xiao, D., Wu, S., Zeng, Y., Qian, Y., Li, Y. Control and monitoring of tritium in molten salt reactor. *He Jishu/Nuclear Techniques*, 34:632–636, August 2011.

[26] `www.nuclear-power.net/nuclear-power-plant/nuclear-fuel/uranium/uranium-233/` – accessed on 13th January 2020.

[27] Renault, C., Delpech, S., Merle, E., Konings, R., Ignatiev, V. The molten salt reactor: R&D status and perspectives in Europe. *Proc. of the 7th European Commission Conference on Euratom Research and Training in Reactor Systems (FISA 2009)*, pages 384–399, January 2009.

[28] Merle, E., Heuer, D., Allibert, M., Brovchenko, M., Capellan, N., Ghetta, V. Launching the thorium fuel cycle with the Molten Salt Fast Reactor, May 2011.

[29] Nayfeh, A., Balachandran, B. *Applied Nonlinear Dynamics*. WILEY-VCH Verlag GmbH & Co. KGaA, Weinheim, 2004.

[30] Jackson, E. A. *Perspectives of nonlinear dynamics*. Cambridge University Press, Cambridge, 1989.

[31] Kuznetsov, Y. A. *Elements of Applied Bifurcation Theory*. Springer-Verlag, New York, 1995.

[32] Guckenheimer, J., Holmes, P. *Nonlinear Oscillations, Dynamical Systems, and Bifurcations of Vector Fields*. Springer-Verlag, New York, 1983.

[33] Perko, L. *Differential Equations and Dynamical Systems*. Springer-Verlag, New-York, 2001.

[34] March-Leuba, J., Cacuci, D. G., Pérez, R. B. Nonlinear dynamics and stability of boiling water reactors: Part 1 - qualitative analysis. *Nuclear Science and Engineering*, 93:111–123, August 1986.

[35] Lange, C., Hennig, D., Hurtado, A. A novel result in the field of nonlinear stability analysis of boiling water reactors. *International Journal of Bifurcation and Chaos*, 22, 2012.

[36] `www.nuclear-power.net/glossary/doppler-broadening/` – accessed on 22th March 2020.

[37] Fiorina, C., Cammi, A., Aufiero, M., Křepel, J. Analysis of the MSFR core neutronics adopting different neutron transport models. *Conference: 20th International Conference On Nuclear Engineering collocated with the ASME 2012 Power Conference*, August 2012.

[38] Dhooge, A., Govaerts, W., Kuznetsov, Y. A., Meijer, H. G., Sautois, B. New features of the software MatCont for bifurcation analysis of dynamical systems. *MCMDS*, 14(2):147–175, 2008.

[39] Burke, O. W. Hybrid Computer Simulation of the MSBR. Technical report, Oak Ridge National Laboratory, 1972.

[40] Huke, A., Ruprecht, G., Weißbach, D., Gottlieb, S., Hussein, A., Czerski, K. The Dual Fluid Reactor – a novel concept for a fast nuclear reactor of high efficiency. *Annals of Nuclear Energy*, pages 225–235, 2015.

[41] Rizwan-uddin. Turning points and sub- and supercritical bifurcations in a simple BWR model. *Nuclear Engineering and Design*, 236:267–283, 2006.

[42] Křepel, J. *Dynamics of Molten Salt Reactors*. Phd thesis, Czech Technical University in Prague, 2006.

ABBREVIATIONS

AHTR	Advanced High-Temperature Reactor
DDE	delayed differential equation
MSBR	Molten Salt Breeder Reactor
MSFR	Molten Salt Fast Reactor
MSR	Molten Salt Reactor
MSRE	Molten Salt Reactor Experiment
ODE	ordinary differential equation
ORNL	Oak Ridge National Laboratory
PWR	Pressurised Water Reactor
TRU	transuranic

LIST OF SYMBOLS

Symbols for stability considerations:

Latin symbols

a_i	–	Constant
$\boldsymbol{c}$	–	Control parameter vector
c_k	–	Control parameter
$c_{k,\mathrm{c}}$	–	Critical parameter value
$c_{k,0}$	–	Default parameter value
$\boldsymbol{F}$	–	Set of rules describing a dynamical system, e.g. ODE system
$\boldsymbol{J}$	–	Jacobian matrix
$\boldsymbol{p}_i$	–	Eigenvector
M	–	Generic number (cf. stability definition)
t	s	Time
t_0	s	Initial time
T	s	Oscillatory period
$\boldsymbol{u}(t)$	–	Generic solution (cf. stability definition)
$\boldsymbol{u}_0$	–	Generic fixed point (cf. stability definition)
$\boldsymbol{v}(t)$	–	Generic solution (cf. stability definition)
$\boldsymbol{x}$	–	State vector
x_i	–	State variable
$\delta\boldsymbol{x}$	–	Deviation from fixed point
$\widehat{\boldsymbol{x}}$	–	State vector relative to fixed point
$\widehat{x}_i$	–	State variable relative to its fixed-point value
$\boldsymbol{X}_j$	–	Point in phase space
$\boldsymbol{X}_0$	–	Fixed point
$X_{0,i}$	–	Fixed-point value of corresponding state variable x_i
$\boldsymbol{z}$	–	Local coordinates on Poincaré section
$\boldsymbol{Z}_j$	–	Point on Poincaré section
$\boldsymbol{Z}_0$	–	Fixed point on Poincaré section

Greek symbols

Γ_0	$-$	Periodic orbit
Γ_1, Γ_2	$-$	Generic periodic orbits (cf. stability definition)
δ	$-$	Small number (cf. stability definition)
ϵ	$-$	Small number (cf. stability definition)
ϕ_t	$-$	Flow in phase space, evolution operator
λ_i	$-$	Eigenvalue
μ_i	$-$	Eigenvalues of monodromy matrix
Σ	$-$	Poincaré section
τ	s	Generic time (cf. stability definition)

Symbols for reactor models:

Latin symbols

c	$\mathrm{J\ kg^{-1}\ K^{-1}}$	Specific heat capacity of the primary salt
c_g	$\mathrm{J\ kg^{-1}\ K^{-1}}$	Specific heat capacity of the graphite
C_j	$-$	Delayed neutron precursor population of group j in the core
$\widetilde{C}_j$	W	Rescaled delayed neutron precursor population of group j in the core
$\widetilde{C}_{j,0}$	W	Rescaled delayed neutron precursor population of group j in the core at the steady-state fixed point
$\delta\widetilde{C}_j$	W	Deviation of the rescaled delayed neutron precursor population in the core from the steady-state fixed point
$\widehat{C}_j$	$-$	Delayed neutron precursor population of group j in the core relative to its fixed-point value
f_i	$-$	Weighting factor according to a cosine distribution
K	$\mathrm{W\ K^{-1}}$	Overall heat transfer coefficient between the primary and intermediate salt in the heat exchanger
K_i	$\mathrm{W\ K^{-1}}$	Overall heat transfer coefficient between the primary and intermediate salt in region i of the heat exchanger
K_D	$-$	Doppler constant
M_c	kg	Mass of salt in the core
$M_{\mathrm{c},i}$	kg	Mass of salt in region i of the core
M_cl	kg	Mass of salt in the cold leg
$M_{\mathrm{cl},i}$	kg	Mass of salt in region i of the cold leg
M_g	kg	Mass of graphite in the core
$M_{\mathrm{g},i}$	kg	Mass of graphite in region i of the core
M_he	kg	Mass of salt in the heat exchanger
$M_{\mathrm{he},i}$	kg	Mass of salt in region i of the heat exchanger
M_hl	kg	Mass of salt in the hot leg
$M_{\mathrm{hl},i}$	kg	Mass of salt in region i of the hot leg
N	$-$	Neutron population in the core
N_0	$-$	Neutron population at the steady-state fixed point

N_{c}	$-$	Number of regions in the core
N_{cl}	$-$	Number of regions in the cold leg
N_{e}	$-$	Number of regions in the external loop
N_{he}	$-$	Number of regions in the heat exchanger
N_{hl}	$-$	Number of regions in the hot leg
P	W	Reactor power
P_0	W	Reactor power at the steady-state fixed point
δP	W	Deviation of the reactor power from the steady-state fixed point
$\widehat{P}$	$-$	Relative reactor power relative to its fixed-point value
$\widehat{P}_0$	$-$	Relative fixed-point reactor power depending on the parameter variation
P_{nom}	W	Nominal reactor power
$T_{\mathrm{c},i}$	K	Salt temperature in core region i
$T_{\mathrm{c},i,0}$	K	Salt temperature in core region i at the steady-state fixed point
$\delta T_{\mathrm{c},i}$	K	Deviation of the salt temperature in core region i from the steady-state fixed point
$\widehat{T}_{\mathrm{c},i}$	$-$	Salt temperature in core region i relative to its fixed-point value
T_{c}^*	K	Average temperature of the salt
$T_{\mathrm{c}0}^*$	K	Reference average temperature of the salt
$T_{\mathrm{cl},i}$	K	Salt temperature in region i of the cold leg
$T_{\mathrm{cl},i,0}$	K	Salt temperature in region i of the cold leg at the steady-state fixed point
$\widehat{T}_{\mathrm{cl},i}$	$-$	Salt temperature in region i of the cold leg relative to its fixed-point value
$T_{\mathrm{g},i}$	K	Temperature in region i of the graphite
T_{g}^*	K	Average temperature of the graphite
$T_{\mathrm{g}0}^*$	K	Reference average temperature of the graphite
$T_{\mathrm{he},i}$	K	Salt temperature in heat exchanger region i
$T_{\mathrm{he},i,0}$	K	Salt temperature in heat exchanger region i at the steady-state fixed point
$\delta T_{\mathrm{he},i}$	K	Deviation of the salt temperature in heat exchanger region i from the steady-state fixed point

$\widehat{T}_{\mathrm{he},i}$	$-$	Salt temperature in heat exchanger region i relative to its fixed-point value
$T_{\mathrm{hl},i}$	K	Salt temperature in region i of the hot leg
$T_{\mathrm{hl},i,0}$	K	Salt temperature in region i of the hot leg at the steady-state fixed point
$\widehat{T}_{\mathrm{hl},i}$	$-$	Salt temperature in region i of the hot leg relative to its fixed-point value
T_{ic}	K	Temperature of the intermediate salt on the secondary side of the heat exchanger
U	$\mathrm{W\ K^{-1}}$	Overall heat transfer coefficient between the primary salt and the graphite in the core
U_i	$\mathrm{W\ K^{-1}}$	Overall heat transfer coefficient between the primary salt and the graphite in region i of the core
W	$\mathrm{kg\ s^{-1}}$	Salt flow rate in the primary circuit
$Y_{i,j}$	$-$	Delayed neutron precursor population of group j in region i of the external loop
$Y_{i,j,0}$	$-$	Delayed neutron precursor population of group j in region i of the external loop at the steady-state fixed point
$\widehat{Y}_{i,j}$	$-$	Delayed neutron precursor population of group j in region i of the external loop relative to its fixed-point value

Greek symbols

α_{ex}	$\mathrm{K^{-1}}$	Density feedback coefficient of the salt
α_{f}	$\mathrm{K^{-1}}$	Temperature feedback coefficient of the salt
α_{g}	$\mathrm{K^{-1}}$	Temperature feedback coefficient of the graphite
$\alpha_{\mathrm{g,lim}}$	$\mathrm{K^{-1}}$	Limit value of the graphite temperature feedback coefficient at the stability boundary
β	$-$	Total fraction of delayed neutron precursors
β_j	$-$	Fraction of delayed neutron precursors of group j
γ_{f}	$-$	Fraction of fission power released in the fuel salt
γ_{g}	$-$	Fraction of fission power released in the graphite

λ_c	s^{-1}	Inverse of core transit time
λ_e	s^{-1}	Inverse of external loop transit time
λ_j	s^{-1}	Decay constant of delayed neutron precursors of group j
Λ	s	Mean neutron generation time
ρ_0	$-$	Reactivity contribution ensuring steady-state conditions by compensating for the circulation of delayed neutron-precursors
ρ_ex	$-$	Externally supplied reactivity contribution
ρ_t	$-$	Reactivity contribution due to temperature feedback
τ_1	s	Hot leg transit time
τ_2	s	Cold leg transit time
τ_c	s	Core transit time
τ_e	s	External loop transit time
ω	$\frac{\mathrm{rad}}{\mathrm{s}}$	Angular frequency

LIST OF FIGURES

LIST OF TABLES

A BOILING WATER REACTOR MODEL ACCORDING TO MARCH-LEUBA

The so-called March-Leuba system describes a low-dimensional model of a boiling water reactor. It was presented by March-Leuba and his colleagues at the University of Tennessee and the ORNL in 1986 [34]. The governing equations and parameter values of this system are taken from [41]. It is described by the following system of equations:

$$\frac{\mathrm{d}N(t)}{\mathrm{d}t} = \frac{\rho_\alpha(t) + DT(t) - \beta}{\Lambda} N(t) + \lambda C(t) + \frac{\rho_\alpha(t) + DT(t)}{\Lambda} \tag{A-1}$$

$$\frac{\mathrm{d}C(t)}{\mathrm{d}t} = \frac{\beta}{\Lambda} N(t) - \lambda C(t) \tag{A-2}$$

$$\frac{\mathrm{d}T(t)}{\mathrm{d}t} = a_1 N(t) - a_2 T(t) \tag{A-3}$$

$$\frac{\mathrm{d}\rho_\alpha(t)}{\mathrm{d}t} = \rho_t(t) \tag{A-4}$$

$$\frac{\mathrm{d}\rho_t(t)}{\mathrm{d}t} = -a_3 \rho_t(t) - a_4 \rho_\alpha(t) + kT(t)\ . \tag{A-5}$$

Variables $N(t)$, $C(t)$ and $T(t)$ denote the neutron concentration, delayed neutron precursor concentration and temperature in the core, and $\rho_\alpha(t)$ and $\rho_t(t)$ represent reactivity feedback contributions.

Table A-1 specifies the parameter values for the March-Leuba system. For the bifurcation analysis, parameter k gets varied and has the critical value $k_\mathrm{c} = -3.7036 \cdot 10^{-3}\,\mathrm{K^{-1}s^{-2}}$ [41].

Table A-1: Parametric data for the March-Leuba system [41]

Symbol	Unit	Value
a_1	s^{-1}	25.04
a_2	$\mathrm{K}^{-1}\mathrm{s}^{-1}$	0.23
a_3	s^{-2}	2.25
a_4	s^{-2}	6.82
D	K^{-1}	$-2.52 \cdot 10^{-5}$
β	$-$	0.0056
Λ	s	$4 \cdot 10^{-5}$
λ	s^{-1}	0.08

B APPLICATION OF FLOQUET THEORY TO PERIODIC SOLUTIONS

This appendix describes the application of the Floquet theory to a periodic solution of a generic dynamical system.

The periodic solution $\boldsymbol{x}(t) = \boldsymbol{\gamma}(t) \in \mathbb{R}^{\mathrm{n}}$, associated with the limit cycle Γ_0 of an autonomous dynamical system $\dot{\boldsymbol{x}} = \boldsymbol{F}(\boldsymbol{x}; \boldsymbol{c})$, has the minimal period T. The system can be linearised about the periodic solution $\boldsymbol{\gamma}(t)$ by using a first-order Taylor series approximation correspondingly to Eq. 3-8. Applying a small disturbance $\delta\boldsymbol{\gamma}(t)$ to the linearised system yields [29]

$$\delta\dot{\boldsymbol{\gamma}} = D_{\boldsymbol{x}}\boldsymbol{F}(\boldsymbol{\gamma}(t); \boldsymbol{c})\delta\boldsymbol{\gamma} = \boldsymbol{A}(t; \boldsymbol{c})\delta\boldsymbol{\gamma} \tag{B-1}$$

where $A(t; \boldsymbol{c})$ is a time-continuous, T-periodic matrix, containing the partial derivatives of $\boldsymbol{F}$ at $\boldsymbol{\gamma}(t)$ [32].

Eq. B-1 has the form of an n-dimensional, nonautonomous linear system, which has n linearly independent solutions $\boldsymbol{\phi}_i(t)$ [33]. The fundamental matrix solution $\boldsymbol{\Phi}(t)$ of system B-1 contains all linearly independent solution vectors:

$$\boldsymbol{\Phi}(t) = \begin{pmatrix} \boldsymbol{\phi}_1(t) & \boldsymbol{\phi}_2(t) & \cdots & \boldsymbol{\phi}_n(t) \end{pmatrix} . \tag{B-2}$$

The solution of system B-1 can then be given as the linear combination

$$\delta\boldsymbol{\gamma}(t) = \boldsymbol{\Phi}(t)\,\boldsymbol{\Phi}^{-1}(0)\delta\boldsymbol{\gamma}_0 \tag{B-3}$$

for the initial condition $\delta\boldsymbol{\gamma}(t = 0) = \delta\boldsymbol{\gamma}_0$ [33].

Floquet's Theorem says that, for $\boldsymbol{A}(t; \boldsymbol{c})$ being a time-continuous, T-periodic matrix, the fundamental matrix solution can be expressed as

$$\boldsymbol{\Phi}(t) = \boldsymbol{Q}(t)\mathrm{e}^{\boldsymbol{B}t} \tag{B-4}$$

with $\boldsymbol{Q}(t)$ being a T-periodic matrix such that $\boldsymbol{Q}(t) = \boldsymbol{Q}(t + T)$, and $\boldsymbol{B}$ being a constant

matrix [33]. Choosing the initial condition $\boldsymbol{\Phi}(0) = \boldsymbol{I}$, Eq. B-4 gives $\boldsymbol{Q}(0) = \boldsymbol{I}$. Thus, $\boldsymbol{\Phi}(T)$ can be calculated as

$$\boldsymbol{\Phi}(T) = \boldsymbol{Q}(T)\mathrm{e}^{\boldsymbol{B}T} = \boldsymbol{Q}(0)\mathrm{e}^{\boldsymbol{B}T} = \mathrm{e}^{\boldsymbol{B}T} \tag{B-5}$$

where the constant matrix $\mathrm{e}^{\boldsymbol{B}T}$ is called the monodromy matrix [33].

As the fundamental matrix $\boldsymbol{\Phi}(t)$ contains all n linearly independent solutions $\boldsymbol{\phi}_i(t)$ of system B-1, the fundamental matrix solution $\boldsymbol{\Phi}(t+T)$ must be a linear combination of $\boldsymbol{\phi}_i(t)$ [29]. This linear combination uses the entries of the monodromy matrix as vector coefficients and is specified by the following equation:

$$\boldsymbol{\Phi}(t+T) = \boldsymbol{\Phi}(t)\mathrm{e}^{\boldsymbol{B}T} = \boldsymbol{\Phi}(t)\,\boldsymbol{\Phi}(T)\ . \tag{B-6}$$

With $\boldsymbol{\Phi}(\boldsymbol{0}) = \boldsymbol{I}$, the general solution B-3 of system B-1 at the time $t+T$ eventually equals

$$\delta\boldsymbol{\gamma}(t+T) = \boldsymbol{\Phi}(t+T)\delta\boldsymbol{\gamma}_0 = \boldsymbol{\Phi}(t)\mathrm{e}^{\boldsymbol{B}T}\delta\boldsymbol{\gamma}_0 = \boldsymbol{\Phi}(t)\,\boldsymbol{\Phi}(T)\delta\boldsymbol{\gamma}_0\ . \tag{B-7}$$

It is therefore evident that the monodromy matrix is a valuable indicator of the temporal behaviour of periodic solutions.

C MATCONT IMPLEMENTATION OF THE NONLINEAR MSFR SYSTEM

C.1 Adapted Nonlinear System of Ordinary Differential Equations

The nonlinear ODE system (Eqs. 4-45 to 4-55) of the presented MSFR model is transformed such that the system variables $x_i(t) \in \boldsymbol{x}(t)$ can be expressed relative to the fixed-point values $X_{0,i} \in \boldsymbol{X}_0$, as described in Section 5.2.1.

This is done by applying the following substitution, which uses the newly introduced relative variables $\widehat{x}_i(t)$:

$$x_i(t) = X_{0,i}\, \widehat{x}_i(t)\ . \tag{C-1}$$

Thus, a generic dynamical system can be transformed as

$$\dot{\boldsymbol{x}} = \boldsymbol{F}(\boldsymbol{x}; \boldsymbol{c}) \tag{C-2}$$

$$\boldsymbol{X}_0 \circ \dot{\widehat{\boldsymbol{x}}} = \boldsymbol{F}(\boldsymbol{X}_0 \circ \widehat{\boldsymbol{x}}; \boldsymbol{c}) \tag{C-3}$$

$$\dot{\widehat{\boldsymbol{x}}} = \boldsymbol{F}(\boldsymbol{X}_0 \circ \widehat{\boldsymbol{x}}; \boldsymbol{c}) \oslash \boldsymbol{X}_0\ . \tag{C-4}$$

Here, the operator $\circ$ denotes the element-wise product with $\boldsymbol{X}_0 \circ \widehat{\boldsymbol{x}} = X_{0,i}\ \widehat{x}_i$, and the operator $\oslash$ symbolises the element-wise division with $\boldsymbol{F} \oslash \boldsymbol{X}_0 = \frac{F_i}{X_{0,i}}$.

The MSFR system is adjusted according to Eq. C-4. This yields the following system:

$$\frac{\mathrm{d}\widehat{P}(t)}{\mathrm{d}t} = \frac{\dfrac{\rho_0 + \rho_\mathrm{t}(t) + \rho_\mathrm{ex}(t) - \beta}{\Lambda} P_0\, \widehat{P}(t) + \displaystyle\sum_{j=1}^{8} \lambda_j\, C_{j,0}\, \widehat{C}_j(t)}{P_0} \tag{C-5}$$

$$\text{with } \rho_\mathrm{t}(t) = \alpha_\mathrm{ex}\Big(T_\mathrm{c}^*(t) - T_\mathrm{c0}^*\Big) + K_\mathrm{D} \ln\left(\frac{T_\mathrm{c}^*(t)}{T_\mathrm{c0}^*}\right)$$

$$\text{and } T_c^*(t) = \frac{1}{N_\mathrm{c}} \sum_{i=1}^{N_\mathrm{c}} T_{c,i,0}\, \widehat{T}_{c,i}(t)$$

$$\frac{\mathrm{d}\widehat{C}_j(t)}{\mathrm{d}t} = \frac{\dfrac{\beta_j}{\Lambda} P_0\, \widehat{P}(t) - (\lambda_j + \lambda_\mathrm{c})\, C_{j,0}\, \widehat{C}_j(t) + \lambda_\mathrm{c}\, Y_{N_\mathrm{e},j,0}\, \widehat{Y}_{N_\mathrm{e},j}(t)}{C_{j,0}} \tag{C-6}$$

for $j = 1 \ldots 8$

$$\frac{\mathrm{d}\widehat{T}_{\mathrm{c},1}(t)}{\mathrm{d}t} = \frac{\dfrac{f_1}{M_{\mathrm{c},1}\,c} P_0\,\widehat{P}(t) + \dfrac{W}{M_{\mathrm{c},1}}\Big(T_{\mathrm{cl},N_{\mathrm{cl}},0}\,\widehat{T}_{\mathrm{cl},N_{\mathrm{cl}}}(t) - T_{\mathrm{c},1,0}\,\widehat{T}_{\mathrm{c},1}(t)\Big)}{T_{\mathrm{c},1,0}} \tag{C-7}$$

$$\frac{\mathrm{d}\widehat{T}_{\mathrm{c},i}(t)}{\mathrm{d}t} = \frac{\dfrac{f_i}{M_{\mathrm{c},i}\,c} P_0\,\widehat{P}(t) + \dfrac{W}{M_{\mathrm{c},i}}\Big(T_{c,i-1,0}\,\widehat{T}_{\mathrm{c},i-1}(t) - T_{c,i,0}\,\widehat{T}_{\mathrm{c},i}(t)\Big)}{T_{c,i,0}} \tag{C-8}$$

for $i = 2, \ldots, N_{\mathrm{c}}$

$$\frac{\mathrm{d}\widehat{T}_{\mathrm{he},1}(t)}{\mathrm{d}t} = \frac{\dfrac{W}{M_{\mathrm{he},1}}\Big(T_{\mathrm{hl},N_{\mathrm{hl}},0}\,\widehat{T}_{\mathrm{hl},N_{\mathrm{hl}}}(t) - T_{\mathrm{he},1,0}\,\widehat{T}_{\mathrm{he},1}(t)\Big) + \dfrac{K_1}{M_{\mathrm{he},1}\,c}\Big(T_{\mathrm{ic}} - T_{\mathrm{he},1,0}\,\widehat{T}_{\mathrm{he},1}(t)\Big)}{T_{\mathrm{he},1,0}} \tag{C-9}$$

$$\frac{\mathrm{d}\widehat{T}_{\mathrm{he},i}(t)}{\mathrm{d}t} = \frac{\dfrac{W}{M_{\mathrm{he},i}}\Big(T_{\mathrm{he},i-1,0}\,\widehat{T}_{\mathrm{he},i-1}(t) - T_{\mathrm{he},i,0}\,\widehat{T}_{\mathrm{he},i}(t)\Big) + \dfrac{K_i}{M_{\mathrm{he},i}\,c}\Big(\widehat{T}_{\mathrm{ic}} - T_{\mathrm{he},i,0}\,\widehat{T}_{\mathrm{he},i}(t)\Big)}{T_{\mathrm{he},i,0}} \tag{C-10}$$

for $i = 2, \ldots, N_{\mathrm{he}}$.

$$\frac{\mathrm{d}\widehat{Y}_{1,j}(t)}{\mathrm{d}t} = \frac{\lambda_{\mathrm{e}}\,N_{\mathrm{e}}\,C_{j,0}\,\widehat{C}_j(t) - \lambda_j\,Y_{1,j,0}\,\widehat{Y}_{1,j}(t) - \lambda_{\mathrm{e}}\,N_{\mathrm{e}}\,Y_{1,j,0}\,\widehat{Y}_{1,j}(t)}{Y_{1,j,0}}$$

for $j = 1 \ldots 8$

$$\frac{\mathrm{d}\widehat{Y}_{i,j}(t)}{\mathrm{d}t} = \frac{\lambda_{\mathrm{e}}\,N_{\mathrm{e}}\,Y_{i-1,j,0}\,\widehat{Y}_{i-1,j}(t) - \lambda_j\,Y_{i,j,0}\,\widehat{Y}_{i,j}(t) - \lambda_{\mathrm{e}}\,N_{\mathrm{e}}\,Y_{i,j,0}\,\widehat{Y}_{i,j}(t)}{Y_{i,j,0}} \tag{C-11}$$

for $i = 2 \ldots N_{\mathrm{e}}$ and $j = 1 \ldots 8$

$$\frac{\mathrm{d}\widehat{T}_{\mathrm{cl},1}(t)}{\mathrm{d}t} = \frac{\dfrac{W}{M_{\mathrm{cl},1}}\Big(T_{\mathrm{he},N_{\mathrm{he}},0}\,\widehat{T}_{\mathrm{he},N_{\mathrm{he}}}(t) - T_{\mathrm{cl},1,0}\,\widehat{T}_{\mathrm{cl},1}(t)\Big)}{T_{\mathrm{cl},1,0}} \tag{C-12}$$

$$\frac{\mathrm{d}\widehat{T}_{\mathrm{cl},i}(t)}{\mathrm{d}t} = \frac{\dfrac{W}{M_{\mathrm{cl},i}}\Big(T_{\mathrm{cl},i-1,0}\,\widehat{T}_{\mathrm{cl},i-1}(t) - T_{\mathrm{cl},i,0}\,\widehat{T}_{\mathrm{cl},i}(t)\Big)}{T_{\mathrm{cl},i,0}} \tag{C-13}$$

for $i = 2 \ldots N_{\mathrm{cl}}$

$$\frac{\mathrm{d}\widehat{T}_{\mathrm{hl},1}(t)}{\mathrm{d}t} = \frac{\dfrac{W}{M_{\mathrm{hl},1}}\Big(T_{\mathrm{c},N_{\mathrm{c}},0}\,\widehat{T}_{\mathrm{c},N_{\mathrm{c}}}(t) - T_{\mathrm{hl},1,0}\,T_{\mathrm{hl},1}(t)\Big)}{T_{\mathrm{hl},1,0}} \tag{C-14}$$

$$\frac{\mathrm{d}\widehat{T}_{\mathrm{hl},i}(t)}{\mathrm{d}t} = \frac{\dfrac{W}{M_{\mathrm{hl},i}}\Big(T_{\mathrm{hl},i-1,0}\,\widehat{T}_{\mathrm{hl},i-1}(t) - T_{\mathrm{hl},i,0}\,\widehat{T}_{\mathrm{hl},i}(t)\Big)}{T_{\mathrm{hl},i,0}} \tag{C-15}$$

for $i = 2 \dots N_{\mathrm{hl}}$

The transformed version of the rescaled delayed neutron precursor population $\widetilde{C}_j(t)$ (see Eqs. 4-7 and 4-8) is denoted as $\widehat{C}_j(t)$ instead of $\widehat{\widetilde{C}}_j(t)$ for reasons of simplicity. The corresponding fixed-point value is expressed as $C_{j,0}$ instead of $\widetilde{C}_{j,0}$.

Table C-1 lists the fixed-point values of all system variables. The value of the intermediate salt temperature equals $T_{\mathrm{ic}} = 806.4\,\mathrm{K}$ when solving the equation system at this point.

Table C-1: Fixed-point values of the system variables of equation system C-15 to C-15

Symbol	Unit	Value
P_0	W	3000000000.00000
$C_{1,0}$	W	25628577880240.7
$C_{2,0}$	W	22742501066974.0
$C_{3,0}$	W	13353003196622.3
$C_{4,0}$	W	6935328054496.97
$C_{5,0}$	W	5331227674892.07
$C_{6,0}$	W	402239560949.893
$C_{7,0}$	W	272960513819.274
$C_{8,0}$	W	30320996577.2117
$T_{\mathrm{c},1,0}$	K	920.844625951690
$T_{\mathrm{c},2,0}$	K	927.892890512671
$T_{\mathrm{c},3,0}$	K	938.870819939666
$T_{\mathrm{c},4,0}$	K	952.703818012627
$T_{\mathrm{c},5,0}$	K	968.037814500009
$T_{\mathrm{c},6,0}$	K	983.371810987391
$T_{\mathrm{c},7,0}$	K	997.204809060352
$T_{\mathrm{c},8,0}$	K	1008.18273848735
$T_{\mathrm{c},9,0}$	K	1015.23100304833
$T_{\mathrm{c},10,0}$	K	1017.65966949992
$T_{\mathrm{he},1,0}$	K	1004.67268722248
$T_{\mathrm{he},2,0}$	K	992.484069733814

Symbol	Unit	Value
$T_{\mathrm{he},3,0}$	K	981.044738169991
$T_{\mathrm{he},4,0}$	K	970.308630752662
$T_{\mathrm{he},5,0}$	K	960.232517316022
$T_{\mathrm{he},6,0}$	K	950.775825235597
$T_{\mathrm{he},7,0}$	K	941.900476057930
$T_{\mathrm{he},8,0}$	K	933.570732173325
$T_{\mathrm{he},9,0}$	K	925.753052914269
$T_{\mathrm{he},10,0}$	K	918.415959500098
$T_{\mathrm{cl},1,0}$	K	918.415959500098
$T_{\mathrm{cl},2,0}$	K	918.415959500098
$T_{\mathrm{cl},3,0}$	K	918.415959500098
$T_{\mathrm{cl},4,0}$	K	918.415959500098
$T_{\mathrm{hl},1,0}$	K	1017.65966949992
$T_{\mathrm{hl},2,0}$	K	1017.65966949992
$T_{\mathrm{hl},3,0}$	K	1017.65966949992
$T_{\mathrm{hl},4,0}$	K	1017.65966949992
$Y_{1,1,0}$	W	25473349655775.8
$Y_{1,2,0}$	W	22433009657486.9
$Y_{1,3,0}$	W	13081961310715.9
$Y_{1,4,0}$	W	6513038895133.73
$Y_{1,5,0}$	W	4664904393574.82
$Y_{1,6,0}$	W	303539800552.681
$Y_{1,7,0}$	W	151686865139.914
$Y_{1,8,0}$	W	11084261223.6197
$Y_{2,1,0}$	W	25319061624004.5
$Y_{2,2,0}$	W	22127729962985.1
$Y_{2,3,0}$	W	12816421086333.4
$Y_{2,4,0}$	W	6116462742093.26
$Y_{2,5,0}$	W	4081861501372.53
$Y_{2,6,0}$	W	229058549840.251

Symbol	Unit	Value
$Y_{2,7,0}$	W	84293895604.2865
$Y_{2,8,0}$	W	4052005565.20552
$Y_{3,1,0}$	W	25165708090329.1
$Y_{3,2,0}$	W	21826604668329.6
$Y_{3,3,0}$	W	12556270849666.9
$Y_{3,4,0}$	W	5744033941416.66
$Y_{3,5,0}$	W	3571690202126.31
$Y_{3,6,0}$	W	172853178263.232
$Y_{3,7,0}$	W	46842953934.0297
$Y_{3,8,0}$	W	1481266885.47085
$Y_{4,1,0}$	W	25013283394643.0
$Y_{4,2,0}$	W	21529577238355.0
$Y_{4,3,0}$	W	12301401193685.2
$Y_{4,4,0}$	W	5394282171145.04
$Y_{4,5,0}$	W	3125282642655.94
$Y_{4,6,0}$	W	130439231613.657
$Y_{4,7,0}$	W	26031094156.1710
$Y_{4,8,0}$	W	541497673.358016

C.2 MatCont Settings

Tables C-2 and C-3 contain the MatCont settings used for the fixed-point analysis of the MSFR system.

Table C-2: MatCont settings for the MSFR fixed-point analysis

Setting	Value
Starter window	
Initial Values	1
Parameter Values	see Table 5-1
Branching	yes
Hopf bifurcation	yes
Limit point bifurcation	yes
Calculate eigenvalues	yes
Integrator window	
InitStepsize	see Table C-3
MinStepsize	see Table C-3
MaxStepsize	see Table C-3
MaxNewtonIters	3
MaxCorrIters	10
MaxTestIters	10
VarTolerance	$1\mathrm{e}-06$
FunTolerance	$1\mathrm{e}-06$
TestTolerance	$1\mathrm{e}-05$
Adapt	3
MaxNumPoints	1000
CheckClosed	50
Jacobian Increment	$1\mathrm{e}-05$

Table C-3: Step size settings for the MSFR fixed-point analysis

Parameter	InitStepsize	MinStepsize	MaxStepsize
α_{ex}	$1\mathrm{e}-08$	$1\mathrm{e}-10$	$1\mathrm{e}-06$
K_{D}	$1\mathrm{e}-06$	$1\mathrm{e}-07$	0.001
M_{c}	10	1	100
M_{he}	10	1	100
W	10	1	100
K	$10\,000$	1000	$100\,000$
M_{cl}	10	1	100
M_{hl}	10	1	100

D JACOBIAN MATRIX OF THE MSFR SYSTEM

The Jacobian matrix at the steady-state fixed point of the MSFR system is presented in Eq. D-1 on the following pages. Since the Jacobian matrix has the dimension 69×69, not all entries for the discretised variables $\widetilde{C}_j(t)$, $T_{\mathrm{c},i}(t)$, $T_{\mathrm{he},i}(t)$, $Y_{i,j}(t)$, $T_{\mathrm{cl},i}(t)$ and $T_{\mathrm{hl},i}(t)$ are included in the representation.

Table D-1 contains the eigenvalues of the Jacobian matrix for the specified parameter sets of Section 5.3.1.

$$
\boldsymbol{J}(\boldsymbol{X}_0;\boldsymbol{c}) = \begin{pmatrix}
\frac{\rho_0-\beta}{\Lambda} & \lambda_1 & \cdots & \lambda_8 & \frac{P_0}{\Lambda N_\mathrm{c}}(\alpha_\mathrm{ex}+\frac{K_\mathrm{D}}{T^*_{\mathrm{c}0}}) & \cdots & \frac{P_0}{\Lambda N_\mathrm{c}}(\alpha_\mathrm{ex}+\frac{K_\mathrm{D}}{T^*_{\mathrm{c}0}}) & 0 & \cdots & 0 & \\
\frac{\beta_1}{\Lambda} & -(\lambda_1+\lambda_c) & \cdots & 0 & 0 & \cdots & 0 & 0 & \cdots & 0 & \\
\vdots & \vdots & \ddots & \vdots & \vdots & \ddots & \vdots & \vdots & \ddots & \vdots & \\
\frac{\beta_8}{\Lambda} & 0 & \cdots & -(\lambda_8+\lambda_c) & 0 & \cdots & 0 & 0 & \cdots & 0 & \\
\frac{f_1}{M_{\mathrm{c},1}\,c} & 0 & \cdots & 0 & -\frac{W}{M_{\mathrm{c},1}} & \cdots & 0 & 0 & \cdots & 0 & \\
\vdots & \vdots & \ddots & \vdots & \vdots & \ddots & \vdots & \vdots & \ddots & \vdots & \\
\frac{f_{10}}{M_{\mathrm{c},10}\,c} & 0 & \cdots & 0 & 0 & \cdots\ \frac{W}{M_{\mathrm{c},1}} & -\frac{W}{M_{\mathrm{c},10}} & 0 & \cdots & 0 & \\
0 & 0 & \cdots & 0 & 0 & \cdots & 0 & -(\frac{W}{M_{\mathrm{he},1}}+\frac{K_1}{M_{\mathrm{he},1}\,c}) & \cdots & 0 & \\
\vdots & \vdots & \ddots & \vdots & \vdots & \ddots & \vdots & \vdots & \ddots & \vdots & \\
0 & 0 & \cdots & 0 & 0 & \cdots & 0 & 0 \quad\cdots\ \frac{W}{M_{\mathrm{he},10}} & -(\frac{W}{M_{\mathrm{he},10}}+\frac{K_{10}}{M_{\mathrm{he},10}\,c}) & \cdots \\
0 & 4\lambda_\mathrm{e} & \cdots & 0 & 0 & \cdots & 0 & 0 & \cdots & 0 & \\
\vdots & \vdots & \vdots & \vdots & \vdots & \vdots & \vdots & \vdots & \vdots & \vdots & \\
0 & 0 & \cdots & 0 & 0 & \cdots & 0 & 0 & \cdots & 0 & \\
0 & 0 & \cdots & 0 & 0 & \cdots & 0 & 0 & \cdots & \frac{W}{M_{\mathrm{cl},1}} & \\
\vdots & \vdots & \ddots & \vdots & \vdots & \ddots & \vdots & \vdots & \ddots & \vdots & \\
0 & 0 & \cdots & 0 & 0 & \cdots & 0 & 0 & \cdots & 0 & \\
0 & 0 & \cdots & 0 & 0 & \cdots & \frac{W}{M_{\mathrm{hl},1}} & 0 & \cdots & 0 & \\
\vdots & \vdots & \ddots & \vdots & \vdots & \ddots & \vdots & \vdots & \ddots & \vdots & \\
0 & 0 & \cdots & 0 & 0 & \cdots & 0 & 0 & \cdots & 0 &
\end{pmatrix}
$$

$$
\begin{pmatrix}
0 & \cdots & 0 & 0 & \cdots & 0 & 0 & \cdots & 0 \\
0 & \cdots & \lambda_c & 0 & \cdots & 0 & 0 & \cdots & 0 \\
\vdots & \vdots & \vdots & \vdots & \ddots & \vdots & \vdots & \ddots & \vdots \\
0 & \cdots & \lambda_c & 0 & \cdots & 0 & 0 & \cdots & 0 \\
0 & \cdots & 0 & 0 & \cdots & \frac{W}{M_{\mathrm{c},1}} & 0 & \cdots & 0 \\
\vdots & \vdots & \vdots & \vdots & \ddots & \vdots & \vdots & \ddots & \vdots \\
0 & \cdots & 0 & 0 & \cdots & 0 & 0 & \cdots & 0 \\
0 & \cdots & 0 & 0 & \cdots & 0 & 0 & \cdots & \frac{W}{M_{\mathrm{he},1}} \\
\vdots & \vdots & \vdots & \vdots & \ddots & \vdots & \vdots & \ddots & \vdots \\
0 & \cdots & 0 & 0 & \cdots & 0 & 0 & \cdots & 0 \\
-(\lambda_j + 4\lambda_{\mathrm{e}}) & \cdots & 0 & 0 & \cdots & 0 & 0 & \cdots & 0 \\
\vdots & \vdots & \vdots & \vdots & \vdots & \vdots & \vdots & \vdots & \vdots \\
0 & \cdots\ 4\lambda_{\mathrm{e}} & -(\lambda_j + 4\lambda_{\mathrm{e}}) & 0 & \cdots & 0 & 0 & \cdots & 0 \\
0 & \cdots & 0 & -\frac{W}{M_{\mathrm{cl},1}} & \cdots & 0 & 0 & \cdots & 0 \\
\vdots & \vdots & \vdots & \vdots & \ddots & \vdots & \vdots & \ddots & \vdots \\
0 & \cdots & 0 & 0 & \cdots\ \frac{W}{M_{\mathrm{cl},4}} & -\frac{W}{M_{\mathrm{cl},4}} & 0 & \cdots & 0 \\
0 & \cdots & 0 & 0 & \cdots & 0 & -\frac{W}{M_{\mathrm{hl},1}} & \cdots & 0 \\
\vdots & \vdots & \vdots & \vdots & \ddots & \vdots & \vdots & \ddots & \vdots \\
0 & \cdots & 0 & 0 & \cdots & 0 & 0 & \cdots\ \frac{W}{M_{\mathrm{hl},4}} & -\frac{W}{M_{\mathrm{hl},4}}
\end{pmatrix}
\cdots \tag{D-1}
$$

Table D-1: Eigenvalues of the Jacobian matrix of the MSFR model for the parameter sets of Section 5.3.1

Parameter set 1		**Parameter set 2**		**Parameter set 3**	
Re(λ_i)	Im(λ_i)	Re(λ_i)	Im(λ_i)	Re(λ_i)	Im(λ_i)
-1590.82	0.00	-1459.06	0.00	-735.53	0.00
-23.43	0.00	-120.49	0.00	-29.43	0.00
-22.32	4.59	-114.68	24.31	-27.46	5.84
-22.32	-4.59	-114.68	-24.31	-27.46	-5.84
-19.21	8.23	-98.33	43.68	-22.87	7.84
-19.21	-8.23	-98.33	-43.68	-22.87	-7.84
-14.69	10.20	-74.58	54.21	-20.73	10.74
-14.69	-10.20	-74.58	-54.21	-20.73	-10.74
-9.60	10.11	-47.94	53.84	-13.87	12.53
-9.60	-10.11	-47.94	-53.84	-13.87	-12.53
-11.14	0.00	-58.76	0.00	-23.43	0.00
-10.59	2.38	-55.84	12.53	-22.32	4.59
-10.59	-2.38	-55.84	-12.53	-22.32	-4.59
-9.04	4.28	-47.67	22.59	-19.21	8.23
-9.04	-4.28	-47.67	-22.59	-19.21	-8.23
-6.80	5.34	-35.88	28.18	-14.07	0.00
-6.80	-5.34	-35.88	-28.18	-6.44	10.61
-4.93	8.03	-23.61	42.87	-6.44	-10.61
-4.93	-8.03	-23.61	-42.87	-14.69	10.20
-4.32	5.35	-22.80	28.20	-14.69	-10.20
-4.32	-5.35	-22.80	-28.20	-9.60	10.11
-6.63	0.87	-11.04	22.63	-9.60	-10.11
-6.63	-0.87	-11.04	-22.63	-4.93	8.03
-2.10	4.29	-6.59	23.69	-4.93	-8.03
-2.10	-4.29	-6.59	-23.69	-7.30	1.21
-1.65	4.43	-3.16	12.53	-7.30	-1.21
-1.65	-4.43	-3.16	-12.53	-5.40	1.21

Parameter set 1		**Parameter set 2**		**Parameter set 3**	
Re(λ_i)	Im(λ_i)	Re(λ_i)	Im(λ_i)	Re(λ_i)	Im(λ_i)
-0.78	2.24	-19.80	4.61	-5.40	-1.21
-0.78	-2.24	-19.80	-4.61	-5.00	1.93
-4.82	1.33	-17.87	4.60	-5.00	-1.93
-4.82	-1.33	-17.87	-4.60	-1.55	3.26
-4.69	0.87	-16.92	4.61	-1.55	-3.26
-4.69	-0.87	-16.92	-4.61	-1.65	4.43
-0.01	0.00	-16.53	4.61	-1.65	-4.43
-0.03	0.00	-16.53	-4.61	-4.35	1.19
-0.04	0.00	-16.38	4.61	-4.35	-1.19
-0.14	0.00	-16.38	-4.61	-3.10	1.94
-0.31	0.00	-16.27	4.61	-3.10	-1.94
-0.69	0.00	-16.27	-4.61	-4.01	1.20
-1.28	1.35	-16.30	4.61	-4.01	-1.20
-1.28	-1.35	-16.30	-4.61	-3.59	0.00
-1.29	1.35	-16.28	4.61	-3.80	1.19
-1.29	-1.35	-16.28	-4.61	-3.80	-1.19
-1.31	1.35	-10.27	7.10	-3.70	1.19
-1.31	-1.35	-10.27	-7.10	-3.70	-1.19
-1.37	1.35	-8.33	7.08	-3.68	1.19
-1.37	-1.35	-8.33	-7.08	-3.68	-1.19
-1.49	1.34	-7.39	7.10	-3.67	1.19
-1.49	-1.34	-7.39	-7.10	-3.67	-1.19
-1.92	1.34	-6.99	7.08	-2.08	1.93
-1.92	-1.34	-6.99	-7.08	-2.08	-1.93
-1.64	0.51	-6.85	7.10	-1.72	1.96
-1.64	-0.51	-6.85	-7.10	-1.72	-1.96
-3.74	0.87	-6.77	7.11	-1.41	1.92
-3.74	-0.87	-6.77	-7.11	-1.41	-1.92
-2.85	1.29	-6.74	7.11	-1.43	1.92

Parameter set 1		**Parameter set 2**		**Parameter set 3**	
Re(λ_i)	Im(λ_i)	Re(λ_i)	Im(λ_i)	Re(λ_i)	Im(λ_i)
-2.85	-1.29	-6.74	-7.11	-1.43	-1.92
-3.47	0.00	-6.76	7.11	-1.44	1.92
-3.34	0.87	-6.76	-7.11	-1.44	-1.92
-3.34	-0.87	-3.48	0.00	-1.54	1.93
-3.20	0.87	-1.49	0.43	-1.54	-1.93
-3.20	-0.87	-1.49	-0.43	-1.67	0.00
-3.12	0.87	-0.69	0.00	-0.67	0.00
-3.12	-0.87	-0.32	0.00	-0.30	0.00
-3.09	0.87	-0.14	0.00	-0.13	0.00
-3.09	-0.87	-0.04	0.00	-0.04	0.00
-3.11	0.87	-0.03	0.00	-0.03	0.00
-3.11	-0.87	-0.01	0.00	-0.01	0.00
-0.47	0.00	-0.48	0.00	-0.47	0.00

E MSBR SYSTEM

E.1 Nonlinear System of Delayed Differential Equations

The MSBR model is represented by the following set of nonlinear delayed differential equations, which were specified in the reference paper by the Politecnico di Milano [7]:

$$\frac{\mathrm{d}P(t)}{\mathrm{d}t} = \frac{\rho_0 + \rho_\mathrm{t}(t) + \rho_\mathrm{ex}(t) - \beta}{\Lambda} P(t) + \sum_{j=1}^{6} \lambda_j \widetilde{C}_j(t) \tag{E-1}$$

$$\text{with } \rho_\mathrm{t}(t) = \alpha_\mathrm{f}\Big(T^*_\mathrm{c}(t) - T^*_{\mathrm{c}0}\Big) + \alpha_\mathrm{g}\Big(T^*_\mathrm{g}(t) - T^*_{\mathrm{g}0}\Big)$$

$$\text{and } T^*_c(t) = \frac{1}{N_\mathrm{c}} \sum_{i=1}^{N_\mathrm{c}} T_{c,i}(t)$$

$$\text{and } T^*_g(t) = \frac{1}{N_\mathrm{c}} \sum_{i=1}^{N_\mathrm{c}} T_{g,i}(t)$$

$$\frac{\mathrm{d}\widetilde{C}_j(t)}{\mathrm{d}t} = \frac{\beta_j}{\Lambda} P(t) - (\lambda_j + \lambda_\mathrm{c})\widetilde{C}_j(t) + \lambda_\mathrm{c}\widetilde{C}_j(t - \tau_\mathrm{e})\mathrm{e}^{-\tau_\mathrm{e}\lambda_j} \tag{E-2}$$

$$\text{for } j = 1 \ldots 6$$

$$\frac{\mathrm{d}T_{\mathrm{c},1}(t)}{\mathrm{d}t} = \frac{f_1\gamma_\mathrm{f}}{M_{\mathrm{c},1}\,c} P(t) + \frac{W}{M_{\mathrm{c},1}}\Big(T_{\mathrm{he},N_\mathrm{he}}(t - \tau_2) - T_{\mathrm{c},1}(t)\Big) + \frac{U_1}{M_{\mathrm{c},1}\,c}\Big(T_{\mathrm{g},1}(t) - T_{\mathrm{c},1}(t)\Big) \tag{E-3}$$

$$\frac{\mathrm{d}T_{\mathrm{c},i}(t)}{\mathrm{d}t} = \frac{f_i\gamma_\mathrm{f}}{M_{\mathrm{c},i}\,c} P(t) + \frac{W}{M_{\mathrm{c},i}}\Big(T_{\mathrm{c},i-1}(t) - T_{\mathrm{c},i}(t)\Big) + \frac{U_i}{M_{\mathrm{c},i}\,c}\Big(T_{\mathrm{g},i}(t) - T_{\mathrm{c},i}(t)\Big) \tag{E-4}$$

$$\text{for } i = 2, \ldots, N_\mathrm{c}$$

$$\frac{\mathrm{d}T_{\mathrm{g},i}(t)}{\mathrm{d}t} = \frac{f_i\gamma_\mathrm{g}}{M_{\mathrm{g},i}\,c_\mathrm{g}} P(t) + \frac{U_i}{M_{\mathrm{g},i}\,c_\mathrm{g}}\Big(T_{\mathrm{c},i}(t) - T_{\mathrm{g},i}(t)\Big) \tag{E-5}$$

$$\text{for } i = 1, \ldots, N_\mathrm{c}$$

$$\frac{\mathrm{d}T_{\mathrm{he},1}(t)}{\mathrm{d}t} = \frac{W}{M_{\mathrm{he},1}}\Big(T_{\mathrm{c},N_\mathrm{c}}(t - \tau_1) - T_{\mathrm{he},1}(t)\Big) + \frac{K_1}{M_{\mathrm{he},1}\,c}\Big(T_\mathrm{ic} - T_{\mathrm{he},1}(t)\Big) \tag{E-6}$$

$$\frac{\mathrm{d}T_{\mathrm{he},i}(t)}{\mathrm{d}t} = \frac{W}{M_{\mathrm{he},i}}\Big(T_{\mathrm{he},i-1}(t) - T_{\mathrm{he},i}(t)\Big) + \frac{K_i}{M_{\mathrm{he},i}\,c}\Big(T_\mathrm{ic} - T_{\mathrm{he},i}(t)\Big) \tag{E-7}$$

$$\text{for } i = 2, \ldots, N_\mathrm{he}.$$

Most equations are adopted from the MSFR system, a detailed description of which can be

found in Section 4.2. However, a significant difference is the introduction of the graphite temperature $T_{\mathrm{g},i}(t)$ for each region i of the core. This also leads to additional reactivity feedback resulting from the graphite.

The parameters used in Eqs. E-1 to E-7 are listed in Table E-1 together with their values as given by the reference paper. Just as for the MSFR parameter list, it was found that there are discrepancies between the values provided by the reference article and those of the quoted parameter sources [39] and [42]. As a consequence, the mismatching parameters were adapted according to the quoted articles. The updated parameters are marked in red in Table E-1.

Table E-1: Parametric and discretisation data for the MSBR model according to [7], changes in red according to [39] and [42]

Parameters and discretisation data	**Symbol**	**Unit**	**Value**
Nominal thermal power	P_{nom}	$\mathrm{MW_{th}}$	2250
Reactivity contribution for ensuring steady-state conditions	ρ_0	$-$	$1.25 \cdot 10^{-3}$
Mean neutron generation time	Λ	ms	0.36
Total fraction of delayed neutron precursors	β	$-$	$303.6 \cdot 10^{-5}$
Fraction of delayed neutron precursors of group 1	β_1	$-$	$23.9 \cdot 10^{-5}$
Fraction of delayed neutron precursors of group 2	β_2	$-$	$59.1 \cdot 10^{-5}$
Fraction of delayed neutron precursors of group 3	β_3	$-$	$62.6 \cdot 10^{-5}$
Fraction of delayed neutron precursors of group 4	β_4	$-$	$115.5 \cdot 10^{-5}$
Fraction of delayed neutron precursors of group 5	β_5	$-$	$31.6 \cdot 10^{-5}$
Fraction of delayed neutron precursors of group 6	β_6	$-$	$10.9 \cdot 10^{-5}$
Decay constant of delayed neutron precursors of group 1	λ_1	$\mathrm{s^{-1}}$	$1.272 \cdot 10^{-2}$
Decay constant of delayed neutron precursors of group 2	λ_2	$\mathrm{s^{-1}}$	$3.174 \cdot 10^{-2}$
Decay constant of delayed neutron precursors of group 3	λ_3	$\mathrm{s^{-1}}$	$1.16 \cdot 10^{-1}$
Decay constant of delayed neutron precursors of group 4	λ_4	$\mathrm{s^{-1}}$	$3.11 \cdot 10^{-1}$

Parameter	Symbol	Unit	Value
Decay constant of delayed neutron precursors of group 5	λ_5	s^{-1}	1.4
Decay constant of delayed neutron precursors of group 6	λ_6	s^{-1}	3.87
Core transit time	τ_c	s	4.51
External loop transit time	τ_e	s	6.05
Inverse of core transit time	λ_c	s^{-1}	0.2217
Inverse of external loop transit time	λ_e	s^{-1}	0.1653
Hot leg transit time	τ_1	s	2.125
Cold leg transit time	τ_2	s	2.125
Salt temperature feedback coefficient	α_f	K^{-1}	$-3.233 \cdot 10^{-5}$
Graphite temperature feedback coefficient	α_g	K^{-1}	$-0.605 \cdot 10^{-5}$
Reference average temperature of the salt	$T^*_{\mathrm{c}0}$	K	923
Reference average temperature of the graphite	$T^*_{\mathrm{g}0}$	K	930.32
Average temperature of the intermediate salt	T_ic	K	797.49
Mass of salt in the core	M_c	kg	$54\,205$
Mass of graphite in the core	M_g	kg	$122\,623$
Mass of salt in the heat exchangers	M_he	kg	$21\,634$
Mass of salt in the cold leg	M_cl	kg	$25\,540$
Mass of salt in the hot leg	M_hl	kg	$25\,540$
Specific heat capacity of the primary salt	c	$\mathrm{J\ kg^{-1}\ K^{-1}}$	1356
Specific heat capacity of the graphite	c_g	$\mathrm{J\ kg^{-1}\ K^{-1}}$	1758
Salt flow rate in the primary circuit	W	$\mathrm{kg\ s^{-1}}$	$12\,019$
Overall heat transfer coefficient between the primary and intermediate salt in the heat exchanger	K	$\mathrm{W\ K^{-1}}$	$2.32 \cdot 10^7$
Overall heat transfer coefficient between the primary salt and the graphite in the core	U	$\mathrm{W\ K^{-1}}$	$2.49 \cdot 10^7$
Fraction of fission power released in the fuel salt	γ_f	$-$	0.919
Fraction of fission power released in the graphite	γ_g	$-$	0.081

The given value of the reactivity contribution ρ_0, which ensures steady-state conditions by compensating the circulation of the delayed neutron precursors, is calculated according to Eq. 4-2. The values of the reference average graphite temperature $T^*_{\mathrm{g}0}$ and the intermediate salt T_{ic} are determined by solving the presented system of equations for steady-state conditions.

The temperatures in the core ($T_{\mathrm{c},i}$ and $T_{\mathrm{g},i}$) and heat exchanger ($T_{\mathrm{he},i}$) are discretised by different regions i in each component. The number of core and heat exchanger regions is set to ten in each case. The weighting factors f_i are the same as for the MSFR and can be calculated according to a cosine distribution (see Eq. 4-11).

E.2 Comparison with Reference Plots

In the reference article [7], a linearised version of the MSBR system is used to create some Bode plots. In order to verify the implementation of the equation system and the parameter list specified in this work, Eqs. E-1 to E-7 are linearised, and the resulting Bode plots are compared to those of the reference paper. The linearisation of the relevant equations around the fixed point

$$\boldsymbol{X}_0 = \begin{pmatrix} P_0 & \widetilde{C}_{1,0} & \dots & \widetilde{C}_{8,0} & T_{\mathrm{c},1,0} & \dots & T_{\mathrm{c},N_{\mathrm{c}},0} & T_{\mathrm{g},1,0} & \dots & T_{\mathrm{g},N_{\mathrm{c}},0} & T_{\mathrm{he},1,0} & \dots & T_{\mathrm{he},N_{\mathrm{he}},0} \end{pmatrix}^\top$$

is carried out according to Eqs. 3-8 and 3-9.

Figure E-1 shows the closed-loop Bode plots obtained in MATLAB for the linearised MSBR system. The graphs of the reference paper are depicted in the background. The different-coloured graphs represent the Bode plots for different power levels P_0. The associated MATLAB file is saved on the accompanying CD as 'ClosedLoop_SS_MSBR.mlx'.

The magnitude plot shows almost no deviation from the reference graph. In the phase plot, there is a difference between the newly calculated plot curves and the ones obtained from the reference paper, which seems to be increasing with the power level P_0. This difference might be due to another mismatching parameter. However, this assumption cannot be verified since the literature sources provided in the reference article do not specify all of the listed parameter values. Hence, no further parameter adjustments are

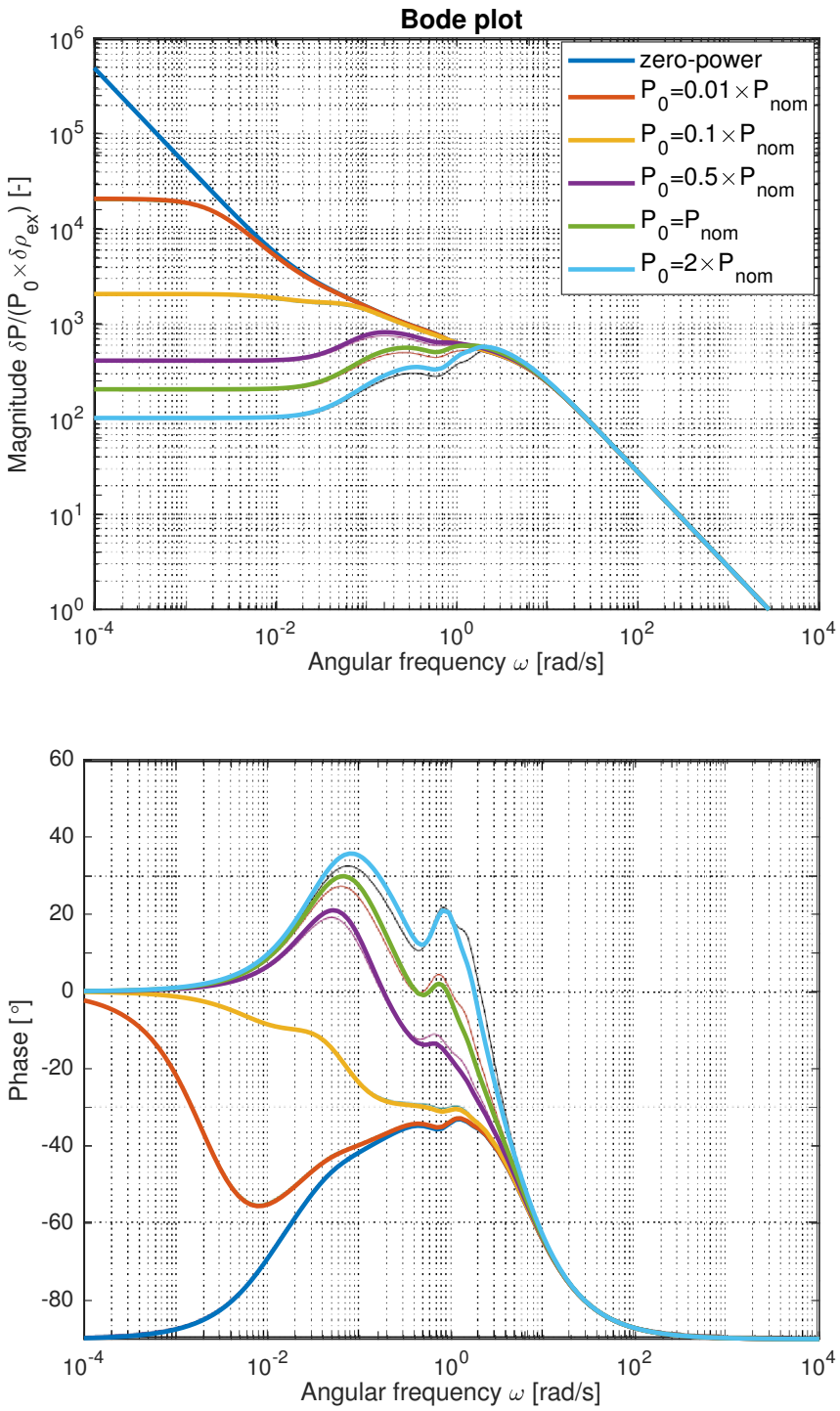

Figure E-1: Closed-loop Bode plots of the linearised MSBR system for different power levels in comparison with the results obtained in [7].

made.

E.3 Nonlinear System of Ordinary Differential Equations

Since the numerical bifurcation tool MatCont requires the input equations to be ODEs, the nonlinear DDE system (Eqs. E-1 to E-7) has to be rewritten as an ODE system. Therefore, the variables containing time delays $\widetilde{C}_j(t-\tau_\mathrm{e})$, $T_{\mathrm{c},N_\mathrm{c}}(t-\tau_1)$ and $T_{\mathrm{he},N_\mathrm{he}}(t-\tau_2)$ are replaced by new variables that are defined by additional ODEs. These variables constitute:

- the delayed neutron precursor population of group j in the region i of the external loop $Y_{i,j}(t)$,
- the salt temperature in the region i of the hot leg of the external loop $T_{\mathrm{hl},i}(t)$,
- the salt temperature in the region i of the cold leg of the external loop $T_{\mathrm{cl},i}(t)$.

A detailed explanation of these additional variables and their differential equations can be found in Sections 4.4.2 and 4.4.3.

Using the presented auxiliary variables, the nonlinear DDE system can be rewritten as the following nonlinear ODE system:

$$\frac{\mathrm{d}P(t)}{\mathrm{d}t} = \frac{\rho_0 + \rho_\mathrm{t}(t) + \rho_\mathrm{ex}(t) - \beta}{\Lambda} P(t) + \sum_{j=1}^{6} \lambda_j \widetilde{C}_j(t) \tag{E-8}$$

$$\text{with } \rho_\mathrm{t}(t) = \alpha_\mathrm{ex}\Big(T_\mathrm{c}^*(t) - T_\mathrm{c0}^*\Big) + K_\mathrm{D} \ln\left(\frac{T_\mathrm{c}^*(t)}{T_\mathrm{c0}^*}\right)$$

$$\text{and } T_c^*(t) = \frac{1}{N_\mathrm{c}} \sum_{i=1}^{N_\mathrm{c}} T_{c,i}(t)$$

$$\text{and } T_g^*(t) = \frac{1}{N_\mathrm{c}} \sum_{i=1}^{N_\mathrm{c}} T_{g,i}(t)$$

$$\frac{\mathrm{d}\widetilde{C}_j(t)}{\mathrm{d}t} = \frac{\beta_j}{\Lambda} P(t) - (\lambda_j + \lambda_\mathrm{c})\widetilde{C}_j(t) + \lambda_\mathrm{c} Y_{N_\mathrm{e},j}(t) \tag{E-9}$$

$$\text{for } j = 1 \ldots 6$$

$$\frac{\mathrm{d}T_{\mathrm{c},1}(t)}{\mathrm{d}t} = \frac{f_1 \gamma_\mathrm{f}}{M_{\mathrm{c},1}\, c} P(t) + \frac{W}{M_{\mathrm{c},1}}\Big(T_{\mathrm{cl},N_\mathrm{cl}}(t) - T_{\mathrm{c},1}(t)\Big) + \frac{U_1}{M_{\mathrm{c},1}\, c}\Big(T_{\mathrm{g},1}(t) - T_{\mathrm{c},1}(t)\Big) \tag{E-10}$$

$$\frac{\mathrm{d}T_{\mathrm{c},i}(t)}{\mathrm{d}t} = \frac{f_i \gamma_\mathrm{f}}{M_{\mathrm{c},i}\, c} P(t) + \frac{W}{M_{\mathrm{c},i}} \Big(T_{\mathrm{c},i-1}(t) - T_{\mathrm{c},i}(t) \Big) + \frac{U_i}{M_{\mathrm{c},i}\, c} \Big(T_{\mathrm{g},i}(t) - T_{\mathrm{c},i}(t) \Big) \tag{E-11}$$

for $i = 2, \ldots, N_\mathrm{c}$

$$\frac{\mathrm{d}T_{\mathrm{g},i}(t)}{\mathrm{d}t} = \frac{f_i \gamma_\mathrm{g}}{M_{\mathrm{g},i}\, c_\mathrm{g}} P(t) + \frac{U_i}{M_{\mathrm{g},i}\, c_\mathrm{g}} \Big(T_{\mathrm{c},i}(t) - T_{\mathrm{g},i}(t) \Big) \tag{E-12}$$

for $i = 1, \ldots, N_\mathrm{c}$

$$\frac{\mathrm{d}T_{\mathrm{he},1}(t)}{\mathrm{d}t} = \frac{W}{M_{\mathrm{he},1}} \Big(T_{\mathrm{hl},N_\mathrm{hl}}(t) - T_{\mathrm{he},1}(t) \Big) + \frac{K_1}{M_{\mathrm{he},1}\, c} \Big(T_\mathrm{ic} - T_{\mathrm{he},1}(t) \Big) \tag{E-13}$$

$$\frac{\mathrm{d}T_{\mathrm{he},i}(t)}{\mathrm{d}t} = \frac{W}{M_{\mathrm{he},i}} \Big(T_{\mathrm{he},i-1}(t) - T_{\mathrm{he},i}(t) \Big) + \frac{K_i}{M_{\mathrm{he},i}\, c} \Big(T_\mathrm{ic} - T_{\mathrm{he},i}(t) \Big) \tag{E-14}$$

for $i = 2, \ldots, N_\mathrm{he}$.

$$\frac{\mathrm{d}Y_{1,j}(t)}{\mathrm{d}t} = \lambda_\mathrm{e} N_\mathrm{e} \widetilde{C}_j(t) - \lambda_j Y_{1,j}(t) - \lambda_\mathrm{e} N_\mathrm{e} Y_{1,j}(t)$$

for $j = 1 \ldots 6$

$$\frac{\mathrm{d}Y_{i,j}(t)}{\mathrm{d}t} = \lambda_\mathrm{e} N_\mathrm{e} Y_{i-1,j}(t) - \lambda_j Y_{i,j}(t) - \lambda_\mathrm{e} N_\mathrm{e} Y_{i,j}(t) \tag{E-15}$$

for $i = 2 \ldots N_\mathrm{e}$ and $j = 1 \ldots 6$

$$\frac{\mathrm{d}T_{\mathrm{cl},1}(t)}{\mathrm{d}t} = \frac{W}{M_{\mathrm{cl},1}} \Big(T_{\mathrm{he},N_\mathrm{he}}(t) - T_{\mathrm{cl},1}(t) \Big) \tag{E-16}$$

$$\frac{\mathrm{d}T_{\mathrm{cl},i}(t)}{\mathrm{d}t} = \frac{W}{M_{\mathrm{cl},i}} \Big(T_{\mathrm{cl},i-1}(t) - T_{\mathrm{cl},i}(t) \Big) \tag{E-17}$$

for $i = 2 \ldots N_\mathrm{cl}$

$$\frac{\mathrm{d}T_{\mathrm{hl},1}(t)}{\mathrm{d}t} = \frac{W}{M_{\mathrm{hl},1}} \Big(T_{\mathrm{c},N_\mathrm{c}}(t) - T_{\mathrm{hl},1}(t) \Big) \tag{E-18}$$

$$\frac{\mathrm{d}T_{\mathrm{hl},i}(t)}{\mathrm{d}t} = \frac{W}{M_{\mathrm{hl},i}} \Big(T_{\mathrm{hl},i-1}(t) - T_{\mathrm{hl},i}(t) \Big) \tag{E-19}$$

for $i = 2 \ldots N_\mathrm{hl}$

Regarding the discretisation of the external loop, $N_\mathrm{e} = 4$ is chosen for the delayed neutron precursors and $N_\mathrm{cl} = N_\mathrm{hl} = 4$ for the temperature in the cold and hot leg. Thus, the ODE system contains 69 equations for 69 state variables.

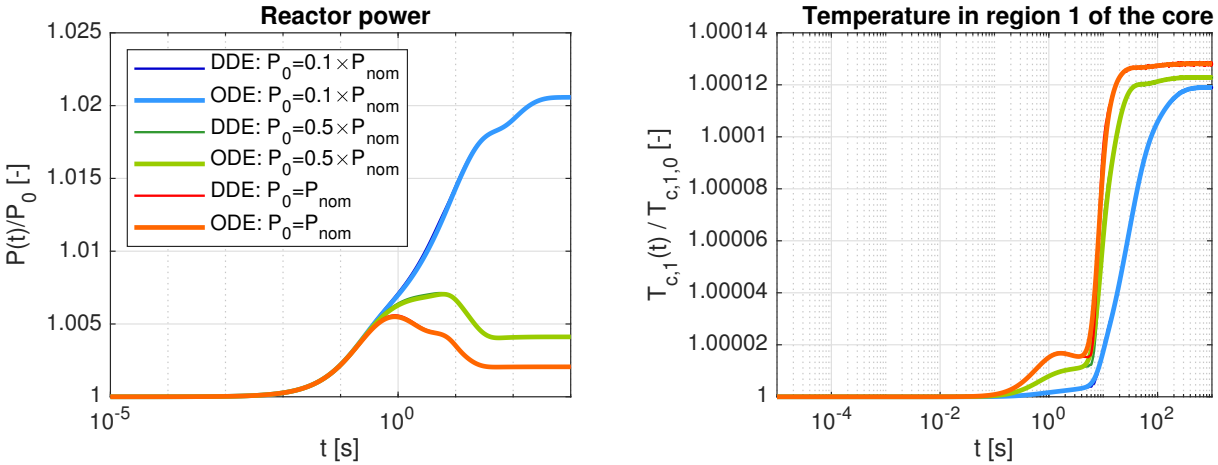

Figure E-2: MSBR time series plots of $P(t)$ and $T_{\mathrm{c},1}(t)$ for the nonlinear ODE system, compared to those of the nonlinear DDE system.

Time series plots of the reactor power and salt temperature are created in MATLAB for the ODE system and the original DDE system for a reactivity insertion of $\rho_{\mathrm{ex}}(t_0 = 0) = 1 \cdot 10^{-3}$. Both graphs are compared with each other to ensure that the rewritten ODEs describe the same behaviour as the original model. Figure E-2 shows these plots for different initial power levels. The reference plot of the DDE system uses a discretisation with $N_{\mathrm{c}} = N_{\mathrm{he}} = 10$. The corresponding MATLAB file can be found on the CD under the name 'ODE_DDE_System_MSBR.mlx'.

The curves for the DDE and ODE systems follow almost identical paths in the reactor power plot as well as the core temperature plot. Hence, one can conclude that the specified ODE system with the given discretisation data approximates the dynamical evolution of the DDE system very precisely.

F LIST OF MATLAB AND MATCONT FILES

Tables F-1 and F-2 list all MATLAB and MatCont files that are used in this work. The files are saved on the accompanying CD.

Table F-1: List of the main MATLAB and MatCont files saved on the accompanying CD

File name	Reactor design	Description
DDE_System_lin.mlx	MSFR	Time series plot of the linearised DDE system (Eqs. 4-14 to 4-19)
ClosedLoop_SS.mlx	MSFR	Closed-loop Bode plots of the linearised DDE system (Eqs. 4-14 to 4-19) using a state space model
ClosedLoop_SOE.mlx	MSFR	Closed-loop Bode plots of the linearised DDE system (Eqs. 4-14 to 4-19) using the Laplace transform
ClosedLoop_Simulink.mlx	MSFR	Closed-loop Bode plots of the linearised DDE system (Eqs. 4-14 to 4-19) using a Simulink model
DDE_System.mlx	MSFR	Time series plot of the nonlinear DDE system (Eqs. 4-21 to 4-26)
ODE_DDE_System.mlx	MSFR	Time series plot of the nonlinear ODE system (Eqs. 4-45 to 4-55) compared to the nonlinear DDE system (Eqs. 4-21 to 4-26)
MSFR_5.m	MSFR	MatCont file for the MSFR system (Eqs. 4-45 to 4-55)
Jacobian_Set	MSFR	Eigenvalues of Jacobian matrix
ClosedLoop_SS_MSBR.mlx	MSBR	Closed-Loop Bode plot of linearised DDE system
ODE_DDE_System_MSBR.mlx	MSBR	Time series plot of the nonlinear ODE system (Eqs. E-1 to E-7) compared to the nonlinear DDE system (Eqs. E-8 to E-19)
MSBR.m	MSBR	MatCont file for the MSBR system (Eqs. E-1 to E-7)

Table F-2: List of the auxiliary MATLAB and MatCont files saved on the accompanying CD

File name	Reactor design	Description
Initialization.mlx	MSFR	Parameter values of Table 4-1
Initialization2.mlx	MSFR	Updated parameter values of Table 4-3
Initialization3.mlx	MSFR	Updated parameter values of Table 4-3 accepting additional inputs
ddefun_system_lin.mlx	MSFR	Linearised DDE system (Eqs. 4-14 to 4-19)
ddefun_system.mlx	MSFR	Full DDE system (Eqs. 4-21 to 4-26)
odefun_system.mlx	MSFR	ODE system (Eqs. 4-45 to 4-55)
Simulink_Closed_Loop3.slx	MSFR	Simulink model used for 'Closed-Loop_Simulink.mlx'
msfr_fun_system.mlx	MSFR	ODE system (Eqs. C-15 to C-15) used by MatCont
Initialization_MSBR.mlx	MSBR	Parameter values of Table E-1
ddefun_system_MSBR.mlx	MSBR	Full DDE system (Eqs. E-8 to E-19)
odefun_system.mlx	MSBR	ODE system (Eqs. E-1 to E-7)
msbr_fun_system_MSBR.mlx	MSBR	ODE system (Eqs. E-1 to E-7)) used by MatCont